

INFORMATION TO USERS

This manuscript has been reproduced from the microfilm master. UMI films the text directly from the original or copy submitted. Thus, some thesis and dissertation copies are in typewriter face, while others may be from any type of computer printer.

The quality of this reproduction is dependent upon the quality of the copy submitted. Broken or indistinct print, colored or poor quality illustrations and photographs, print bleedthrough, substandard margins, and improper alignment can adversely affect reproduction.

In the unlikely event that the author did not send UMI a complete manuscript and there are missing pages, these will be noted. Also, if unauthorized copyright material had to be removed, a note will indicate the deletion.

Oversize materials (e.g., maps, drawings, charts) are reproduced by sectioning the original, beginning at the upper left-hand corner and continuing from left to right in equal sections with small overlaps. Each original is also photographed in one exposure and is included in reduced form at the back of the book.

Photographs included in the original manuscript have been reproduced xerographically in this copy. Higher quality 6" x 9" black and white photographic prints are available for any photographs or illustrations appearing in this copy for an additional charge. Contact UMI directly to order.

UMI

A Bell & Howell Information Company
300 North Zeeb Road, Ann Arbor MI 48106-1346 USA
313/761-4700 800/521-0600

UNIVERSITY OF OKLAHOMA

GRADUATE COLLEGE

**Search for Charged Higgs Bosons
in Top Quark Pair Decays
at DØ**

A Dissertation

SUBMITTED TO THE GRADUATE FACULTY

In partial fulfillment of the requirements
for the degree of

Doctor of Philosophy

by

ERIC H. SMITH

Norman, Oklahoma
1999

UMI Number: 9930842

UMI Microform 9930842
Copyright 1999, by UMI Company. All rights reserved.

This microform edition is protected against unauthorized
copying under Title 17, United States Code.

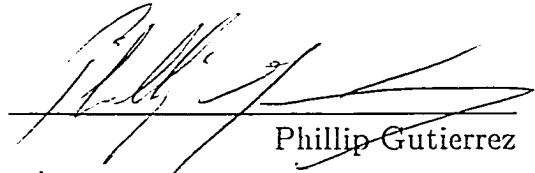
UMI
300 North Zeeb Road
Ann Arbor, MI 48103

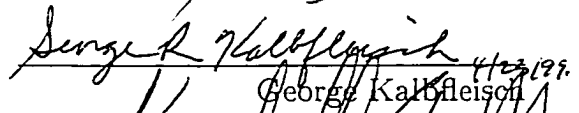
© Eric H. Smith 1999
ALL RIGHTS RESERVED

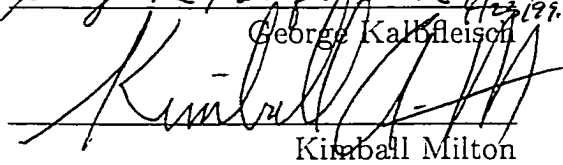
Search for Charged Higgs Bosons
in Top Quark Pair Decays
at DØ

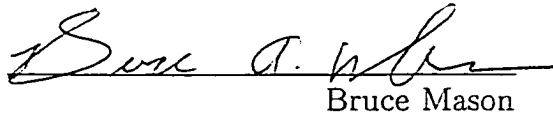
A Dissertation APPROVED FOR THE
DEPARTMENT OF PHYSICS AND ASTRONOMY

BY


Phillip Gutierrez


George Kalbfleisch


Kimball Milton


Bruce Mason


James Hawthorne

Acknowledgments

My experience in the OU high energy physics group has been extremely fulfilling, allowing me to work in an environment of constant change and challenge. Many people deserve thanks for allowing me this time of education and adventure.

I would first like to thank my wife, Cristina. After graduating from a long, arduous stint in dental school, she packed up her life, and moved with me to Chicago. While in a residency program in a Chicago hospital, she has supported my efforts to complete a difficult thesis; work which often left little time for her. Her support has made the completion of five years of hard work possible.

I would also like to thank my advisor, Prof. Phillip Gutierrez. Unlike the aloof and unconcerned advisors from other universities that I've heard so much about, Phil has always maintained interest my work, both thesis and service, and his input and criticism have many times steered me back onto a productive course. The final quality of my dissertation is the result of his work.

The person with whom I've been in closest contact with over the course of my physics analysis is Dr. Dhiman Chakraborty. It was Dhiman's indirect search for charged Higgs which provided the groundwork for my direct search. His dedication to the truth in data analysis has forced me (and inspired me) to understand, in every detail, the subtleties of this search; the result was an analysis which surpassed our expectations, and could be defended with confidence.

While not involved directly in my analysis, Prof. George Kalbfleisch must be acknowledged as a major influence in my physics education. He has an envious ability to draw solid conclusions given, what seems to the inexperienced, loosely related pieces of information. His continuing drive to discover and learn is a characteristic that everyone wants, but few posses; I hope to be one of the few.

I cannot forget the influence of Prof. Dave Kaplan, who has not been with the high energy group at OU for many years. It was in his course on Waves and Optics that my interest in particle physics was cemented. Dave, seeing my enthusiasm,

was able to open the door to the group's work. That marked the beginning of eight years of education and work, and it has been the most interesting eight years thus far.

Contents

1	The Physics of Higgs Bosons	1
1.1	Introduction	1
1.2	E&M	2
1.3	SSB and the Goldstone theorem	4
1.4	The Higgs mechanism	6
1.4.1	Higgs in $U(1)$	6
1.4.2	$SU(2) \otimes U(1)$	8
1.5	Beyond the SM Higgs	11
1.5.1	Experimental signatures	14
2	The Experiment	16
2.1	Accelerator complex	16
2.2	The DØ Detector	20
2.2.1	Drift Chamber Principles	22
2.2.2	Vertex Drift Chamber	23
2.2.3	Transition Radiation Detector	24
2.2.4	Central Drift Chamber	25
2.2.5	Forward Drift Chambers	26
2.3	Calorimeter	27
2.3.1	Principles of Calorimetry	27
2.3.2	Calorimeter Geometry	30
2.4	Muon System	33

2.4.1	WAMUS	34
2.4.2	SAMUS	35
3	Triggering and Data Acquisition	36
3.1	Level 0	38
3.2	Level 1 framework	38
3.2.1	Level 1 Calorimeter Trigger	39
3.2.2	Level 1 Muon triggers	40
3.3	Level 2	40
4	Defining objects offline	42
4.1	Jets from gluons and quarks	42
4.1.1	Offset correction	44
4.1.2	Response: The Missing E_T Projection Fraction Method . . .	45
4.1.3	Showering Correction	47
4.2	Identifying the origin of jets	48
4.2.1	Jets from Tau decay	48
5	Data Selection	51
6	Analysis	54
6.1	Event Selection	56
6.1.1	Cutoffs on output from the Neural Network	58
6.2	Final selection: τ -id	64
6.2.1	τ -id efficiency	68
6.2.2	Correction for Data-Based Monte Carlo	68
6.3	Backgrounds	72
6.3.1	Calculation of QCD fake rate	74
6.3.2	Effect of \cancel{E}_T on the QCD fake rate	77
7	Selected Data Sample	79
7.1	Efficiencies	79

8	Trigger Efficiency	81
9	Results	86
9.0.1	Accessible region of parameter space	98
9.0.2	Estimation of low $\tan\beta$	99
9.1	Bayesian Results	106
9.1.1	Choosing the NN cut	115
9.2	Frequentist Results	115
9.3	Conclusions	118
9.3.1	Limits from other experiments	121
A	Principles of Feed-forward Neural Networks	123
A.1	Fundamentals	123
A.2	Back-Propagation	126

List of Figures

1.1	Branching ratios for the three possible final states of H^+ decay. . .	13
1.2	Branching ratios of top to charged Higgs, for various M_{H^+}	14
2.1	Layout of the Fermilab accelerator complex (not to scale).	17
2.2	Cutaway view of the DØ detector.	21
2.3	End view of the vertex chamber.	23
2.4	Cutaway view of the calorimeter.	31
2.5	Section of cathode pads found in muon chamber drift tubes.	34
3.1	Schematic of the DØ trigger and data acquisition system.	37
4.1	Sample event display, showing a $t\bar{t} \rightarrow W^+W^-b\bar{b} \rightarrow alljets$ candidate, in the η, ϕ coordinate system.	49
6.1	Missing energy in the $t\bar{t} \rightarrow WWbb$ Monte Carlo. The \cancel{E}_T has been scaled by 1/150, so that a value of 0.2 corresponds to $\cancel{E}_T = 30GeV$	57
6.2	Event \cancel{E}_T	59
6.3	First eigenvalue of the momentum tensor	59
6.4	Second eigenvalue of the momentum tensor	60
6.5	Scheme for the training of neural nets, and the determination of all signal efficiencies.	61
6.6	Separation in the output of a neural network trained on $t\bar{t} \rightarrow H^-H^+$ where both Higgs decay to τ . One test signal is data, and the other is MC of $t\bar{t} \rightarrow HH$. Ordinate is number of events, normalized to one.	63

6.7	Energy for τ decays in SM decays of top quark pairs, and fakes found in JET_MULTI, where the energy is for 0.5 cone jets matched to τ jets, and the matched jets have $ \eta < 0.9$	67
6.8	τ -id efficiency for all events in the decay of $t\bar{t} \rightarrow W^+W^-b\bar{b}$; $W^+ \rightarrow 2jets$; $W^- \rightarrow \tau$ where only hadronic τ decays are considered. . . .	69
6.9	Correlation of Profile and Discriminant for a sample of $t\bar{t} \rightarrow WW \rightarrow \tau j j$ events.	70
6.10	Fake rates for a combined sample of JET_MULTI, and JET_MS_MULTI.	76
6.11	Predicted number of qcd fakes as a function of missing energy. . .	77
8.1	Trigger Efficiencies for standard model top decay, and top anti-top decay to W and Higgs, using the JET_MULTI trigger.	82
8.2	Trigger Efficiencies for top anti-top decay to Higgs Higgs, using the JET_MS_MULTI trigger.	83
8.3	Trigger efficiency for standard model decay, and the distribution of E_{T_5} for the same mode.	84
8.4	Distribution of E_{T_5} for $t\bar{t} \rightarrow WH$, overlaid on the trigger efficiency for standard model decay.	85
8.5	Distribution of E_{T_4} for $t\bar{t} \rightarrow HH$, overlaid on the trigger efficiency for the HH mode, with $M_H = 50GeV$	85
9.1	Expected and measured events as a function of neural network cut, for the network trained on $t\bar{t} \rightarrow WH$, for $M_H = 50GeV$	88
9.2	Expected and measured events as a function of neural network cut, for the network trained on $t\bar{t} \rightarrow WH$, for $M_H = 80GeV$	89
9.3	Expected and measured events as a function of neural network cut, for the network trained on $t\bar{t} \rightarrow WH$, for $M_H = 110GeV$	90

9.4	Expected and measured events as a function of neural network cut, for the network trained on $t\bar{t} \rightarrow WH$, for $M_H = 140\text{GeV}$	91
9.5	Expected and measured events as a function of neural network cut, for the network trained on $t\bar{t} \rightarrow HH$, for $M_H = 50\text{GeV}$	92
9.6	Expected and measured events as a function of neural network cut, for the network trained on $t\bar{t} \rightarrow HH$, for $M_H = 80\text{GeV}$	93
9.7	Expected and measured events as a function of neural network cut, for the network trained on $t\bar{t} \rightarrow HH$, for $M_H = 110\text{GeV}$	94
9.8	Expected and measured events as a function of neural network cut, for the network trained on $t\bar{t} \rightarrow HH$, for $M_H = 140\text{GeV}$	95
9.9	Schematic of how $t\bar{t} \rightarrow WHbb$ might be separated by the two sets of cuts and neural network selection.	97
9.10	Branching ratios of various $t\bar{t} \rightarrow WX$ final states.	101
9.11	Branching ratios of various $t\bar{t} \rightarrow HH$ final states.	102
9.12	Number of events from $t\bar{t}$ decay expected in the NN_{HH} network, including the estimated modes for low $\tan\beta$	103
9.13	Probability that we measure the data, given all $t\bar{t}$ decays, including the effect of increasing the low $\tan\beta$ estimates by a factor of two. .	104
9.14	Efficiency of detecting $t\bar{t} \rightarrow WH$ and $t\bar{t} \rightarrow HH$. Each curve is the efficiency for detecting single mass, and the abscissa is the mass on which the network was trained.	107
9.15	Fits to the first six parameters used to fit probabilities from the NN_{HH} network, where the cut on the output was placed at 0.88. .	109
9.16	Fits to the last seven parameters used to fit probabilities from the NN_{HH} network, where the cut on the output was placed at 0.88. .	110
9.17	Probability of measuring the data in the NN_{HH} network.	111
9.18	Probability of measuring the data in the NN_{HH} network.	111
9.19	Probability of measuring the data in the NN_{HH} network.	112

9.20	Probability of measuring the data in the NN_{HH} network.	112
9.21	Probability of measuring the data in the NN_{HH} network.	113
9.22	Likelihood surface of $P(\tan \beta, M_{H^+} n)$	114
9.23	Predictions of the excluded area, using efficiencies from MC.	116
9.24	a) Probability that JET_MS_MULTI containing H^+ would give at most the values measured in data. b) Number of events expected in JET_MS_MULTI given H^+	117
9.25	Region excluded by our search, for a NN cut of 0.88.	118
9.26	Effect on the Bayesian limit of using different cuts on neural net outputs.	119
9.27	Effect on the Bayesian limit of using a fourth order polynomial fit the 13 parameters used to generate $P(n \tan \beta, M_{H^+})$	120
9.28	Limits on $(\tan \beta, M_{H^+})$ from CDF and LEP2. The hatched region labelled “ $\alpha(tbH^+)$ large” indicates $\alpha \geq 1$	121
A.1	Schematic of the basic neuron.	125
A.2	Schematic of a full network.	125

List of Tables

1.1	Decay modes, and their branching ratios, for $t\bar{t} \rightarrow \tau + X$, given a H^+	14
1.2	Final states leading to the $t\bar{t} \rightarrow \tau + jets$ topologies used in this analysis. Final states 2 and 4 include their charge-conjugate reactions.	15
2.1	Vertex Drift Chamber Parameters.	24
2.2	Central Drift Chamber Parameters.	26
2.3	Forward Drift Chamber Parameters.	27
2.4	Parameters of the Central Calorimeter	32
2.5	Parameters of the End Calorimeter	32
2.6	Parameters for the WAMUS and SAMUS.	35
5.1	Requirements for the JET_MULTI trigger, and the JET_MULTI and JET_MS_MULTI filters for Run Ib.	52
6.1	Efficiency of cuts defining a τ for DBMC and Isajet.	71
7.1	Efficiencies of loose cuts applied to signal and data.	80
7.2	Efficiencies of networks for all decay modes.	80
8.1	Average trigger efficiencies for the final data set.	84
9.1	Expected and measured events for each network. Notice the similarity in the expected events for a given network type (NN_{XX}), indicating large correlations.	87

9.2	Fractions of signals found in the NN_{HH} output which were also found in the output of NN_{WH}	96
-----	--	----

Chapter 1

The Physics of Higgs Bosons

1.1 Introduction

The fundamental problem in particle physics is the nature of interactions between particles (and fields). In electricity and magnetism (E&M), one asks about the interaction of charged particles, where certain laws, like charge conservation, are known. Also known is the fact that the phase of a particle's wavefunction cannot be measured, meaning that the product $\psi^*\psi$ is invariant under global phase shifts. This global phase invariance results in the previously known conservation of charge. A remarkable thing happens when this global phase invariance is further extended to a local phase invariance. One generates the form of interactions between the charged particles, via a new gauge field, the photon. So, having never seen light, we could have predicted its existence with the simple requirement of local phase (gauge) invariance.

The Standard Model (SM) consists of a larger symmetry group than the $U(1)$ symmetry of E&M. It is $SU(3) \otimes SU(2) \otimes U(1)$, and all interactions are generated by the requirement of local gauge invariance under rotations in the various spaces.

It is known, however, that some of the gauge fields responsible for the electro-weak interactions (those in $SU(2) \otimes U(1)$) are massive, but the addition of mass terms in our Lagrangian \mathcal{L} breaks the very symmetry used to predict the gauge fields! The solution used by the SM to add these masses, while maintaining the renormalizability of the theory, is the application of spontaneous symmetry breaking (SSB). SSB applied to a gauge theory is known as the Higgs mechanism, and any number of massive scalar particles (Higgs) are produced in the process.

The following sections describe the power of local gauge invariance as a tool in predicting gauge fields, and the role of the Higgs mechanism in allowing massive gauge fields in the electroweak sector of the SM. I then move to a richer, non-SM Higgs sector, which is the object of this analysis.

1.2 E&M

In the event that we were unaware of Maxwell's equations, but did know Schrodinger's equation, it would be possible through the application of gauge invariance, to predict the existence of light. Consider some quantum mechanical (QM) observable:

$$\mathcal{O} = \int \psi^* \mathcal{O} \psi \tag{1.1}$$

which is clearly invariant under the rotation

$$\psi(x) \rightarrow e^{i\theta} \psi(x) \tag{1.2}$$

in the case that the angle of rotation does not depend on time or space. If, however, we demand the freedom to choose different phases at different points in space-time (ie $\theta \rightarrow \theta(x)$), then the derivative terms in our Schrodinger equation will transform like [1]:

$$\partial_\mu \psi(x) \rightarrow \partial_\mu \psi'(x) = e^{i\theta(x)} [\partial_\mu \psi(x) + i(\partial_\mu \theta(x))\psi(x)] \quad (1.3)$$

If one postulates the existence of a field, which appears in conjunction with the derivative in a way which cancels the unwanted term in equation (3), *local* gauge invariance can be preserved. The covariant derivative is the result

$$\mathcal{D}_\mu = \partial_\mu + ieA_\mu \quad (1.4)$$

where the gauge field transforms like

$$A_\mu \rightarrow A_\mu - \frac{1}{e} \partial_\mu \theta(x) \quad (1.5)$$

resulting in

$$\mathcal{D}_\mu \psi(x) \rightarrow \mathcal{D}'_\mu \psi'(x) = e^{i\theta(x)} \mathcal{D}_\mu \psi(x) \quad (1.6)$$

We therefore predict the existence of light, through the requirement that our QM observable not depend on when or where we rotate our fields.

Now consider a field theory with our complex field $\psi(x)$ and our gauge field A_μ . A locally invariant \mathcal{L} can be written:

$$\mathcal{L} = -\frac{1}{4} F_{\mu\nu} F^{\mu\nu} + \bar{\psi}(x) (i\gamma^\mu \mathcal{D}_\mu - m) \psi(x) \quad (1.7)$$

where

$$F_{\mu\nu} = \partial_\mu A_\nu - \partial_\nu A_\mu \quad (1.8)$$

\mathcal{L} describes a massive $\psi(x)$, but note that A_μ *must* remain massless

$$-m^2 |A'(x)|^2 \neq -m^2 |A(x)|^2 \quad (1.9)$$

So that local gauge invariance is enough to predict gauge fields, and imply the form of their interaction with massive fields, provided the gauge fields themselves have no mass.

1.3 SSB and the Goldstone theorem

In the previous section, a \mathcal{L} whose physical particle spectrum reflected the symmetry under consideration was outlined. In the case of SSB, the \mathcal{L} which reveals the physical spectrum no longer shows, in any obvious way, the original symmetry. The model first investigated by Goldstone is[2]

$$\mathcal{L} = \frac{1}{2}[(\partial_\mu \phi_1)(\partial^\mu \phi_1) + (\partial_\mu \phi_2)(\partial^\mu \phi_2)] - V(\phi_1^2 + \phi_2^2) \quad (1.10)$$

$$V(\Phi^2) = \frac{1}{2}\mu^2|\Phi|^2 + \frac{1}{4}|\lambda|(|\Phi|^2)^2 \quad (1.11)$$

$$\Phi \equiv \begin{pmatrix} \phi_1 \\ \phi_2 \end{pmatrix} \quad (1.12)$$

where ϕ_1 and ϕ_2 are real scalar fields. This \mathcal{L} is invariant under $SO(2)$ rotations

$$\Phi \rightarrow \Phi' = R\Phi \quad (1.13)$$

where R is the usual 2-D rotation matrix. One investigates the behavior of the vacuum by considering small fluctuations of the fields, \mathcal{L}_{SO} . If $\mu^2 > 0$, the potential is minimum for

$$\langle \Phi \rangle = \begin{pmatrix} 0 \\ 0 \end{pmatrix} \quad (1.14)$$

In this case,

$$\mathcal{L}_{SO} = \frac{1}{2}[(\partial_\mu \phi_1)(\partial^\mu \phi_1) - \mu^2 \phi_1^2] + \frac{1}{2}[(\partial_\mu \phi_2)(\partial^\mu \phi_2) - \mu^2 \phi_2^2] \quad (1.15)$$

neglecting $\mathcal{O}(\phi^4)$. This is the \mathcal{L} for scalar fields with common mass μ^2 . If one chooses the parameter $\mu^2 < 0$, the minimum in the potential (the vacuum) occurs for

$$\frac{\partial V}{\partial \Phi^2} = \frac{1}{2}\mu^2 + \frac{1}{2}\lambda\Phi^2 = 0 \quad (1.16)$$

$$\langle \Phi \rangle_0^2 = -\frac{\mu^2}{|\lambda|} \equiv v^2 \quad (1.17)$$

which represents a continuum of possible vacuum states, none of which reflects the original symmetry. Choose

$$\langle \Phi \rangle_0 = \begin{pmatrix} v \\ 0 \end{pmatrix} \quad (1.18)$$

Expanding around the new vacuum state

$$\Phi' = \Phi - \langle \Phi \rangle_0 = \begin{pmatrix} \eta \\ \zeta \end{pmatrix} \quad (1.19)$$

substituting back into \mathcal{L} , we obtain

$$\mathcal{L}_{SO} = \frac{1}{2}[(\partial_\mu \eta)(\partial^\mu \eta) + 2\mu^2 \eta^2] + \frac{1}{2}[(\partial_\mu \zeta)(\partial^\mu \zeta)] \quad (1.20)$$

So there is now a field, η , with mass $-2\mu^2$, and a massless field ζ . The massless field is a Goldstone boson, and one Goldstone boson will be generated for each broken continuous symmetry of \mathcal{L} . This production of massless scalars is known as the Goldstone theorem [3]. The non-observation of massless scalars seems to exclude SSB as a mechanism in physical theories. If, however, one considers symmetries of the gauge group as opposed to the fields, a very useful result is obtained, as shown in the next section.

1.4 The Higgs mechanism

In section 1, local gauge symmetry was imposed on a \mathcal{L} , which resulted in the requirement of the photon field, as well as interactions between the particle fields and the photon field. However, the fact that the \mathcal{L} which contained the physical fields also reflected the original gauge symmetry, prevented the introduction of gauge particle masses. Because gauge particles are the carriers of force, and the weak force is known to be very short range, it is imperative to write down a \mathcal{L} which allows for massive gauge particles. The solution is known as the Higgs mechanism, and is the result of SSB applied to the $SU(2) \otimes U(1)$ symmetric electroweak sector of the SM \mathcal{L} .

1.4.1 Higgs in U(1)

The Higgs mechanism appears in the case of SSB in $U(1)$ when the phase invariance becomes a local requirement. Consider the \mathcal{L} for charged scalars [4]

$$\mathcal{L} = |\mathcal{D}^\mu \phi|^2 - \mu^2 |\phi|^2 - |\lambda| (\phi^* \phi)^2 - \frac{1}{4} F_{\mu\nu} F^{\mu\nu} \quad (1.21)$$

where

$$\phi = \frac{\phi_1 \pm i\phi_2}{\sqrt{2}} \quad (1.22)$$

and

$$\mathcal{D}_\mu = \partial_\mu + iqA_\mu \quad (1.23)$$

Again, the covariant derivative \mathcal{D}_μ allows the \mathcal{L} to remain invariant under the simultaneous transformations

$$\phi(x) \rightarrow e^{iq\theta(x)} \phi(x) \quad (1.24)$$

$$A_\mu(x) \rightarrow A_\mu(x) - \partial_\mu \theta(x) \quad (1.25)$$

If one chooses $\mu^2 > 0$, the result is a \mathcal{L} for charged scalars with a common mass μ . If one chooses $\mu^2 < 0$, the potential has a minimum for

$$\langle |\phi|^2 \rangle_0 = -\frac{1}{2} \frac{\mu^2}{|\lambda|} \equiv \frac{v^2}{2} \quad (1.26)$$

Choosing the vacuum to be the real part of ϕ

$$\langle \phi \rangle_0 = \frac{v}{\sqrt{2}} \quad (1.27)$$

$$\phi' = \phi - \langle \phi \rangle_0 \quad (1.28)$$

ϕ can be parameterized by

$$\phi = e^{i\zeta/v} (v + \eta) / \sqrt{2} \quad (1.29)$$

$$\simeq \frac{1}{\sqrt{2}} (v + \eta + i\zeta) \quad (1.30)$$

Substituting back into the \mathcal{L}_{SO} gives

$$\begin{aligned} \mathcal{L}_{SO} &= \frac{1}{2} [(\partial_\mu \eta)(\partial^\mu \eta) + 2\mu^2 \eta^2] + \frac{1}{2} [(\partial_\mu \zeta)(\partial^\mu \zeta)] \\ &- \frac{1}{4} F_{\mu\nu} F^{\mu\nu} - qv A_\mu (\partial^\mu \zeta) + \frac{q^2 v^2}{2} A_\mu A^\mu + \dots \end{aligned} \quad (1.31)$$

and it appears that we have generated another massless field, ζ , while also providing a mass for the gauge field, A_μ . The true particle spectrum is obscured by the term mixing A_μ and ζ ; but we still have free choice of our gauge. Picking the transformation

$$A_\mu \rightarrow A_\mu + \frac{1}{qv} \partial_\mu \zeta \quad (1.32)$$

$$\phi \rightarrow e^{-i\zeta/v} \phi = (v + \eta)/\sqrt{2} \quad (1.33)$$

This form of ϕ is then substituted back into equation (21), and

$$\mathcal{L}_{SO} = \frac{1}{2} \left[(\partial_\mu \eta)(\partial^\mu \eta) + 2\mu^2 \eta^2 \right] - \frac{1}{4} F_{\mu\nu} F^{\mu\nu} + \frac{q^2 v^2}{2} A_\mu A^\mu \quad (1.34)$$

The particle spectrum is now clear. The gauge field has a mass qv , the η field has a squared mass $-2\mu^2$, and the ζ field has disappeared. The reason for the disappearance is the new mass of the gauge field. Massless fields have only two polarizations (transverse) while massive ones have an additional longitudinal polarization. The ζ field has become the longitudinal polarization of the gauge field. So, when SSB is applied to locally symmetric Lagrangians, one avoids the appearance of Goldstone bosons, while solving the problems of massive gauge fields. However, one also generates new massive fields which appear in the physical spectrum, in the case the η field. This is the so-called Higgs field, and if the SM is correct, the Higgs must exist.

1.4.2 $SU(2) \otimes U(1)$

The symmetry group $SU(2)$ has generators τ_i which obey the Lie algebra [5]

$$\left[\frac{\tau_i}{2}, \frac{\tau_j}{2} \right] = i\epsilon_{ijk} \frac{\tau_k}{2} \quad (1.35)$$

where the τ_i are the Pauli matrices

$$\tau_1 = \begin{pmatrix} 0 & 1 \\ 1 & 0 \end{pmatrix}, \quad \tau_2 = \begin{pmatrix} 0 & -i \\ i & 0 \end{pmatrix}, \quad \tau_3 = \begin{pmatrix} 1 & 0 \\ 0 & -1 \end{pmatrix} \quad (1.36)$$

The generator of the $U(1)$ symmetry is a charge operator, but this is not the electric charge, it is hypercharge. Its coupling to the fields will therefore be written generally as g . A rotation in $SU(2)$ space is

$$\psi(x) \rightarrow \psi'(x) = e^{i\vec{\theta} \cdot \frac{\vec{\tau}}{2}} \psi(x) \quad (1.37)$$

and the $\psi(x)$ is an $SU(2)$ spinor field, while a rotation in $U(1)$ is

$$\psi(x) \rightarrow \psi'(x) = e^{iy\theta} \psi(x) \quad (1.38)$$

where y is the hypercharge carried by ψ . As usual, a locally invariant \mathcal{L} is required.

The covariant derivative in this case is [6]

$$\mathcal{D}_\mu = \partial_\mu + ig \frac{\vec{\tau} \cdot \mathbf{W}^\mu}{2} - \frac{ig'}{2} B^\mu \quad (1.39)$$

for left handed leptons, which form the left handed $SU(2)$ doublets

$$\begin{pmatrix} \nu_e \\ e^- \end{pmatrix}, \quad \begin{pmatrix} \nu_\mu \\ \mu^- \end{pmatrix}, \quad \begin{pmatrix} \nu_\tau \\ \tau^- \end{pmatrix} \quad (1.40)$$

and

$$\mathcal{D}_\mu = \partial_\mu - ig' B_\mu \quad (1.41)$$

for right handed fields. The choice of the Higgs field is a complex scalar doublet [7]

$$\phi = \frac{1}{\sqrt{2}} \begin{pmatrix} \phi_1 + i\phi_2 \\ \phi_3 + i\phi_4 \end{pmatrix} \quad (1.42)$$

Again, we pick $\mu^2 < 0$ in the Higgs potential, and pick a vacuum state for the Higgs field

$$\langle \phi \rangle_0 = \frac{1}{\sqrt{2}} \begin{pmatrix} 0 \\ v \end{pmatrix} \quad y = 1 \quad (1.43)$$

Although any choice of $\langle \phi \rangle_0$ will generate masses for the gauge particles, this particular choice is physically sound. The photon should remain massless, and

because charge is the generator of the $U(1)_{em}$ symmetry, a neutral field will leave this symmetry unbroken. And electric charge is

$$Q = T_3 + \frac{y}{2} \quad (1.44)$$

where T_3 is the third component of weak isospin. In this case

$$Q\phi_0 = 0 \quad (1.45)$$

So that

$$\phi'_0 = e^{iQ\theta(x)}\phi_0 = \phi_0 \quad (1.46)$$

and we will be left with a massless photon. The term in the \mathcal{L} relevant to the gauge particle masses is

$$\begin{aligned} & \left| \left(-ig\frac{\vec{\tau}}{2} \cdot \vec{W}_\mu - i\frac{g'}{2}B_\mu \right) \phi \right|^2 \\ &= \frac{1}{8} \left| \begin{pmatrix} gW_\mu^3 + g'B_\mu & g(W_\mu^1 - iW_\mu^2) \\ g(W_\mu^1 + iW_\mu^2) & -gW_\mu^3 + g'B_\mu \end{pmatrix} \begin{pmatrix} 0 \\ v \end{pmatrix} \right|^2 \\ &= \frac{1}{8}v^2g^2[(W_\mu^1)^2 + (W_\mu^2)^2] + \frac{1}{8}v^2(g'B_\mu - gW_\mu^3)(g'B_\mu - gW_\mu^3) \\ &= \left(\frac{1}{2}vg\right)^2 W_\mu^+ W_\mu^- + \frac{1}{8}v^2(W_\mu^3, B_\mu) \begin{pmatrix} g^2 & -gg' \\ -gg' & g'^2 \end{pmatrix} \begin{pmatrix} W_\mu^3 \\ B_\mu \end{pmatrix} \end{aligned} \quad (1.47)$$

So, there is a mass generated for the W^\pm of $(1/2)gv$, but the W_μ^3 and B_μ remain mixed. Diagonalizing the matrix in coupling constants reveals the particle spectrum. There are two neutral eigenvectors

$$\begin{aligned} A_\mu &= \frac{g'W_\mu^3 + gB_\mu}{\sqrt{g^2 + g'^2}} & m_A &= 0 \\ Z_\mu &= \frac{gW_\mu^3 - g'B_\mu}{\sqrt{g^2 + g'^2}} & m_Z &= \frac{1}{2}v\sqrt{g^2 + g'^2} \end{aligned}$$

So, the Higgs mechanism has successfully added masses to three of the four gauge particles associated with $SU(2) \otimes U(1)$ while leaving the fourth gauge particle massless. It has also, in the process, produced one massive scalar field which has yet to be discovered.

Of course, another course of action may be to drop gauge invariance altogether, and simply add the mass terms of fermions and gauge particles by hand. However, we would find upon doing this, a theory which is completely useless: gauge invariance insures that our theory is renormalizable, so divergent terms may be cancelled. Without this, infinite cross-sections could exist, and such results are clearly meaningless.

1.5 Beyond the SM Higgs

It is not known whether the SM Higgs scalar is truly the source of the gauge particle masses and fermion masses, or merely a useful trick. Other models of the Higgs sector should therefore be explored as alternative sources of masses. I will introduce such an alternative, and discuss efforts at Fermilab to discover one of the resulting massive scalar Higgs particles.

A minimal extension one might consider, and this coincides with the extension found in SUSY, is the addition of another complex scalar doublet [8].

$$\phi_1 = \begin{pmatrix} \phi_1^0 \\ \phi_1^- \end{pmatrix}, \quad \phi_2 = \begin{pmatrix} \phi_2^+ \\ \phi_2^0 \end{pmatrix} \quad (1.48)$$

where the superscripts refer to the eigenvalues of Q . The coupling of the doublets to the fermions is not unique, and I will choose (as in the Minimal Super-Symmetric Model (MSSM)) the scheme where ϕ_1 couples to up-type quarks and neutrinos, while ϕ_2 couples to down-type quarks and charged leptons. The usual SSB results in the choice

$$\langle \phi_1 \rangle_0 = \begin{pmatrix} v_1 \\ 0 \end{pmatrix}, \quad \langle \phi_2 \rangle_0 = \begin{pmatrix} 0 \\ v_2 \end{pmatrix} \quad (1.49)$$

leading to the popular definition

$$\tan \beta \equiv \frac{v_2}{v_1} \quad (1.50)$$

We started with two complex scalar doublets, or eight degrees of freedom in our Higgs sector. Three of the gauge particles (W^\pm, Z) acquire masses, leaving five degrees of freedom, which show up as observable fields. These are

$$H^\pm, \quad A^0, \quad H^0, \quad h^0$$

The charged Higgs couplings to the fermions is a part of the \mathcal{L} in which we can make a choice. The first choice is to allow one doublet to couple to both up and down type quarks, while the other couples to no quarks at all. The second choice to to allow one doublet to couple only to up-type quarks, while the other couples only to down-type. This second choice, the so-called Model II coupling, insures that at tree level, we have no H^+ mediated flavor changing neutral currents (a process forbidden in the SM).

In the case of the Model II couplings, the H^+ couplings to the fermions are given by:

$$\mathcal{L}_{H^+ \bar{U} D} = \frac{g}{2m_W \sqrt{2}} \left(H^+ \bar{U} [m_U \cot \beta K(1 - \gamma_5) + m_D \tan \beta K(1 + \gamma_5)] D \right) \quad (1.51)$$

where U and D are the up and down fermions, and K is the CKM matrix for the quarks, and the identity for the leptons. If $m_{H^+} < m_t - m_b$, then $t \rightarrow H^+ b$ can have a significant branching ratio (BR).

The coupling of the H^+ to fermions is proportional to the fermion mass, so if a H^+ decays to a lepton, it will decay to the heaviest allowed, the τ , and if it decays to quark pairs, it will again choose the heaviest, $c\bar{s}$. In fact, when M_{H^+}

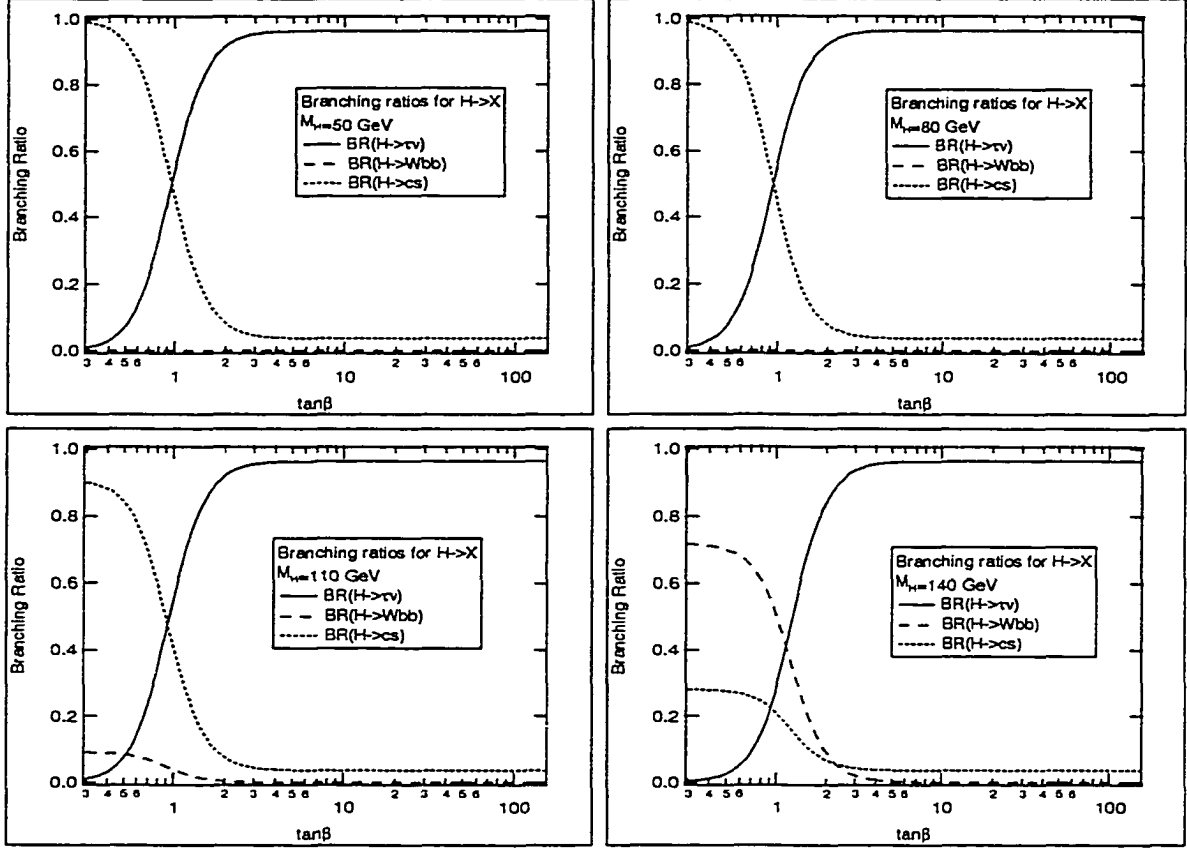


Figure 1.1: Branching ratios for the three possible final states of H^+ decay.

becomes large, the decay $H^+ \rightarrow W^+ b \bar{b}$, via a virtual top becomes important in the region of low $\tan\beta$, as indicated in figure 1.1. The dependence of $BR(t \rightarrow H^+ b)$ on M_{H^+} , $\tan\beta$ is shown in figure 1.2.

Lepton universality dictates that the W couple equally to all leptons, and one should therefore find equal numbers of $W \rightarrow l$ in a collection of $t\bar{t}$ decays. Because of the nature of the Higgs coupling, an abundance of events of the type $t\bar{t} \rightarrow \tau + jets$ is the signature sought in this analysis. This type of search [10] probes the region $\tan\beta \geq 1$.

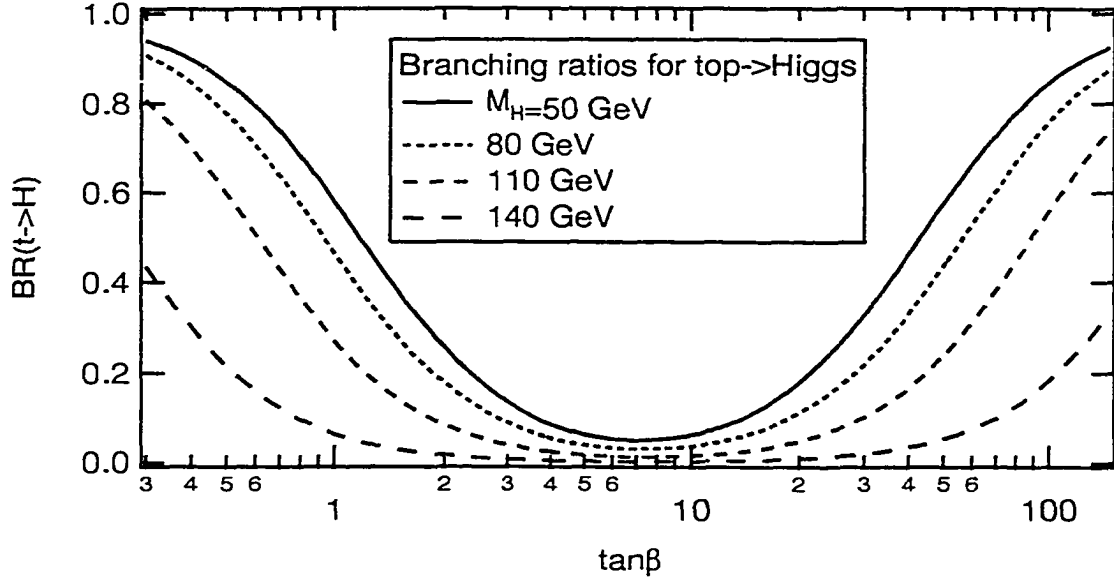


Figure 1.2: Branching ratios of top to charged Higgs, for various M_{H^\pm} .

Final state	First decay	Secondary decays	BR for secondary decays
1	$t\bar{t} \rightarrow W^+W^-b\bar{b}$	$W^+ \rightarrow \tau^+\nu_\tau, W^- \rightarrow l$	0.025
2	$t\bar{t} \rightarrow W^+W^-b\bar{b}$	$W^+ \rightarrow \tau^+\nu_\tau, W^- \rightarrow jets$	0.15
3	$t\bar{t} \rightarrow W^+H^-b\bar{b}$	$W^+ \rightarrow \bar{l}, H^- \rightarrow \tau\bar{\nu}_\tau$	0.11
4	$t\bar{t} \rightarrow W^+H^-b\bar{b}$	$W^+ \rightarrow jets, H^- \rightarrow \tau\bar{\nu}_\tau$	0.68
5	$t\bar{t} \rightarrow H^+H^-b\bar{b}$	$H^+ \rightarrow \tau^+\nu_\tau, H^- \rightarrow \tau\bar{\nu}_\tau$	1

Table 1.1: Decay modes, and their branching ratios, for $t\bar{t} \rightarrow \tau + X$, given a H^+ .

1.5.1 Experimental signatures

For $\tan\beta \simeq 3$ or greater, a search for violation of lepton universality in $t\bar{t}$ events can be based on a comparison of the final states given in Table 1.1, where l refers to each individual charged lepton (e, μ, τ). Unlike the other leptons, the τ decays before reaching any of the detector elements, and must be identified through its decay products. Such identification at $D\phi$ relies only on the hadronic decays, which constitute 64.5% of all τ decays. Table 1.2 lists the available top quark pair decay modes which we use for this search, and the BR s and final states for each.

The first final state in Table 1.1 has a very small BR , and is therefore not useful. Although final state 2 also has a small BR , it is important because it represents

Final state	BR	Topology of final state
2	0.1	$5jets + \cancel{E}_T$
4	0.44	$5jets + \cancel{E}_T$
5	0.42	$4jets + \cancel{E}_T$

Table 1.2: Final states leading to the $t\bar{t} \rightarrow \tau + jets$ topologies used in this analysis. Final states 2 and 4 include their charge-conjugate reactions.

the SM contribution to the inclusive τ yield for $t\bar{t}$ events. The third final state is also not considered a useful channel. Because we will rely on a violation of lepton universality in what is expected to be a small number of selected events, the violating channel must therefore have a much larger BR than the yield from the SM, if a statistically significant statement is to be made. Final states 4 and 5 have large BR s, and are consequently considered useful channels. For details on the partial widths used in the calculation of $BR(t \rightarrow X)$, and $BR(H^+ \rightarrow X)$, the reader is referred to the DØ note for the indirect search results, [9].

Chapter 2

The Experiment

2.1 Accelerator complex

The Fermilab Tevatron [13] is currently world's highest energy particle accelerator. It collides beams of protons (p) and anti-protons (\bar{p}) each having an energy of 900 GeV, achieving a total center of mass energy of 1.8 TeV. A schematic of the Fermilab complex is shown in Figure 2.1. The major subsystems are:

- Pre-accelerator
- Linac
- Booster
- Main Ring
- anti-proton source
- anti-proton Debuncher and Accumulator
- Tevatron

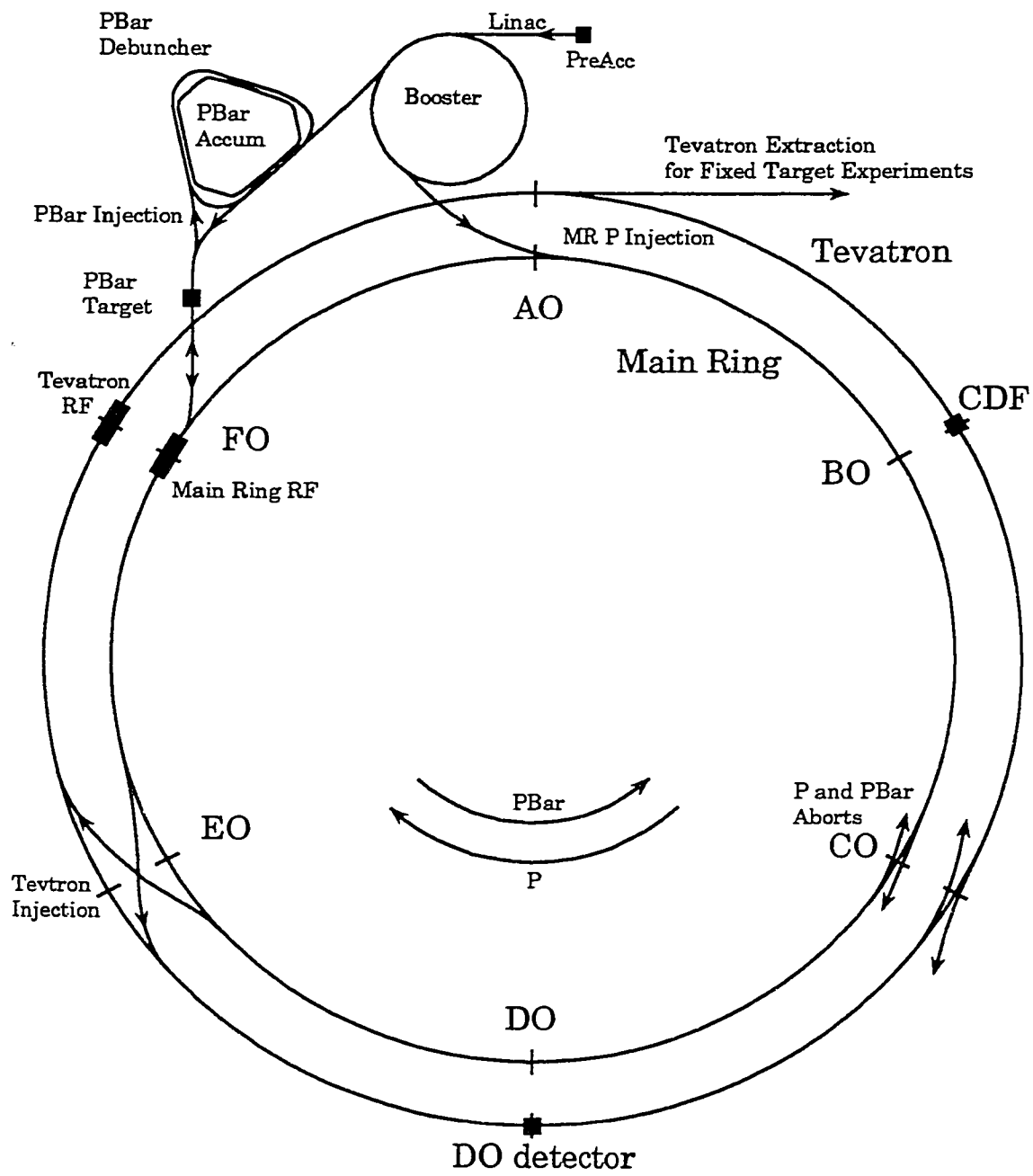


Figure 2.1: Layout of the Fermilab accelerator complex (not to scale).

The source of protons for use in Fermilab begins in the pre-accelerator. Here, H_2 molecules are transformed into H^- ions when they collide with electrons at the surface of a catalyst, in a device called the magnetron. H^- ions leave the magnetron with an energy of 18 keV, and enter a Cockroft-Walton accelerator, a solid-state device which accelerates the ions to an energy of 750 keV in cycles of 15 Hz.

Upon leaving the pre-accelerator, the H^- bunches enter the Linac, a 150 meter linear accelerator which increases the H^- energy to 200 MeV for run IA, and 400 MeV for runs IB and IC. The Linac applies an RF field to the H^- bunches during a short time while the bunches are gaps between drift tubes. While in the drift tube, the H^- are collimated and move at constant velocity. The first stage of the Linac operates at 201.24 MHz, while the second stage operates at 805 MHz. Upon reaching the end of the Linac, the H^- ions are passed through a carbon foil, which strips the electrons, leaving only the proton.

The protons enter the booster, which is a 151 meter radius synchrotron operating at 15Hz. The booster can hold up to 84 bunches of protons, each bunch consisting of 6 merged bunches from the Linac. Here, the energy of the protons is boosted to 8 GeV.

The Main Ring is the next stage for the 8 GeV protons. Prior to the construction of the Tevatron, the Main Ring was the highest energy accelerator in the world, operating at a maximum of 400 GeV. The Main Ring is a 1000 meter radius synchrotron, which directs the protons using 774 water-cooled dipole magnets. The beam is re-focused using a series of 240 quadrupole magnets. The Main Ring lies in a plane everywhere, except at the B0 and D0 interaction points. At B0, the particles are bent 19 feet above the plane, and at D0 they are bent 89.2 inches above the plane. This allows room for placement of the detectors.

Certain proton bunches are extracted from the Main Ring after being accelerated to 120 GeV, and directed onto a target of Ni. The result is a spray of particles,

some of which will be anti-protons. The maximum yield is 10^7 anti-protons for every 10^{12} protons. The particles emerging from the Ni target pass through a solid Li cylinder, such that the average particle velocity is along the axis of the cylinder. The Li cylinder carries large pulses of current (500,000 A) anti-aligned with the average particle velocity, and the result is that all positively charged particles are de-focused, and all negatively charged particles are focused along the cylinder axis.

A pulsed dipole magnet selects 8 GeV anti-protons from the anti-proton source, and directs them into the Debuncher/Accumulator. The Debuncher is a storage ring in which the anti-proton bunches are rotated in phase space from a point with large momentum uncertainty and small time uncertainty, to a point with small momentum and large time uncertainties. The bunches are then stochastically “cooled”. This is a process in which corrective signals are applied to the orbits of the bunches. Because the influence of other particles in the beam is quite large, the effect of any single corrective signal is small, but the accumulated effect of many corrections is large. The particles are transferred into the Accumulator before the next cycle of anti-proton production from the Main Ring, which occurs at 2.4 second intervals. In the Accumulator, the anti-protons are cooled for several hours, until their injection back into the Main Ring.

The final phase in the life cycle of protons and anti-protons at Fermilab is injection into the Tevatron. Bunches of protons or anti-protons are injected at 150 GeV into the Tevatron from the Main Ring, where they are accelerated to as much as 900 GeV. Because of their opposite sign charge, protons and anti-protons are able to share the same beam-pipe and RF fields. The dipoles and quadrupoles in the Tevatron operate at 4.6 K, and are super-conducting. In the collider mode, six bunches of protons and anti-protons travel around the accelerator and are made to cross at the two interaction points. The B0 region houses the CDF detector, while D0 occupies the D0 region. The same six bunches are used over the course of about 18 hours, at which time the luminosity is too low to be useful. During the

operation of the Tevatron, the Main Ring continuously creates new anti-protons, so that the Tevatron may run uninterrupted.

2.2 The DØ Detector

The DØ detector [11] [12], shown in figure 2.2, is a large, multipurpose detector used in the study of proton-antiproton collisions at the Fermilab Tevatron.

Discussion of the detector will refer to a right handed coordinate system, in which the positive z-axis is along the proton direction, and y points up. The azimuthal and polar angles are denoted ϕ and θ , respectively, where $\theta = 0$ is aligned with the z-axis. If the quantity θ we to be used in calculations involving two different physics objects in an event, the rest frame of each of those objects would have to be known; θ is not a Lorentz invariant. For that reason, we choose to use the pseudo-rapidity, defined by:

$$\eta = -\ln \left(\tan \left(\frac{\theta}{2} \right) \right) \quad (2.1)$$

which is a good approximation to the true rapidity:

$$y = \ln \left(\frac{E + p_z}{E - p_z} \right) \quad (2.2)$$

when $m \ll E$.

The units used in data analysis warrant some comment. The intensity of the proton anti-proton beams is measured in units of *Luminosity*, \mathcal{L} , which has units $\text{cm}^{-2} \text{s}^{-1}$. The probability per unit of \mathcal{L} that a particular kind of interaction will take place is called a *cross-section*, σ , and has units of area; the unit commonly used in particle physics is the *barn*, where $b \equiv 10^{-24} \text{ cm}^2$. These definitions provide a convenient measure of the reaction rate R for some process:

$$R = \mathcal{L}\sigma \quad (2.3)$$

♦

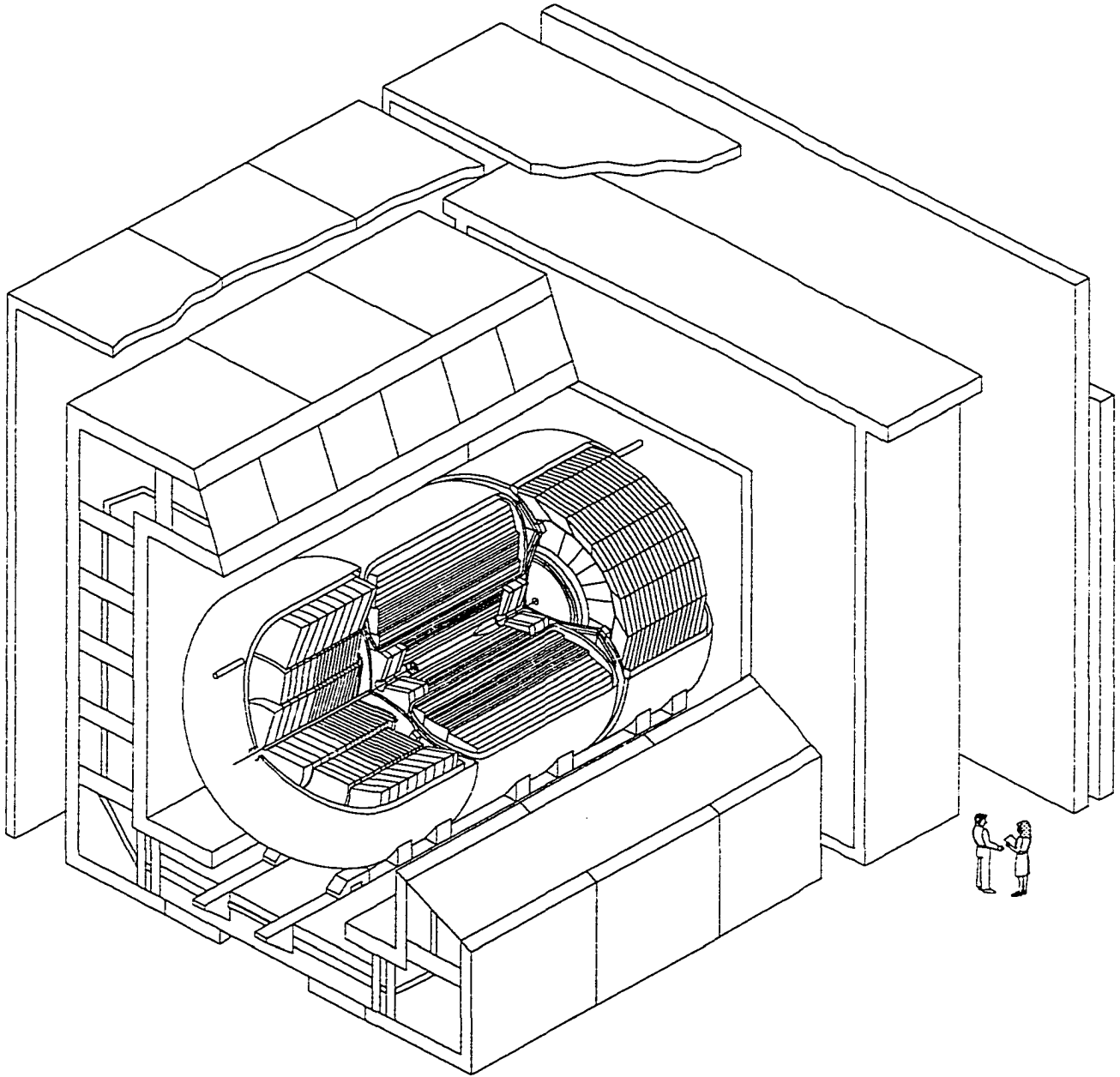


Figure 2.2: Cutaway view of the DØ detector.

And the total number of events N_e expected from some process over time is calculated in terms of the integrated luminosity:

$$N_e = \sigma \int \mathcal{L} dt \quad (2.4)$$

The central detector is comprised of four major subsystems, whose primary function is to enable reconstruction of three dimensional tracks of charged particles. The innermost section is the vertex drift chamber (VTX). The VTX is surrounded by the transition radiation detector (TRD). The TRD is inside the central drift chamber (CDC), and capped on either side by the forward drift chamber (FDC).

Resolution of tracks enable one to distinguish electromagnetic showers arising from electrons, or γ/π^0 . Measurements of dE/dx allow one to determine whether a track is due to a single particle, or multiple tracks closely spaced, as one might expect for $\gamma \rightarrow e^+e^-$. The central detector also uses timing information to determine the z position of the interaction.

2.2.1 Drift Chamber Principles

When a charged particle travels through a gas, it interacts with electrons bound to atoms in the gas, liberating them and producing electron-ion pairs. In the presence of an electric field, the electrons would drift toward the anode, encountering other atoms along the way, and, if enough energy is available, liberating one of its electrons. This exponential rise in the number of free electrons is called an avalanche. When the avalanche arrives at the anode, a current signals the passage of a charged particle. The ratio of the final number of electrons to the initial number deposited is called the gas gain. The very high electric field needed to produce a large avalanche, and hence a large signal, is achieved by using a small diameter wire as the anode, or sense wire. Moreover, because the chamber geometry results in a field which is nearly constant far from the sense wire, the drift velocity of the electrons is nearly constant, and the time required for the avalanche to arrive can

be used as a measure of the distance of closest approach of the incident particle. In addition, the drift velocity of electrons flattens out considerably for large electric fields (1kV/cm) ,[17]Fig 10.3, and a large electric field is therefore desirable.

2.2.2 Vertex Drift Chamber

The VTX [16] is used to find the vertex position and paths of charged particles, as well as identifying charged particles which arise from conversions in the TRD. Four concentric carbon fiber cylinders enclose the three layers which make up the VTX. The inner layer has sense wires arranged in a jet geometry which are 97cm long, and each successive layer has wires 10cm longer than the previous one. Figure 2.3 shows an end view of the VTX, and Table 2.1 details the chamber parameters.

The sense wires are staggered by $100\mu m$ in each cell in order to resolve the

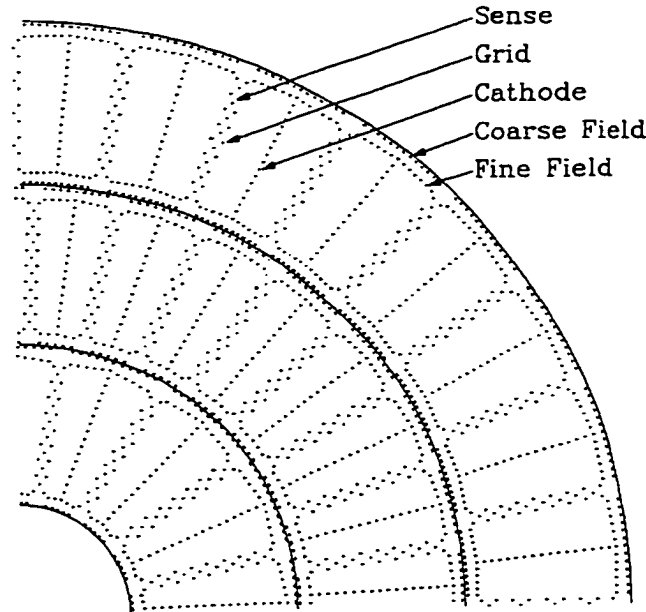


Figure 2.3: End view of the vertex chamber.

ambiguity of whether a particle passes to the left or right of a sense wire. The $r\phi$ position of a hit are determined by the wire hit, and the drift time. The z position is determined by charge division along the sense wire.

Active Radius	3.7cm - 16.2 cm
Number of Layers	3
Active lengths of each layer (cm)	96.6, 106.6, 116.8
Number of cells in each layer	16, 32, 32
Sense Wire separation	4.57mm radially with 100 μ m stagger
Sense Wire specs	25 μ m NiCoTin, 80g tension
Sense Wire Voltage	+2.5 kV
Field Wire specs	152 μ m Au-plated Al, 360g tension
Gas composition	CO_2 95%, $2CH_3$ 5%, H_2O 0.5%
Gas pressure	1atm
Average Drift Field	1kV/cm
Drift Velocity	$\approx 7.3\mu m/ns$
Maximum drift distance	1.6cm
Gas gain	4×10^4
Position resolution	$r\phi \approx 60\mu m, z \approx 1.5cm$

Table 2.1: Vertex Drift Chamber Parameters.

2.2.3 Transition Radiation Detector

Transition radiation has proven a useful tool in the identification of high energy electrons. When an electron travels through a material with a low dielectric constant, the polarization of the material has a small effect on the electron's field so that it has a large spatial extent. When the electron traverses a boundary to a material with a higher dielectric constant, the sudden redistribution of charge in the medium as a result of the electron's changing field results in radiation. At high energies, this radiation is emitted primarily as X-rays. The total energy emitted upon crossing a single surface is:

$$W = \frac{2}{3}\alpha\omega_p\gamma \quad (2.5)$$

Note that the energy emitted increases linearly with the Lorentz factor. The emitted radiation is forward, and contained in a cone of $\theta \sim 1/\gamma$. A TRD is therefore quite useful for the separation of particles with equivalent energies, but different masses. The large difference in mass between electrons and mesons/hadrons therefore makes the TRD a good discriminator.

The DØ TRD consists of three separate units, each containing a radiator and an X-ray detection chamber. The radiator section of each unit consists of 393 foils of $18\mu\text{m}$ thick polypropylene in a volume filled with N_2 . The gap between foils is $150 \pm 150\mu\text{m}$. The gaps are maintained with a pattern embossed on the surface of the polypropylene. For the DØ radiator configuration, the transition radiation X-rays have an energy distribution which peaks at 8 keV, and is mostly contained below 30 keV.

X-ray detection occurs in a drift chamber just outside the radiator. Charged collected in the drift chamber results from transition radiation X-rays, and ionization produced by all charged particles traversing the chambers. The magnitude and time of arrival of charge are both used to distinguish electrons from hadrons.

The outer support of each TRD unit is a 1.1 cm thick plastic honeycomb with fiberglass skins. The radiator and detector volumes are separated by a pair of $23\mu\text{m}$ windows. Dry CO_2 is circulated between these windows to prevent the N_2 in the radiator volume from polluting the gas in the detector volume, which is a mixture of $Xe(91\%)$, $CH_4(7\%)$, $C_2H_6(2\%)$. The thickness of the TRD at normal incidence is 8.1% of a radiation length, and 3.6% of an interaction length.

2.2.4 Central Drift Chamber

The CDC provides tracking at large angles, out to about $|\eta| \leq 1.2$, and lies outside the TRD, and just inside the calorimeter. Its geometry is cylindrical, with a physical length of 184cm. The detector consists of four concentric rings, each containing 32 cells. Like the VTX, its sense wires have a jet geometry, with sense wires staggered by $200\mu\text{m}$ to help resolve left-right ambiguities. In addition, cells are offset by one half between each layer. This provides an average drift distance of $\approx 7\text{cm}$. Each cell is constructed from Rohacell foam wrapped in epoxy coated Kevlar cloth, and wrapped with a double layer of $50\mu\text{m}$ Kapton. Grooves are cut

Active radius	51.8 - 71.9 cm
Number of layers	4
Active length	179.4, 106.6, 116.8 cm
Number of cells per layer	32
Number of sense wires	7/cell, 896 total
Sense wire separation	6.0 mm radially, 200 μm stagger
Sense wire specs	30 μm Au-plated W, 110 g tension
Sense wire voltage	+1.45 kV (inner) - +1.58 kV (outer)
Number of Delay lines	2/cell, 256 total
Delay line velocity	2.34 mm/s
Field wire specs	125 μm Au-plated CuBe, 670 g tension
Gas composition	Ar 93%, CH_4 4%, CO_2 3%, H_2O 0.5%
Gas pressure	1 atm
Average drift field	620 V/cm
Drift velocity	$\approx 34 \mu\text{m}/\text{ns}$
Maximum drift distance	7 cm
Gas gain	2×10^4 (inner SW) - 6×10^4 (outer SW)
Position resolution	$r\phi \approx 180 \mu\text{m}$, $z \approx 2.9 \text{ mm}$

Table 2.2: Central Drift Chamber Parameters.

into the cell walls to accommodate teflon tubes containing inductive delay lines which lie in the planes of the cell's seven sense wires. The $r\phi$ hit is determined with the wire hit and drift time, while the z position is determined via the delay lines. The inner radius of the CDC is comprised of a composite carbon fiber/Rohacell tube to minimize conversions, and the outer radius is made of 0.95cm Al, and serves at the support structure. Table 2.2 details more completely the CDC parameters.

2.2.5 Forward Drift Chambers

The FDC extends the outer tracking to coverage to $\eta \approx 3.1$. This section of the detector lies just outside the VTX, TRD and CDC, and just inside the end calorimeter. Its outer radius is somewhat smaller than that of the CDC to allow passage of cables from the interior chambers. Each FDC is constructed from three separate layers of chambers: two layers measuring Θ which sandwich one

	Θ modules	Φ modules
Active z extent	104.8 - 111.2 cm 128.8 - 135.2 cm	113.0 - 127.0 cm
Number of cells per layer	4 quads of 6 cells	32
Number of sense wires	8/cell, 384/FDC	16/cell, 576/FDC
Sense wire separation	8.0 mm radially with 200 μ m stagger	
Sense wire specs	30 μ m Au-plated W, 50 - 100g tension	
Sense wire voltage	+1.55 kV	+1.66 kV
Number of delay lines	1/cell, 48/FDC	none
Delay line velocity	2.35 mm/ns	NA
Field wire specs	163 μ m Au-plated Al, 100 - 150 g tension	
Gas composition	Ar 93%, CH_4 4%, CO_2 3%, H_2O 0.5%	
Gas pressure	1 atm	
Average drift field	1.0 kV/cm	
Drift velocity	40 μ m/ns	37 μ m/ns
Maximum drift distance	5.3 cm	
Gas gain	2.3 $\times 10^4$ (inner SW) 5.3 $\times 10^4$ (outer SW)	3.6 $\times 10^4$
Position resolution (drift)	$\approx 300 \mu$ m	$\approx 200 \mu$ m

Table 2.3: Forward Drift Chamber Parameters.

layer measuring Φ . The Φ layer is a single chamber consisting of 36 sectors, each with 16 anode wires which are parallel to z . The Θ layers are comprised of four mechanically separated sections, each composed of six rectangular cells arranged in increasing radii. Each cell contains eight sense wires which are parallel to z . The two Θ layers are rotated with respect to each other by 45 degrees. The sense wires in all modules are staggered by 200 μ m to help resolve left-right ambiguities. Table 2.3 shows the FCD parameters in more detail.

2.3 Calorimeter

2.3.1 Principles of Calorimetry

A calorimeter ([18], pg 257) is a device into which a particle deposits energy, through a series of interactions which produces successively lower energy particles.

This collection of particles is termed a *shower*. Some of the energy will be deposited in a practical, detectable form such as scintillation light, Cherenkov light, ionization charge, etc. Advantages of using calorimeters over mass spectrometers include:

- Sensitive to charged and neutral particles
- Energy Resolution improves $1/E^{1/2}$
- Length of the detector scales logarithmically with particle energy. A magnetic spectrometer scales as $p^{1/2}$ for a given relativistic momentum resolution $\Delta p/p$

For electrons and positrons, the primary mechanism for energy loss in matter is bremsstrahlung, and for photons it is pair production, for energies above approximately 1 GeV. When one of these electromagnetic (EM) objects loses energy, it produces other, lower energy EM objects; it is through a succession of these processes that the electromagnetic cascade (EMC) is formed. The process giving rise to the EMC is fully described by QED, and essentially depends on the density of electrons in the absorber medium; it is for that reason that the EMC properties can be described in a material independent way, using the *radiation length*, X_0 . The amount of energy lost through radiation is:

$$(dE)_{\text{radiation}} = -E \frac{dx}{X_0}, \quad X_0 \approx 180AZ^{-1} \quad (2.6)$$

Lower energy portions of the EMC are governed by lower energy processes, ionization loss and excitation, collectively termed collision losses. The energy lost to collisions also decays exponentially with X_0 :

$$(dE)_{\text{collision}} = -\epsilon \frac{dx}{X_0}, \quad \epsilon(\text{MeV}) \approx 550Z^{-1} \quad (2.7)$$

where ϵ is the *critical energy* of the medium.

Hadronic cascades (HC) are fundamentally different from EMCs, and no simple analytic description of the HC shower exists. Hadrons lose energy mainly through

non-elastic collisions with nuclei. There are two major limitations to the energy resolution of hadronic calorimeters. First, a large number of the secondaries are π^0 s, which will continue to lose energy electromagnetically, without any nuclear interactions. Second, a sizeable amount of the incident particles energy will be spent breaking up or exciting nuclei. Only a small fraction of this energy is visible. Dimensions of a HC scale with λ , the absorption length, or interaction length. Hadronic showers are much more extended spatially than EMC of the same energy.

A homogeneous calorimeter is one in which the absorbing material is continuous throughout the particle shower. Examples of this type are NaI, and lead-glass (glass loaded with 50-60% PbO). Homogeneous detectors have the best energy resolution, but have the drawback that one can only measure the total energy deposited. Information on the shower shape, important in the discrimination of leptons and hadrons, is lost.

An alternative approach to calorimetry is to alternate layers of active material and absorber material. One instantly sees one advantage to this design: A more compact detector can be designed, because a very high Z absorber can be used without concern for whether that absorber will also produce a signal. In addition, the active portion of the detector may be chosen for its signal response without concern for its ability to absorb energy. Such a device is called a *sampling calorimeter*. The disadvantage of this design is that only a fraction of the deposited energy is measured, resulting in additional fluctuations in the energy measurement.

Particles incident on a detector in a physics experiment typically come in the form of complicated jets, which may contain both hadrons and leptons. Because of the energy lost in nuclear processes and neutrinos produced in hadronic decays, the response of the calorimeter (homogeneous or sampling) will be different for hadrons and leptons. The ratio of a calorimeter's response to pions and electrons, quantifies this difference. If this ratio is close to one, fluctuations in the decay of a particular hadron will not affect the resolution of the energy measurement of that

hadron, and for jets comprised of decaying hadrons. A calorimeter with $e/\pi \approx 1$ is said to be *compensating*. The e/π ratio for the DØ detector ranges from 1.08 at 10GeV to about 1.03 at 150GeV [19].

For a localized deposit of energy (jet) with mean value μ , and error σ , the energy resolution of the DØ detector is parameterized by:

$$\left(\frac{\sigma}{\mu}\right)^2 = C^2 + \frac{S^2}{E} + \frac{N^2}{E^2} \quad (2.8)$$

where E is the beam energy in GeV, S is due to statistical errors in sampling, C is a constant term reflecting such effects as momentum spread of the beam, upstream energy losses and shower leakage, and unequal response to to EMC and HC, and N accounts for energy-independent contributions such as electronic and Uranium noise. For electrons, the measured parameters are:

$$C = 0.003 \pm 0.002, S = 0.157 \pm 0.005, N \approx 0.140 \quad (2.9)$$

and for pions:

$$C = 0.032 \pm 0.004, S = 0.41 \pm 0.04, N \approx 1.28 \quad (2.10)$$

2.3.2 Calorimeter Geometry

The DØ detector uses liquid Ar (LAr) as an ionization medium, and depleted Uranium as the primary absorber. Cu and stainless steel are used as absorber materials in the outer portions of the detector. Each module in the calorimeter contains several layers of absorber plates, separated from each other by a LAr filled gap of 2.3mm. The signal is read out on a Cu pad sandwiched between two 0.5mm thick pieces of G10, covered with a resistive epoxy coating. The calorimeter is operated with the Cu pad at ground, and the epoxy held at 2.0-2.5 kV. When charged particles pass through the LAr, they leave a trail of ionization, which is collected on the epoxy coating, and read out on the Cu plate via capacitive

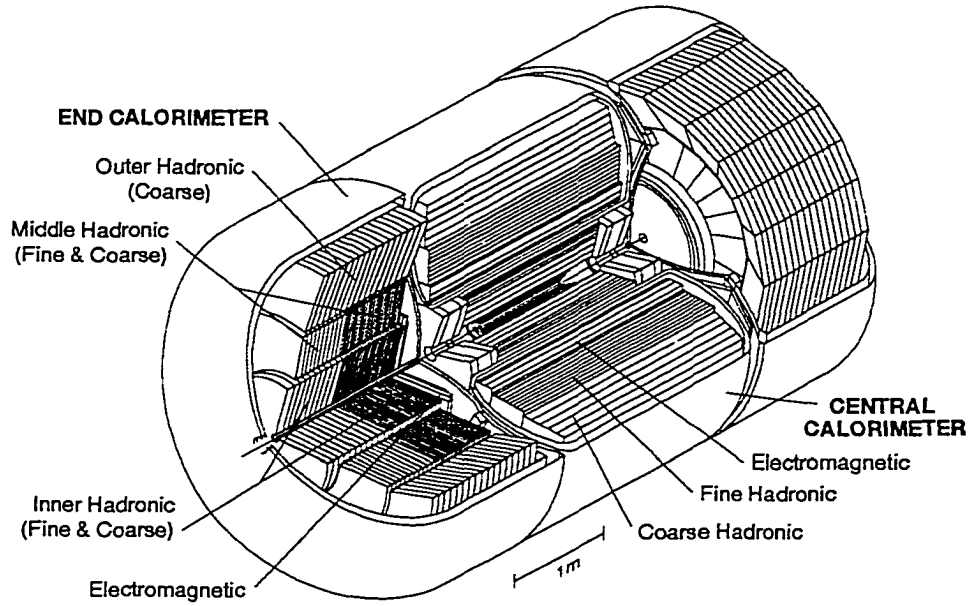


Figure 2.4: Cutaway view of the calorimeter.

coupling. Each signal board is sub-divided into smaller sections to help resolve the transverse shower dimension. Corresponding cells in adjacent boards are ganged together to form *readout cells*.

The transverse sizes of cells were chosen to be comparable to the transverse sizes of showers: 1-2 cm for EMC, and about 10cm for HC. The typical size of jets is $\sqrt{\Delta\eta^2 + \Delta\phi^2} \approx 0.5$. Finer segmentation allows for the determination of shower shape.

Figure 2.4 shows a cut-away view of the calorimeter. In order to allow access to the central detector, the calorimeter is divided into three major components: the central calorimeter (CC), and the end calorimeter (EC).

The CC contains three concentric layers of modules. The inner layer contains 32 EM modules, which absorb most of the EM energy. The middle layer contains 16 fine hadronic (FH) modules, which contain most of the energy due to hadronic

decays. The outer layer contains 16 course hadronic (CH) layers. The CH measures leakage out of the FH, and reduces the amount of energy lost due to punchthrough.

The EC also contains three concentric layers of modules. The center layer has modules ordered EM, FH, CH. The second layer has modules ordered FH, CH, and the outer layer contains only CH modules. Tables 2.4 , 2.5 detail important parameters of the CC and EC. There is a region of between the CC and EC

Central Calorimeter			
Module type	EM	FH	CH
η coverage	± 1.2	± 1.0	± 0.6
Number of modules	32	16	16
Absorber	DU	Du-Nb	Cu
Absorber thickness (mm)	3	6	46.5
Number of signal boards	21	50	9
Number of readout layers	4	3	1
Cells per readout layer	2,2,7,10	20,16,14	9
Total X_0 at $\eta = 0$	20.5	96.0	32.9
Total λ at $\eta = 0$	0.76	3.2	3.2
Sampling fraction (%)	11.79	6.79	1.45
Total readout cells	10,368	3000	1224

Table 2.4: Parameters of the Central Calorimeter

End Calorimeter						
Module type	EM	IFH	ICH	MFH	MCH	OH
η coverage	1.3-3.7	1.6-4.5	2.0-4.5	1.0-1.7	1.3-1.9	0.7-1.4
Num of modules	1	1	1	16	16	16
Absorber	DU	DU-Nb	SS	DU-Nb	SS	SS
Thickness (mm)	4	6	6	6	46.5	46.5
LAr gap (mm)	2.3	2.1	2.1	2.2	2.2	2.2
Signal boards	18	64	12	60	14	24
R.O. layers	4	4	1	4	1	3
Cells/r.o layer	2,2,6,8	16	14	15	12	8
Total X_0	20.5	121.8	32.8	115.5	37.9	65.1
Total λ	0.95	4.9	3.6	4.0	4.1	7.0
Sampling frac (%)	11.9	5.7	1.5	6.7	1.6	1.6
Total r.o. cells	7488	4288	928	1472	384+64+896	

Table 2.5: Parameters of the End Calorimeter

containing no active material, due to the calorimeter's cryostat walls and support

structures. Two additional devices, the massless gaps (MG) and inter-cryostat detectors (ICD), are used to recover some of the energy in this dead region. The MG consist of signal boards mounted on the end plates CCFH, ECMH, and ECOH modules. The ICD consists of a ring of scintillation counters mounted on the EC end-plates. Both the ICD and MG have a segmentation of 0.1×0.1 in η , ϕ .

2.4 Muon System

The calorimeter of DØ is designed to contain all particles which interact hadronically and electromagnetically. As mentioned, the primary mechanism of energy loss at $\geq 1\text{GeV}$ is bremsstrahlung. Every standard model (SM) particle produced is therefore stopped, except muons and neutrinos. Muons do not interact hadronically, and their mass is too high to interact appreciably via EM at Tevatron energies. In addition, one cannot rely on a measurement of the μ decay products, because its long lifetime of $2.2\mu\text{s}$ carries it outside of the detector. The purpose of the muon detector is to measure the transverse momentum, and the position of μs .

The muon system [20] is made up of five separate Fe toroidal magnets, collectively called the wide angle muon system (WAMUS) and small angle muon system (SAMUS), surrounded on top and bottom by proportional drift tubes (PDT), which measure track coordinates to an accuracy of 3cm. The particle trajectory is determined by combining information from the central tracker, the calorimeter, and the inner set of PDTs. As the muon traverses the Fe, its direction is changed by the magnetic field, and its momentum can be determined by comparing the track direction before entering and after exiting the toroid. Multiple scattering in the Fe limits the relative momentum resolution to about 18%. The charge of the muon can be determined with 3σ confidence for $p_T < 200\text{GeV}$ $\eta = 0$, $p_T < 30\text{GeV}$ $|\eta| = 3.3$.

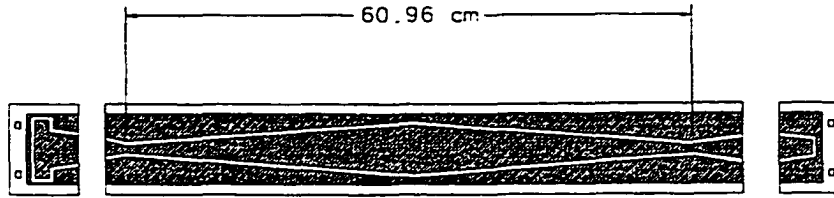


Figure 2.5: Section of cathode pads found in muon chamber drift tubes.

2.4.1 WAMUS

One central magnet (CF), two end magnets (EF), and their associated PDTs make up the WAMUS. These PDTs have a rectangular cross section and contain one sense wire per cell. They are arranged in three layers: one just inside the magnet (A), one just outside the magnet (B), and one 1-3 m away from the magnet (C). The CF is a square annulus covering $|\eta| < 1.0$, while the EFs cover $1.0 < |\eta| < 2.5$, and are made of a flat, square Fe plate with a square hole in the center. Both CF and EF carry a current of 2500 A. In order to allow the drift time to measure the deflection due to the magnetic field, the drift tubes are oriented approximately parallel to the magnetic field. The hit resolution is about 0.5 mm.

The readout of the PDTs occurs at one end only, and the far end has adjacent sense wires jumpered together. The difference in the arrival time of signals from the jumpered end of a pair of wires, and the near ends of those sense wires provides a measurement of the hit position along the wire with an accuracy of about 20cm. A more precise measurement is made using cathode pads inserted at the top and bottom of each tube (Fig 2.5). These pads are constructed from Cu-clad Glasteel, where the Cu-cladding forms two independent electrodes in an inner/outer repeating diamond pattern, whose period is about 61 cm. The ratio of charge deposited on the inner/outer pads can be used to localize the hit to about 3 mm, modulo 30cm, which can be resolved with the course timing measurement.

	WAMUS	SAMUS
Rapidity coverage	$ \eta < 1.7$	$1.7 < \eta < 3.6$
Magnetic Field	2T	
λ	≈ 13.4	≈ 18.7
Number of modules	164	6
Number of drift cells	11,386	5308
Sense wire specs	50 μ m Au-plated W 300g tension	
Max sagitta	0.6 mm	2.4 mm
Sense wire voltage	+4.56 kV	+4.0 kV
Cathode pad voltage	+2.3 kV	NA
Gas composition	Ar93%, CF ₄ 5% CO ₂ 5%	CF ₄ 90%, CH ₄ 10%
Bend view resolution	± 0.53 mm	± 0.35 mm
Non-bend view resolution	± 0.3 mm	± 0.35 mm
Average drift velocity	6.5 cm/ μ s	9.7 cm/ μ s
Maximum drift distance	5 cm	1.45 cm

Table 2.6: Parameters for the WAMUS and SAMUS.

2.4.2 SAMUS

The higher occupancy of the forward regions require a finer hit resolution in the SAMUS PDTs, and these drift tubes are therefore more closely spaced. As in the WAMUS, there are three stations of PDTs: A, B, C. But in this case, each station is made of three separate layers of tubes. These are cylinders 30mm in diameter. In order to combat the small packing fraction of cylinders, each layer is subdivided into two rows of drift tubes offset by half a tube diameter. Each layer has PDTs arranged in a different spatial orientation: one vertically, one horizontally, and one diagonally for multi-track correlation. Table 2.6 details some WAMAS and SAMUS parameters.

Chapter 3

Triggering and Data Acquisition

The crossing rate for the $p\bar{p}$ beams at the Tevatron is 290kHz. At a luminosity of $5 \times 10^{30} \text{cm}^{-2}\text{s}^{-1}$, about three in four of these crossings produces an interaction. The vast majority of these interactions are physically uninteresting, and the *trigger* system is designed to reject these events. The trigger system made of three levels, each of increasingly complex event characterization. A schematic of the overall DØ trigger system is shown in Figure 3.1

The Level 0 trigger signals an inelastic interaction, using scintillation counters. Level 1 consists of several hardware triggers, which can be modified with software. Most of these triggers operate within the $3.5\mu\text{s}$ beam crossing time, although some do require many beam crossings to complete their respective operations, and are collectively called the Level 1.5 triggers. Level 2 triggers consist of a set of algorithms residing in a farm of VAX 4000's, which reduce the data rate to about 2Hz, and is the last step in the trigger process.

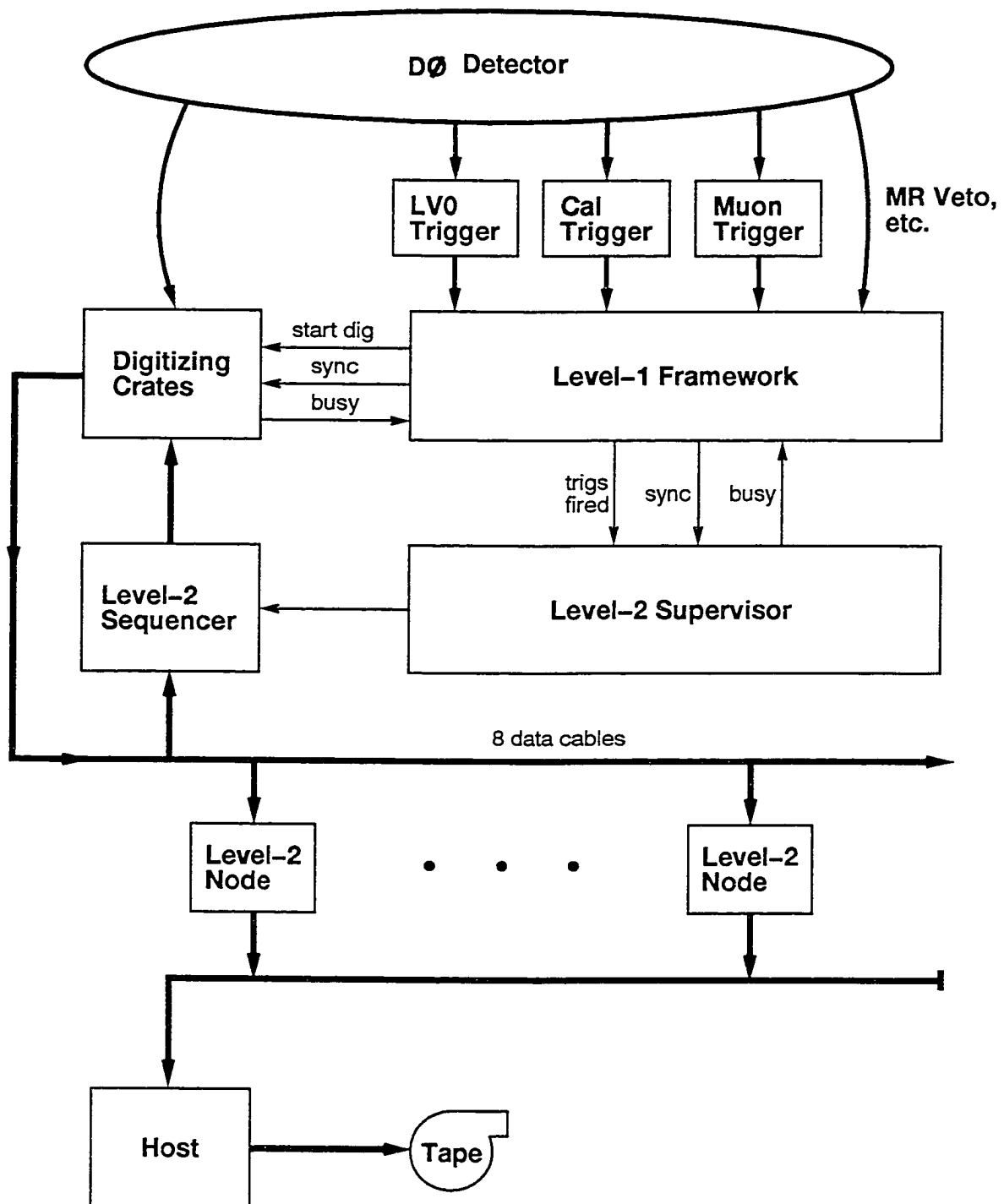


Figure 3.1: Schematic of the DØ trigger and data acquisition system.

3.1 Level 0

The Level 0 trigger consists of scintillation counters mounted on the front of the EC, and is used to detect non-diffractive, inelastic processes with an efficiency of $> 99\%$. Level 0 serves as the luminosity counter for the experiment. The hodoscope formed by the scintillators provides partial coverage in the range $1.9 < |\eta| < 4.3$, and nearly full coverage for the range $2.3 < |\eta| < 3.9$. The scintillators are in the form of bars, which are layered, two per hodoscope, and rotated by 90° . An inelastic collision inferred through a coincidence in the hodoscopes, and the signal arrival times from both detectors provides a measurement of the vertex position, accurate to $\pm 3.5\text{cm}$. Any trigger which depends on E_T would be in gross error without this vertex position, given the spread of 30cm in the interaction region. In the event of a multiple interaction, the vertex position is ambiguous. The Level 0 trigger reduces the data rate from the beam crossing rate of 290 kHz to a rate of approximately 17 kHz .

3.2 Level 1 framework

The level 1 framework [21][22][23] gathers information from each of the specific level 1 trigger devices, using the information to decide whether certain triggers, or the entire event, should be vetoed. If the event is to be kept, the Level 1 framework commands the readout of the digitization crates, and also provides an interface to level 2. The calorimeter trigger, and parts of the muon trigger are the only triggers which operate within the $3.5\mu\text{s}$ event crossing.

The primary input to the framework is a set of 256 trigger terms, each indicating whether some trigger requirement had been met. The 256 trigger terms are reduced by an and/or network, to 32 trigger bits, each corresponding to a specific trigger. Each trigger bit can have a programmable prescale, so that only every N events

will result in that bit being asserted. Digitizing hardware is located in 86 VME crates in the moving counting house, the crates being divided into 32 geographic sectors for readout purposes. The framework has a list of sectors which must be read out for each trigger bit. When the digitization of an event is complete, its information is passed to level 2. If a level 1.5 confirmation is required, digitization is initiated as usual, but notification of level 2 is delayed.

Interactions with the level 1 framework occur through the trigger control computer (TCC), a dedicated Vaxstation 4000/60. The TCC is responsible for programming the level 1 hardware at the beginning and ends of runs, as well as performing diagnostics and monitoring.

3.2.1 Level 1 Calorimeter Trigger

The level 1 calorimeter trigger [22][23] is located on the first floor of the moving counting house, and is responsible for making triggering decisions based purely on calorimeter information. For the purposes of triggering, the calorimeter cells are summed into tower sizes of 0.2×0.2 in η , ϕ , and cover out to $|\eta| = 4.0$. Separate trigger inputs provide for 1280 sections each of EM and FH information. The following quantities are calculated:

- The total EM energy
- The total hadronic energy
- The total EM E_T
- The total hadronic E_T
- The total E_T
- The total $\cancel{E_T}$

The transverse quantities are calculated with an assumed vertex position $z = 0$. The individual trigger tower E_T 's are digitized by 8 bit flash ADC's, and provide part of the address of lookup tables. An additional 3 bits are provided by the Level 0 z-vertex determination. These lookups provide EM and hadronic towers above some preset threshold, using a vertex corrected determination of E_T . Trigger thresholds can be specified in terms of some number of towers above some E_T , or more globally in terms of event E_T (or \cancel{E}_T).

3.2.2 Level 1 Muon triggers

The basic information provided to the framework by this level 1 trigger, is a single latch bit for each of the drift tubes in the samus and wamus. The trigger electronics are physically distinct for the five regions: CF, EF-North, SAMUS-North, EF-South, SAMUS-South. Level 1 provides coarse hit centroids, based on hits in the various layers. Where full coverage is available, the hits are formed on tracks traversing all three layers. If momentum information, and not just the presence of a muon, is required, the centroid information is sent to a level 1.5 trigger for confirmation, where finer p_T information is calculated.

3.3 Level 2

The level 2 trigger consists of a large farm of VAX 4000/60's and 4000/90's running the VaxELN real-time operating system. Each of these nodes runs software filters which require information from the entire event. The filters are built around a set of specific *trigger tools*, each tool being used for a specific type of particle, or event characteristic, such as muons, or \cancel{E}_T . The tools are associated in particular combinations into scripts; each script being associated with one of the 32 level 1 bits. Each script can spawn several level 2 filters, and for each script which passes

(ie, all tools in the script were satisfied) a bit is set in the 128 bit mask of *filter* bits. If any of the filter bits are set, the event advances to the host computers, where it can be written to tape for offline analysis. The interested reader should consult [24] for more details on the host computers and event streaming to tape.

Chapter 4

Defining objects offline

The triggering system provides information as quickly as possible, and as a result, the physics objects are not fully defined. Even in the case of unlimited time in Level 2, the fixed definition of a physics object would preclude the use of alternative, possibly better, definitions in an offline analysis. The process of turning the raw detector information into reconstructed physics objects is carried out by a program called DØRECO.

This analysis is concerned with the identification of tau leptons and jets, and the discussion will therefore be limited to those objects.

4.1 Jets from gluons and quarks

Confinement forbids the existence of individual quarks or gluons; only color singlet objects can appear in nature. When a non-zero color charge object is created from a hard scattering process or gluon radiation, the increasing potential between two separating colored objects provides the energy needed to create new quarks from the vacuum. The newly created quarks appear in ways which result in color singlet hadrons, in a process called hadronization. The deposition of energy in the

calorimeter by these hadrons is one kind of jet. The energy in the parent quark is now contained in the collection of hadrons in the calorimeter, and there are several methods available for reconstructing that energy. The algorithm used most often, and used here, for jet finding at DØ is the cone algorithm [27].

The cone algorithm proceeds in two steps:

1. Calorimeter towers ($\Delta\eta \times \Delta\phi = 0.1 \times 0.1$), are identified. The highest E_T towers are used as seeds, around which contiguous towers containing more than 1GeV are added, provided that the added towers are within 0.3 units in ϕ and η of the seed.
2. The direction (η, ϕ) of the jet is calculated using a fixed cone size, $R = \sqrt{\Delta\eta^2 + \Delta\phi^2}$.
3. Calculate the energy contained in the jet, and redetermine η, ϕ .
4. Iterate steps 2,3 until the jet position is stable.
5. If two jets are close enough so that more than 50% of the E_T of the softer jet is contained in the overlap region, the two are merged into one jet. Otherwise, there will be two distinct jets, and any shared cells will be assigned according to their proximity to the jet axes.
6. Retain jets whose $E_T > 8\text{GeV}$

The jet energy and direction are determined by:

$$\eta = \frac{\sum_i E_T^i \eta^i}{\sum_i E_T^i}, \quad \phi = \frac{\sum_i E_T^i \phi^i}{\sum_i E_T^i}, \quad E_T = \sum_i E_i \sin(\theta_i) \quad (4.1)$$

Upon the construction of spatially stable jets, the η, ϕ of each jet is recalculated using the definitions:

$$\phi = \tan^{-1} \left(\frac{\sum_i E_{y_i}}{\sum_i E_{x_i}} \right) \quad (4.2)$$

$$\theta = \tan^{-1} \left(\frac{\sqrt{\sum_i E_{x_i}^2 + \sum_i E_{y_i}^2}}{\sum_i E_{z_i}} \right) \quad (4.3)$$

where

$$E_{x_i} = E_i \sin \theta_i \cos \phi_i, \quad E_{y_i} = E_i \sin \theta_i \sin \phi_i, \quad E_{z_i} = E_i \cos \theta_i \quad (4.4)$$

A cone size of 0.7 gives the best energy reconstruction, but it is too large for busy events, like $t\bar{t}$, because one merges objects which should remain distinct. A cone size of 0.3 prevents unwanted merging, but the energy resolution is poor, because, as mentioned previously, jet sizes are expected to be about 0.5. This analysis uses 0.5 cone jets.

Once a jet has been identified offline, its energy must be corrected for a number of effects, broadly categorized as offset [28] and response [29], as well as out-of-cone showering. The relationship of the underlying particle energy to the measured energy is:

$$E_{jet}^{ptcl} = \frac{E_{jet}^{meas} - E_O(\mathcal{R}, \eta, \mathcal{L})}{R_{jet}(\mathcal{R}, \eta, \mathcal{L})S(\mathcal{R}, \eta, \mathcal{L})} \quad (4.5)$$

where E_O denotes the energy offset, and depends on the algorithm cone size, \mathcal{R} , the pseudo-rapidity, η , and the luminosity, \mathcal{L} . The jet response correction, (R_{jet}) , and correction for out-of-cone showering, (S) , are defined in the following sections.

4.1.1 Offset correction

When an event resulting from a hard scatter occurs, several effects conspire to offset the energy measured: underlying event, pile-up, Uranium noise, and multiple interactions.

The sum of all offset contributions can be measured using min-bias (MB) data, in which a non-diffractive event is required. The contribution due to pile-up, Uranium noise, and multiple interactions is measured using a zero-bias (ZB) trigger requiring only a beam crossing. If all events with hard scatters are vetoed in the

ZB sample, the underlying events energy density can modeled as:

$$D_{ue} = D_{MB} - D_{ZB}^{noHC} \quad (4.6)$$

which depends on both η and center-of-mass energy.

Uranium noise results from the radioactivity of the absorber plates. Calibration runs taken before data runs give the average and rms noise for the calorimeter, and only those cells which contain energy inconsistent with noise are read out during data runs. Noise in the calorimeter is only approximately gaussian, with zero mean, but non-zero mean outside a 2σ window. The result is that the Uranium noise contributes net positive energy to jets.

Pile-up is the consequence of long shaping times in the calorimeter electronics. The time required to collect all charge liberated in the LAr is longer than the $3.5 \mu s$ beam crossing time. As a result, if a cell is read out over two consecutive crossings, the second readout will include charge from the previous interaction. It would appear, then, that the effect of pile-up would be to increase the signal in a cell; however, the calorimeter is readout according to a baseline subtraction scheme, wherein the energy in each cell is read just before and after a beam crossing. It is the *difference* in readings which is read out. So, the monotonically decreasing pile-up charge has the effect of lowering the cell energy.

The probability of multiple interactions during each beam crossing is luminosity dependent, and can be measured independently of the other MB effects using multiple interaction tools [30].

4.1.2 Response: The Missing E_T Projection Fraction Method

Jet finding algorithms map the charge collected in the LAr to incident particle energy, and must rely on calibration data from the test beam (TB). However, TB data will not map directly to collider data for a number of reasons.

- Particles will not always strike the center of cells

- Particles are not always normally incident
- Calorimeter cryostat modules differ slightly in construction

The *in situ* electromagnetic response of the calorimeter can be measured using the $Z \rightarrow e^+e^-$, J/Ψ , and π^0 resonances ([31], pg 79). The hadronic response can then be measured by requiring that events containing one photon and one jet contain no E_T :

$$\vec{E}_{T\gamma} + \vec{E}_{Tjet} = 0 \quad (4.7)$$

In this case, $E_{T\gamma}$ is well known, and measured correctly. The poorly measured E_{Tjet} , however, will depend on the response of the calorimeter:

$$\begin{aligned} \vec{E}_{T\gamma} + R_{jet} \vec{E}_{Tjet} &= -\vec{E}_T \\ 1 + R_{jet} \frac{\hat{n}_{T\gamma} \cdot \vec{E}_{Tjet}}{E_{T\gamma}} &= -\frac{\hat{n}_{T\gamma} \cdot \vec{E}_T}{E_{T\gamma}} \end{aligned} \quad (4.8)$$

where:

$$\hat{n}_{T\gamma} = \frac{\vec{E}_{T\gamma}}{|\vec{E}_{T\gamma}|} \quad (4.9)$$

or:

$$\begin{aligned} R_{jet} &= 1 + \frac{\vec{E}_T \cdot \hat{n}_{T\gamma}}{E_{T\gamma}} \\ &= 1 + MPF \end{aligned} \quad (4.10)$$

This is a problematic definition of R_{jet} , because it is written in terms of E_T , whereas the response is actually dependent on E . Measuring R_{jet} in terms of E_{jet} is also problematic, and is measured instead in terms of a variable strongly correlated with E_{jet}^{ptcl} , the particle initiating the jet. This variable is the *energy estimator*, E' , defined as:

$$E' = E_{T\gamma} \cdot \cosh(\eta) \quad (4.11)$$

One can map $E' \rightarrow E_{jet}$ bin by bin without concern for energy dependent terms in the hadronic jet, like a changing value of e/π , and changing particle content.

4.1.3 Showering Correction

The showering correction compensates for energy flow through the boundary of the jet algorithm cone. Whether out-of-cone energy in data originates from an offset effect, or fragmentation outside of the cone at the particle level (physics out-of-cone) cannot be determined. Therefore, a combination of data and Herwig Monte Carlo is used to derive the showering correction.

First, the total out-of-cone ratio, F_{tot} is calculated for some algorithm jet in data. For 0.7 cone jets, $\eta < 0.4$, F_{tot} is:

$$F_{tot} = \frac{E_{jet}(r < 1.0)}{E_{jet}(r < 0.7)} \quad (4.12)$$

where E_{jet} has been corrected for offset effects. F_{tot} measures the contribution from physics out-of-cone, F_{phy} , as well as showering loss, F_{sho} . The former term can be calculated with the procedure outlined above, but using herwig instead of data.

The showering correction is defined as:

$$F_{sho} = \frac{E_{jet}(r < 0.7) + E_{sho}}{E_{jet}(r < 0.7)} \quad (4.13)$$

where E_{sho} is the energy associated with particles emitted inside the cone, but whose energy is deposited outside the cone. The fraction of energy lost due to showering is arrived at via:

$$\begin{aligned} F_{tot} &= \frac{E_{jet}(r < 0.7) + E_{phy}(r > 0.7) + E_{sho}}{E_{jet}(r < 0.7)} \\ F_{phy} &= \frac{E_{jet}(r < 0.7) + E_{phy}(r > 0.7)}{E_{jet}(r < 0.7)} \\ F_{sho} &= F_{tot} - F_{phy} + 1 \end{aligned} \quad (4.14)$$

The fraction of the shower which is retained is then $S = 1/F_{sho}$.

4.2 Identifying the origin of jets

All physics objects used in this analysis appear in the detector as a hadronic jet, although the source of these jets are often quite distinct. Other analyses [25] have made use of jet shape to distinguish between jets originating from gluons and those originating from quarks. The semi-leptonic decay of the B is used as a method of identifying (tagging) jets which originate from a b-quark. Most use the decay mode containing a muon [25][34][35], although studies have been done using the mode containing an electron [36][37]. This analysis makes no attempt to differentiate between any jets which have a quark or gluon as the source. The signal to background obtained without such distinction is acceptable, although the expected signal is marginal. Therefore, any further reduction of signal in an attempt to pick events with only certain types of jets (ie, to reject events with high gluon jet content) could reduce the signal to an unusable level.

An example of an event containing jets from $t\bar{t}W^+W^-b\bar{b} \rightarrow all\,jets$ candidate is shown in Figure 4.1. The plot shows seven jets, where a significant amount of the energy is deposited in the hadronic section of the calorimeter. There are two jets which are identified as b-jets by the presence of muons near the jet axis. In this type of decay, very little missing transverse energy is expected, and this is consistent with the tiny amount shown in the plot (labeled as Miss_ET).

4.2.1 Jets from Tau decay

A tau lepton decays before reaching any detector element, and it must be identified by its decay products. Two of its decay modes are leptonic, and produce low E_T leptons with \bar{E}_T , as would be expected from $W \rightarrow lepton$ decay. There is nothing which identifies this final state as having come from a τ , and it will simply amount to lost events. The third class of decays, hadronic, makes up 64% of the total rate. 99% of this mode contains one or three charged particles, and the resulting

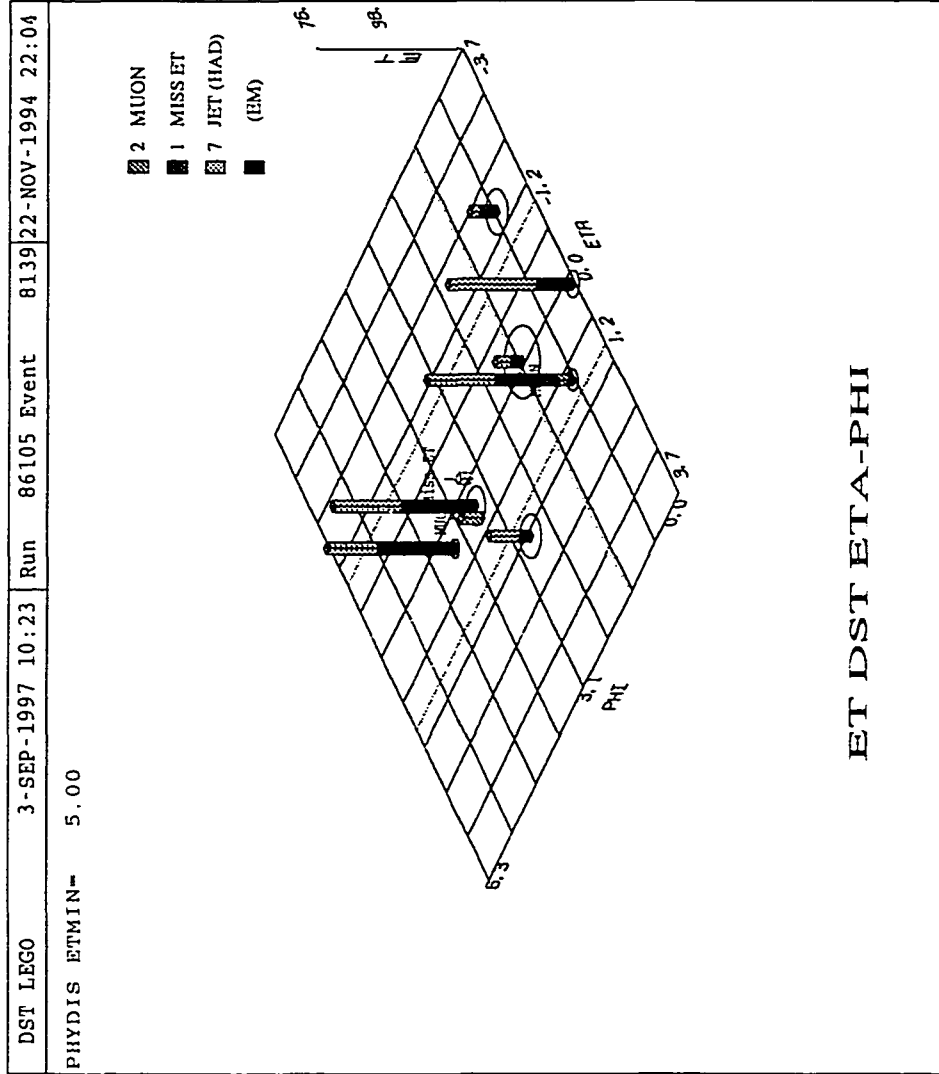


Figure 4.1: Sample event display, showing a $t\bar{t} \rightarrow W^+W^-b\bar{b} \rightarrow alljets$ candidate, in the η, ϕ coordinate system.

jet is very narrow compared to quark or gluon jets. Use of the charged track multiplicity has been used successfully by others [10], but the DØ tracking requires looser constraints. The strength of the DØ detector is its calorimeter, and its τ -id is based almost entirely on the jet shape. The details of τ -id are covered in section 6.2, and the contamination due to QCD jets (those arising from a quark or gluon) faking a τ -jet is covered in section 6.3.

Chapter 5

Data Selection

As discussed in Section 1.5.1, this analysis is concerned with two final states: one containing five jets, and the other containing four. If a trigger had existed that required only four jets, it would have sufficed for both final states. In fact, such a trigger was available, but it was not used for the entire Run Ib, and a prescale was introduced in the latter part of the run. Consequently, to maximize statistical accuracy, we chose the JET_MULTI filter for our $5jet + \cancel{E}_T$ search, and the JET_MS_MULTI filter for the case of $4jet + \cancel{E}_T$. Table 5.1 lists the Level 1 and Level 2 requirements for these triggers. Additional requirements on the data were:

- The MRBS_LOSS signal was used to veto events that occur simultaneously with the injection of proton beam into the Main Ring [14]. Losses from the Main Ring produce sprays of particles in the detector, that lead to poor measurement jets of \cancel{E}_T .
- The MICRO_BLANK signal was used to veto events that occurred simultaneously with the passing of proton bunches through the detector [15].

JET_MULTI		
Level 1	Level 2	Beginning Run
$3LJ > 15\text{GeV}$	$5JT > 10\text{GeV}$ 0.3 cone, $ \eta_{det} < 2.5$	70000
$3LJ > 15\text{GeV}$ $1LJ > 6\text{GeV}$ $1JT > 3\text{GeV}$	$5JT > 10\text{GeV}$ 0.3 cone, $ \eta_{det} < 2.5$	77825
$3LJ > 15\text{GeV}, \eta_{det} < 2.4$ $3JT > 7\text{GeV}, \eta_{det} < 2.6$ $1JT > 3\text{GeV}$	$5JT > 10\text{GeV}$ 0.3 cone, $ \eta_{det} < 2.5$ $HT > 115, \eta_{det} < 2.0$	85277
$3LJ > 15\text{GeV}, \eta_{det} < 2.4$ $3JT > 7\text{GeV}, \eta_{det} < 2.6$ $1JT > 3\text{GeV}$	$5JT > 10\text{GeV}$ 0.3 cone, $ \eta_{det} < 2.5$ $HT > 100, \eta_{det} < 2.0$	89892
JET_MS_MULTI		
Level 1	Level 2	Beginning Run
JET_MULTI	$4JT > 12\text{GeV}$ 0.3 cone, $ \eta_{det} < 2.5, E_T > 10\text{GeV}$	81578
JET_MULTI	$4JT > 12\text{GeV}$ 0.3 cone, $ \eta_{det} < 2.5, E_T > 14\text{GeV}$	85277
JET_MULTI	Prescale (1,1,1,2) $4JT > 12\text{GeV}$ 0.3 cone, $ \eta_{det} < 2.5, E_T > 14\text{GeV}$	89892

Table 5.1: Requirements for the JET_MULTI trigger, and the JET_MULTI and JET_MS_MULTI filters for Run Ib.

- “Unphysical Events” which had more than 4 TeV of energy deposited in the calorimeter were rejected ([33], pg 67).
- Events in which the CH fraction of any jet’s energy in the calorimeter was greater than 70% of the total deposited energy were rejected. Such events were attributed to spray from the Main Ring, or to electronic noise in the calorimeter, or to fluctuations from uranium radioactive emission [33].
- All suspicious runs, identified as problematic due to electronics failure, etc, were rejected.

The requirement of the additional cuts above reduces the available integrated luminosity in the two filters to:

- JET_MULTI : 71.8 pb^{-1}

- JET_MS_MULTI : 62.2 pb⁻¹

Chapter 6

Analysis

This chapter outlines the steps involved in separating a few hundred top quark pair decays from a sea of almost a million background events. Characteristics of the signal of interest and the background from $W + jets$ events were determined using Monte Carlo simulations. The production of $W + jets$ was modeled by VECBOS, while the hadronization of $W + jets$ top quark decays are modeled by Isajet. Event selection proceeds along the following course:

1. **Initial Selection.** Most events in the JET_MULTI and JET_MS_MULTI filters result from QCD $2 \rightarrow 2$ processes, with additional jets being caused by initial or final state radiation. The result is an event with low E_T , and few jets, but each with appreciable energy. A set of minimal criteria is applied to the Monte Carlo and to data, removing events that are not likely to have resulted from the $t\bar{t}$ signal.
2. **Neural Network.** After the application of the initial criteria, the remaining events correspond to a mixture of signal and background, of nearly identical topology, but with subtle differences. A set of variables are chosen that best describe those differences, and a neural network is used to place restric-

tions on these variables in a way that takes their correlations into account. Changing the mass of the H^+ changes the event characteristics, and separate networks are therefore used for each mass hypothesized. For example, as the mass of the H^+ increases, the energy of the recoiling b-jet becomes smaller and the energy of the ν_τ increases, resulting in softer b-jets and higher E_T .

3. **Final Selection.** After passing some cutoff in the neural network, the data contain events that are almost identical in character to what is expected from the $t\bar{t}$ signal. The final sample is obtained by requiring that events contain at least one good τ candidate, of specified energy and pseudo-rapidity, as defined in Section 6.2.

6.1 Event Selection

Initial Selection Criteria

Events selected from the JET_MS_MULTI trigger were required to pass the following selection criteria:

- $\cancel{E}_T > 25\text{GeV}$
- 4 jets, each with $E_T > 20\text{GeV}$
- physics $|\eta_j| < 2.0$
- Maximum jet $E_T < 150\text{GeV}$
- number of jets < 8 , for jets with $E_T > 8\text{GeV}$

while events selected from the JET_MULTI trigger were required to pass

- $\cancel{E}_T > 25\text{GeV}$
- 5 jets, each with $E_T > 15\text{GeV}$
- physics $|\eta_j| < 2.0$
- Maximum jet $E_T < 150\text{GeV}$
- number of jets < 8 , for jets with $E_T > 8\text{GeV}$

The choice of the \cancel{E}_T cutoff was based on a preliminary study using Neural Networks. Figure 6.1 shows the effect on the \cancel{E}_T distribution for $t\bar{t} \rightarrow W^+W^-b\bar{b}$ events of setting the output for distinguishing signal from all JET_MULTI events at $\text{NN} = 0.8$. No values of \cancel{E}_T below about 30 GeV pass the NN cutoff, and 25 GeV is therefore a cutoff that does not affect signal, but eliminates a large fraction of the background.

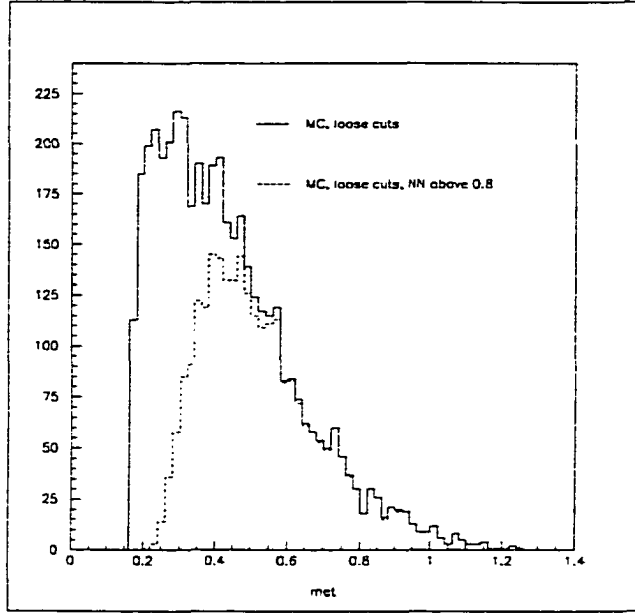


Figure 6.1: Missing energy in the $t\bar{t} \rightarrow WWbb$ Monte Carlo. The E_T has been scaled by 1/150, so that a value of 0.2 corresponds to $E_T = 30\text{GeV}$

The cutoffs on jet energy and jet multiplicity were chosen to maximize acceptance of signal, given the trigger requirements. Section 8 describes the dependence of the expected trigger efficiency on the E_T of the fourth (or fifth) jet. The results indicate that a lower E_T cutoff would not have much impact on signal efficiency.

The final cut was imposed to avoid a low statistics problem in the determination of the QCD τ fake rate for events with high jet multiplicities.

6.1.1 Cutoffs on output from the Neural Network

After the imposition of the initial selection criteria, the data was passed in parallel through a series of neural networks, each network having been optimized on a different signal. The variables used in the training of the network were similar to those used in the $t\bar{t} \rightarrow alljets$ analysis [25]. Six variables were used in a network with six input nodes, thirteen hidden nodes, and one output node. This defines a network with 91 degrees of freedom, which, as indicated in table 7.1, is sufficiently over-constrained, if one uses the loose rule that the number of training events (events passing the initial selection criteria) should exceed the number of degrees of freedom by a factor of ten. The variables used in the network are:

- E_T , the missing energy in the event. Very important in reducing the QCD background, which contains no real source of missing energy.
- Q_1, Q_2 The momentum flow of an event can be characterized by the momentum tensor M_{ab} ([26], pg 280)

$$M_{ab} = \frac{\sum_j^{N_{jets}} p_{ja} p_{jb}}{\sum_j p_j^2} \quad (6.1)$$

having eigenvalues Q_1, Q_2, Q_3 . Only two of these are independent, and we choose to use only the first two in the analysis. These eigenvalues are traditionally termed Aplanarity ($\frac{3}{2}Q_1$), and Sphericity ($\frac{3}{2}(Q_1 + Q_2)$). Because using Aplanarity and Sphericity did not improve the performance of the network relative to Q_1 and Q_2 , the latter were used in the network.

Figures 6.2 - 6.4 show examples of the separation between events in the JET_MULTI trigger, and Monte Carlo of $t\bar{t} \rightarrow W^+W^-b\bar{b} \rightarrow \tau jj$, where both have passed the initial criteria for the $5jet + E_T$ topology.

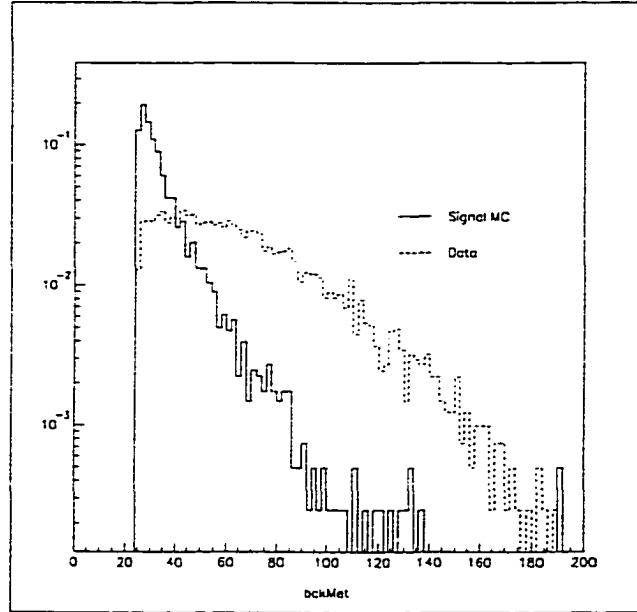


Figure 6.2: Event E_T

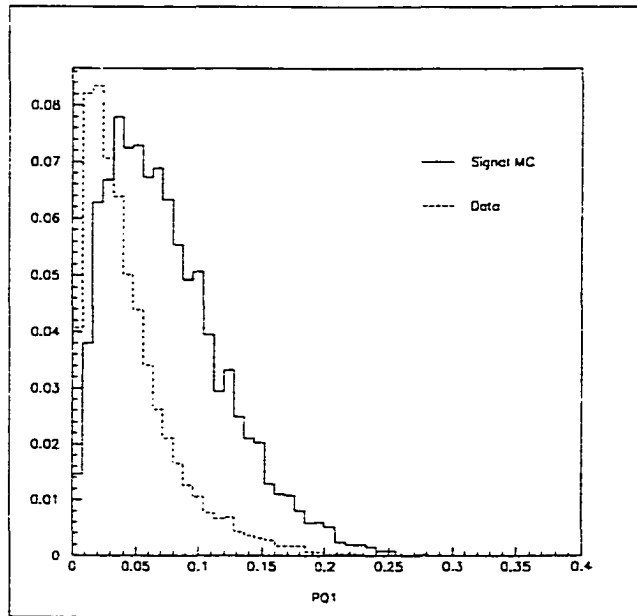


Figure 6.3: First eigenvalue of the momentum tensor

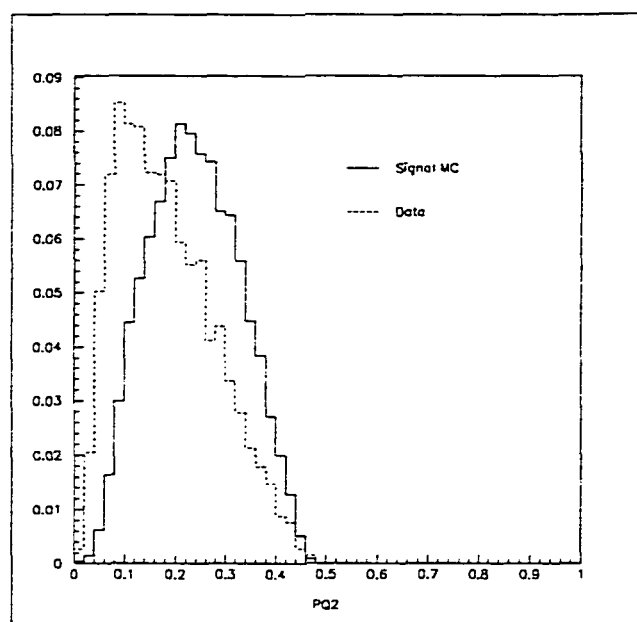


Figure 6.4: Second eigenvalue of the momentum tensor

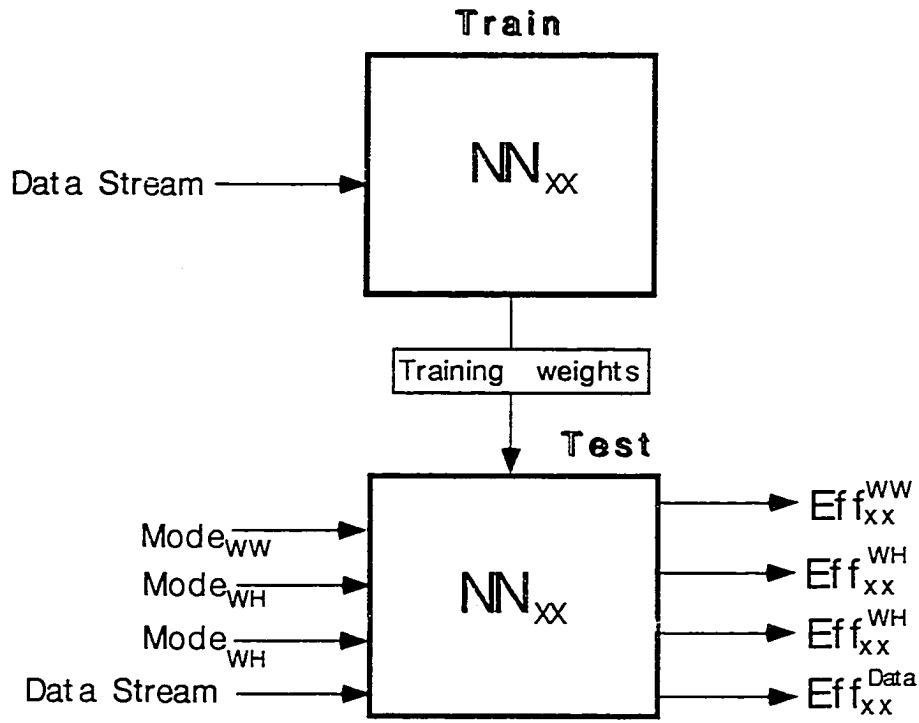


Figure 6.5: Scheme for the training of neural nets, and the determination of all signal efficiencies.

To maximize acceptance for signal, the neural nets used in this analysis are trained on only one decay mode, and one H^+ mass. We denote a network trained to accept $t\bar{t} \rightarrow W^+W^-b\bar{b}$ decays as NN_{WW} . Figure 6.5 indicates the training and testing procedures, where “Mode_{XX}” indicates a particular decay mode, and “Data Stream” is either JET_MULTI or JET_MS_MULTI, and is treated as background. Figure 6.6 shows the remarkable separation achieved using our three variables.

When the trained neural network is used to select a portion of the data stream, it selects from a combination of QCD, W+jets, and $t\bar{t} \rightarrow XXb\bar{b}$ events. The efficiency of the NN_{XX} network for all possible $t\bar{t} \rightarrow XX$ decays must therefore be known. The efficiencies are determined by applying the appropriate initial criteria to the signal. That is, if one finds the efficiency of the NN_{HH} network for the $t\bar{t} \rightarrow WW$ decay mode, the $t\bar{t} \rightarrow WW$ sample is required to pass the 4jets+ \cancel{E}_T selection criteria. Let Eff_{YY}^{XX} denote the efficiency for detecting Mode_{XX} in the network NN_{YY} . The prescription for determining Eff_{WH}^{HH} is then:

1. Train a network to discriminate between events in the JET_MULTI data stream from events in a $t\bar{t} \rightarrow WH$ Monte Carlo.
2. Save the weights from training
3. Apply the 5jet+ \cancel{E}_T cuts to events from a $t\bar{t} \rightarrow HH$ Monte Carlo. Let the number of events passing the cuts be n_L .
4. Initialize a NN with the weights from (2), and process events from (3). Let the number of events passing a NN cut of c be n_c .
5. $Eff_{WH}^{HH} \equiv \frac{n_c}{n_L}$

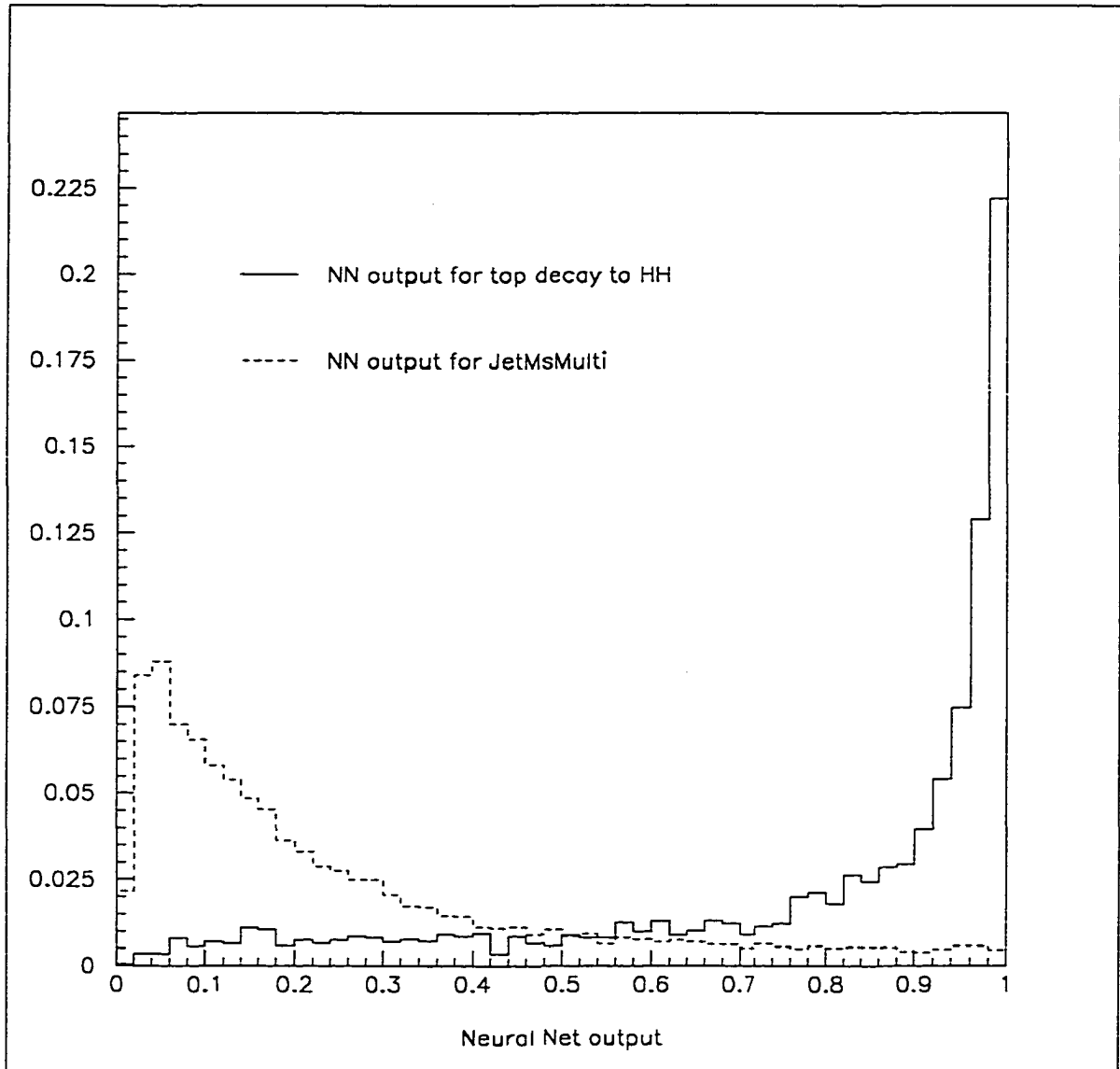


Figure 6.6: Separation in the output of a neural network trained on $t\bar{t} \rightarrow H^-H^+$ where both Higgs decay to τ . One test signal is data, and the other is MC of $t\bar{t} \rightarrow HH$. Ordinate is number of events, normalized to one.

6.2 Final selection: τ -id

Although the neural networks cut or keep events based on jet information, which includes information about hadronic τ decays, no special treatment is given to events which contain τ s. The final selection of events is the requirement that an event contain at least one τ .

The current τ -id used by DØ uses an *H-matrix* to describe correlations between variables which are thought to best describe τ decays.

Consider some set of variables, $\{y\}$, and the set of their residuals, $\{x\}$:

$$x_i = y_i - \langle y_i \rangle, \quad x_j = y_j - \langle y_j \rangle \quad (6.2)$$

with variance:

$$\sigma_{ij}^2 = \frac{1}{N} \sum_{n=0}^N (x_i^n - \langle x_i \rangle)(x_j^n - \langle x_j \rangle) \quad (6.3)$$

The H-matrix for this set of variables is defined as:

$$H_{ij} = (\sigma_{ij}^2)^{-1} \quad (6.4)$$

A chi-square can then be written:

$$\chi^2 = x_i H_{ij} x_j \quad (6.5)$$

The H-matrix for the current DØ τ -id [38] uses the following ten variables:

1. EM layer 1 energy / total energy
2. EM layer 2 energy / total energy
3. EM layer 3 energy / total energy
4. EM layer 4 energy / total energy
5. Fine hadronic energy / total energy
6. Log(total energy)

7. Z-vertex / vertex resolution
8. Energy in 3 x 3 tower / total energy
9. Energy in 5 x 5 tower / total energy
10. Profile

An H-matrix built from a set of signal events, and one built from background events are used to determine whether a particular event is more like signal or background in nature through the Fischer variable, F , or discriminant:

$$F = \chi_{bgnd}^2 - \chi_{signal}^2 \quad (6.6)$$

The signal H-matrix is a set of 736 $W \rightarrow \tau \nu_{\tau}$ events, which has an estimate for the noise from uranium and electronics added to it. The background H-matrix is built from the leading jet of a set of 400 data events which pass a filter requirement of 1 jet with $E_T \geq 20$ GeV.

If an object passes a set of loose cuts, it is stored in the PTAU ZEBRA bank [39][40], where stiffer cuts can be imposed (ZEBRA is a dynamic memory allocation scheme for FORTRAN). Identification of τ jets begins with a 0.7 cone jet, where the following requirements are imposed [41]:

- PTAU requirements

- $\text{RMS} = \sqrt{\Delta\eta^2 + \Delta\phi^2} \leq 0.25$
- Fraction of the jet contained in the electromagnetic portion of the calorimeter, $\text{EMF} < 0.95$

This cut removes electrons and noisy events.

- Charged track multiplicity

Hadronic decays of τ s have either one or three charged tracks. However, due to the resolution of the RunI central tracker, the cut used for τ -id is $1 \leq \text{charged tracks} \leq 7$ reconstructed within a 0.2×0.2 road in $\eta - \phi$.

- $|\eta_{physics}| < 2.5$

- τ -id requirements

- $Profile > 0.55$

$$Profile = \frac{E_{T1} + E_{T2}}{E_T} \quad (6.7)$$

τ jets are very narrow, and have a large fraction of their energy deposited in the two leading jet towers.

- $F > 0$

The profile is an important part of the τ characteristic, as can be seen in figure 6.9, which shows the correlation of the profile with the discriminant. It is clear that an event may be more consistent with signal than background, even with low profile values. It is therefore tempting to allow the H-matrix to decide on the best profile cut; however, adequate background rejection is only achieved when $F > 0$ and $Profile > 0.55$ are simultaneously required.

As discussed in the next section, the data-based monte carlo provides a reliable measure of τ -id efficiency, and in order to believe the results used in this analysis, we restrict the region of τ -id to match that used in the data-based monte carlo. Also, as discussed in section 6.3, using τ s with very high energy invites a large number of QCD fakes, and we therefore choose to limit the energy to a range favoring $t\bar{t} \rightarrow \tau + jets$, decays, as shown in figure 6.7. The final constraints on the τ are then:

- $|\eta_\tau| < 0.9$
- $10GeV < E_{Tj} < 60GeV$, where E_{Tj} is the E_T of a 0.5 cone jet found within $\Delta R < 0.2$ of the τ jet.

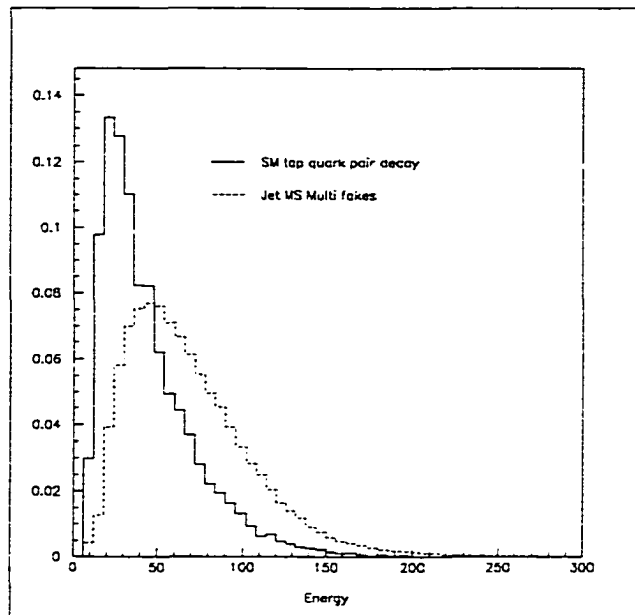


Figure 6.7: Energy for τ decays in SM decays of top quark pairs, and fakes found in JET_MULTI, where the energy is for 0.5 cone jets matched to τ jets, and the matched jets have $|\eta| < 0.9$.

6.2.1 τ -id efficiency

The efficiency for detecting a τ varies slightly depending upon the event topology: the efficiency found for $W \rightarrow \tau\nu$ with no additional jets will be different than that found for $t\bar{t} \rightarrow \tau + X$ events. As the SM decay mode with the highest $\sigma \times BR$, the efficiency for detecting τ s in the $t\bar{t} \rightarrow WWb\bar{b} \rightarrow 4jet + \tau; \tau \rightarrow jet$ is presented.

Let E_T denote the transverse energy distribution for all 0.5 cone jets with $|\eta| < 0.9$, and $10GeV < E_{Tjet} < 60GeV$, where the jet has been matched with an Isajet particle-level τ ($\Delta R_{\tau jet} < 0.2$).

and E_T^τ denote the transverse energy distribution for all jets tagged as τ s, where the jet is again matched to an Isajet particle-level τ . (Definitions of η and η^τ follow.) In order to avoid clutter, all η referring to tau jets should be taken to mean $|\eta|$.

The efficiency, ε of detecting any hadronically decaying τ , provided that its transverse energy and pseudo-rapidity are appropriate for tagging as a τ jet, is:

$$\varepsilon_{E_T} = \frac{E_T^\tau}{E_T} \quad (6.8)$$

$$\varepsilon_\eta = \frac{\eta^\tau}{\eta} \quad (6.9)$$

Figure 6.8 shows the τ -id efficiency as a function of jet transverse energy and pseudo-rapidity. Values of efficiency range from around 25% for a low E_T τ to almost 50% for a high E_T τ . The average E_T of all τ jets in the decay shown is 37 GeV, which corresponds to an efficiency of 45%, according to above definition.

6.2.2 Correction for Data-Based Monte Carlo

The essence of the τ -id is a very narrow jet which is well isolated. For this reason, the underlying event structure effects the efficiency in ways not well modeled by monte carlo. A data-based monte carlo (DBMC) was developed as a way of using the underlying event from data in conjunction with a monte carlo τ , as a way of

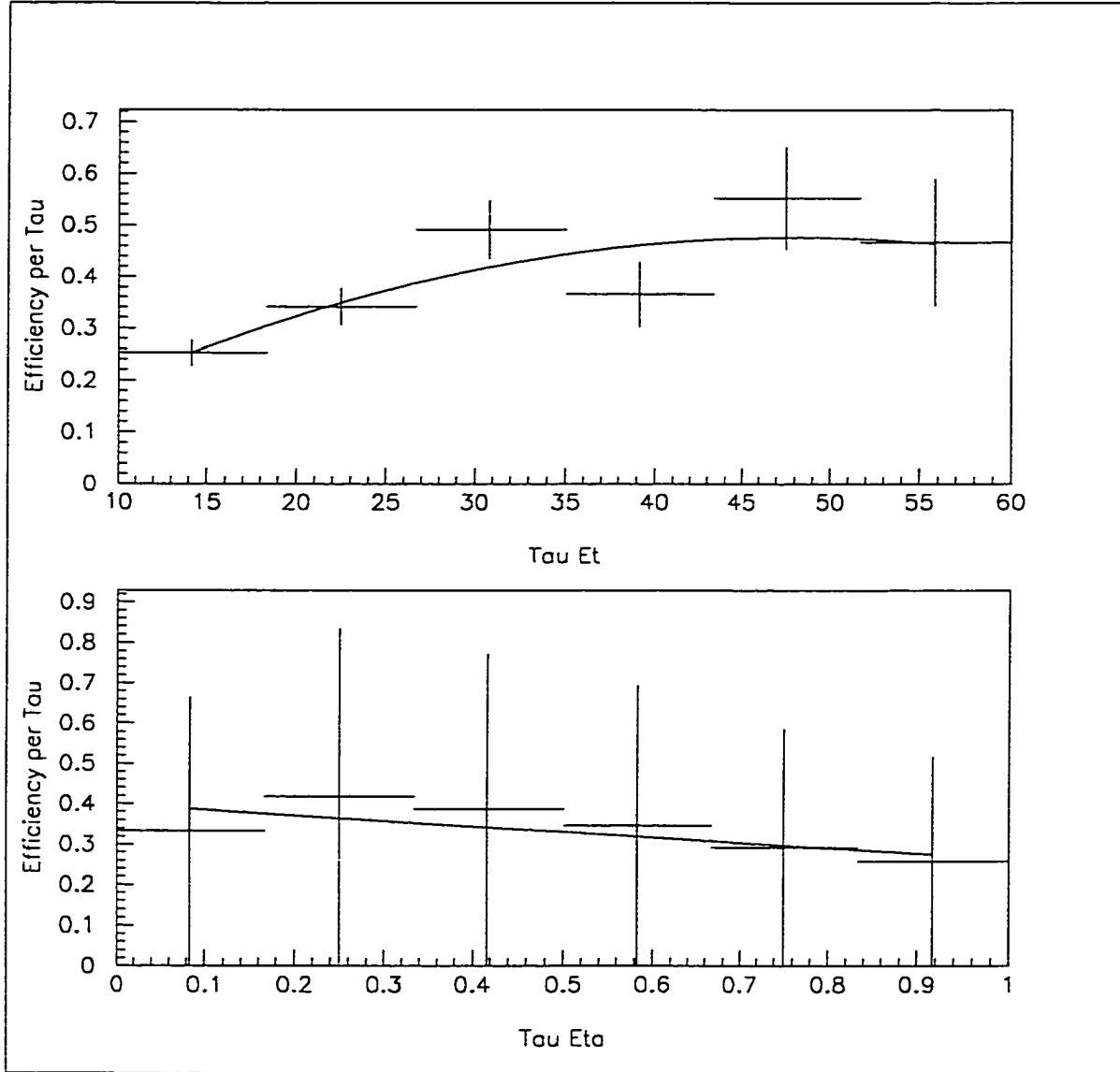


Figure 6.8: τ -id efficiency for all events in the decay of $t\bar{t} \rightarrow W^+W^-b\bar{b}$; $W^+ \rightarrow 2jets$; $W^- \rightarrow \tau$ where only hadronic τ decays are considered.

realistically modeling $W \rightarrow \tau$ events [42]. The result should be a lower efficiency for detecting τ s than one would achieve with MC alone.

DBMC involves replacing the electron in an event from data with a MC τ . This technique cannot be used in $t\bar{t}$ events, because of the small number of $t\bar{t} \rightarrow e + jets$ in the runIb data. The reduction in efficiency must therefore be calculated for a MC $W \rightarrow \tau$ sample. It is expected that the most dramatic decrease in efficiency will occur for events containing a tau with no additional jets. We therefore use

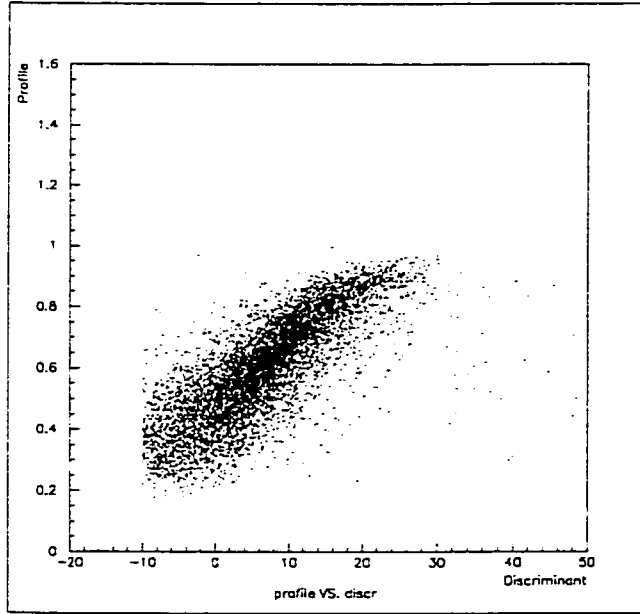


Figure 6.9: Correlation of Profile and Discriminant for a sample of $t\bar{t} \rightarrow WW \rightarrow \tau jj$ events.

$W+0$ jet events from DBMC and isajet to estimate the correction. The selection cuts on the $W \rightarrow e$ sample are:

- $E_T > 25\text{GeV}$
- $E_T^e > 25\text{GeV}$
- $|\eta_{detector}^e| < 0.9$

The selection cuts on the isajet tau (not the decay products) are therfor

6.3 Backgrounds

The dominant background in both final states is that from fakes, where QCD multijet events occur with a jet fluctuating, and causing \cancel{E}_T , while another fakes a τ . Because the τ is identified by its subsequent jet shape which is very narrow, a QCD jet which is also very narrow has a higher probability of faking a τ than the more typical broad QCD jet. Such jets occur for high energy gluons or quarks [32], and as a result, the tau fake rate is a function of jet energy. The probability that any particular jet is well isolated will also affect its ability to fake a τ , and for that reason, the jet multiplicity and pseudo-rapidity must also be considered.

The sample used to derive the fake rate was the data itself. The fake rate for all JET_MULTI, or JET_MS_MULTI events is dependent on the event \cancel{E}_T , and that dependence is covered in section 6.3.2.

The cuts used to select the fake rate sample are:

- JET_MULTI
 - $\cancel{E}_T > 20\text{GeV}$
 - $5 \leq n_{jets} \leq 7$
 - $E_{Tjet} < 150\text{GeV}$
- JET_MS_MULTI
 - $\cancel{E}_T > 20\text{GeV}$
 - $4 \leq n_{jets} \leq 7$
 - $E_{Tjet} < 150\text{GeV}$

The major sources of real τ leptons in these samples are $W + 3/4jet$, $W \rightarrow \tau \rightarrow jet$. The $W + 3jet$ sample has a 16.1% pass rate for the JET_MS_MULTI fake rate cuts. This is a 33pb process, and we analyze 62.2pb^{-1} of JET_MS_MULTI data, so that 360 events from $W + 3jet$, $W \rightarrow \tau \rightarrow jet$ are expected, while 79400 events

	DBMC	Isajet
jets	4539	2950
PTAU	3366	2152
τ	2487	1665
Efficiency	$55 \pm 1.4\%$	$56 \pm 1.7\%$

Table 6.1: Efficiency of cuts defining a τ for DBMC and Isajet.

- $E_T > 25\text{GeV}$
- $E_T^\tau > 25\text{GeV}$
- $|\eta^\tau| < 0.9$

Next, a subset of each sample was selected, containing one jet in the region $|\eta^{jet}| < 0.9$. One PTAU bank was then required, and that PTAU was then required to pass the profile cut. The results are shown in table 6.1. The difference in efficiencies is not statistically significant, and will therefore be ignored for this analysis.

from JET_MS_MULTI are observed. In the JET_MULTI sample, 21004 events are observed, while 112 are expected from $W + 4jets$; so, to better than 1%, these sources of taus can be ignored in the fake rate calculation.

6.3.1 Calculation of QCD fake rate

Let E^j denote the transverse energy distribution for all 0.5 cone jets with $|\eta| < 0.9$, and $10\text{GeV} < E_{Tjet} < 60\text{GeV}$, in events containing j jets, and E_τ^j denote the transverse energy distribution for all jets tagged as τ s in j jet events. (Definitions of η^j and η_τ^j follow.) In order to avoid clutter, all η referring to tau jets (fake or real) should be taken to mean $|\eta|$. Ignoring the small physics contribution, the probability that a jet of transverse energy E_T or pseudo-rapidity η appearing in an event with j jets will fake a tau is:

$$P_E^j(E_T) = \frac{E_\tau^j}{E^j}, \quad P_\eta^j(\eta) = \frac{\eta_\tau^j}{\eta^j} \quad (6.10)$$

The joint probability for a jet faking a τ is:

$$P^j(\eta, E_T) = P^j(\eta|E_T)P_E^j(E_T) \quad (6.11)$$

where

$$\int_0^{0.9} P^j(\eta|E_T) d\eta = 1 \quad (6.12)$$

Because E_T and η are uncorrelated,

$$P^j(\eta|E_T) = \frac{1}{N} P_\eta^j(\eta), \quad \int_0^{0.9} P_\eta^j(\eta) d\eta = N \quad (6.13)$$

Figure 6.10 shows the fake rates P_E^j, P_η^j for events combined from the JET_MULTI and JET_MS_MULTI filters. The errors are taken from the fitted parameters, and any one curve is no different than the next within those errors; however, the monotonically decreasing fake rate for higher multiplicity events does indicate some dependence, and the events passing the neural network are therefore separated according to multiplicity before the number of expected fakes are calculated.

The total number of QCD events expected to produce a τ is calculated based on jet E_T and η distributions of events which pass the neural network. The procedure is:

1. For a j-jet event, histogram E_T and $|\eta|$ of all 0.5 cone jets with $|\eta| < 0.9$, $10\text{GeV} < E_T < 60\text{GeV}$.
2. Find the average probability ($< P^j(\eta, E_T) >$)for a jet to fake a τ

$$< P^j(\eta, E_T) > = < P_E^j(E_T) > < P_\eta^j(\eta|E_T) > \quad (6.14)$$

$$< P_E^j(E_T) > = \frac{\sum_i P_E^j(E_T) E_{Ti}^j}{\sum_i E_{Ti}^j} \quad (6.15)$$

$$< P_\eta^j(\eta|E_T) > = \frac{\sum_i P_\eta^j(\eta) \eta_i^j}{N \sum_i \eta_i^j} \quad (6.16)$$

where E_{Ti}^j is the number of events in the i th bin.

3. The total number of fakes , N_f , is found by

$$N_f = \sum_{j=4}^8 < P^j(\eta, E_T) > A^j, \quad A^j = \sum_i \eta_i^j = \sum_i E_{Ti}^j \quad (6.17)$$

Using this technique, the number of QCD events expected to pass the final selection cut can be calculated as a function of NN cut.

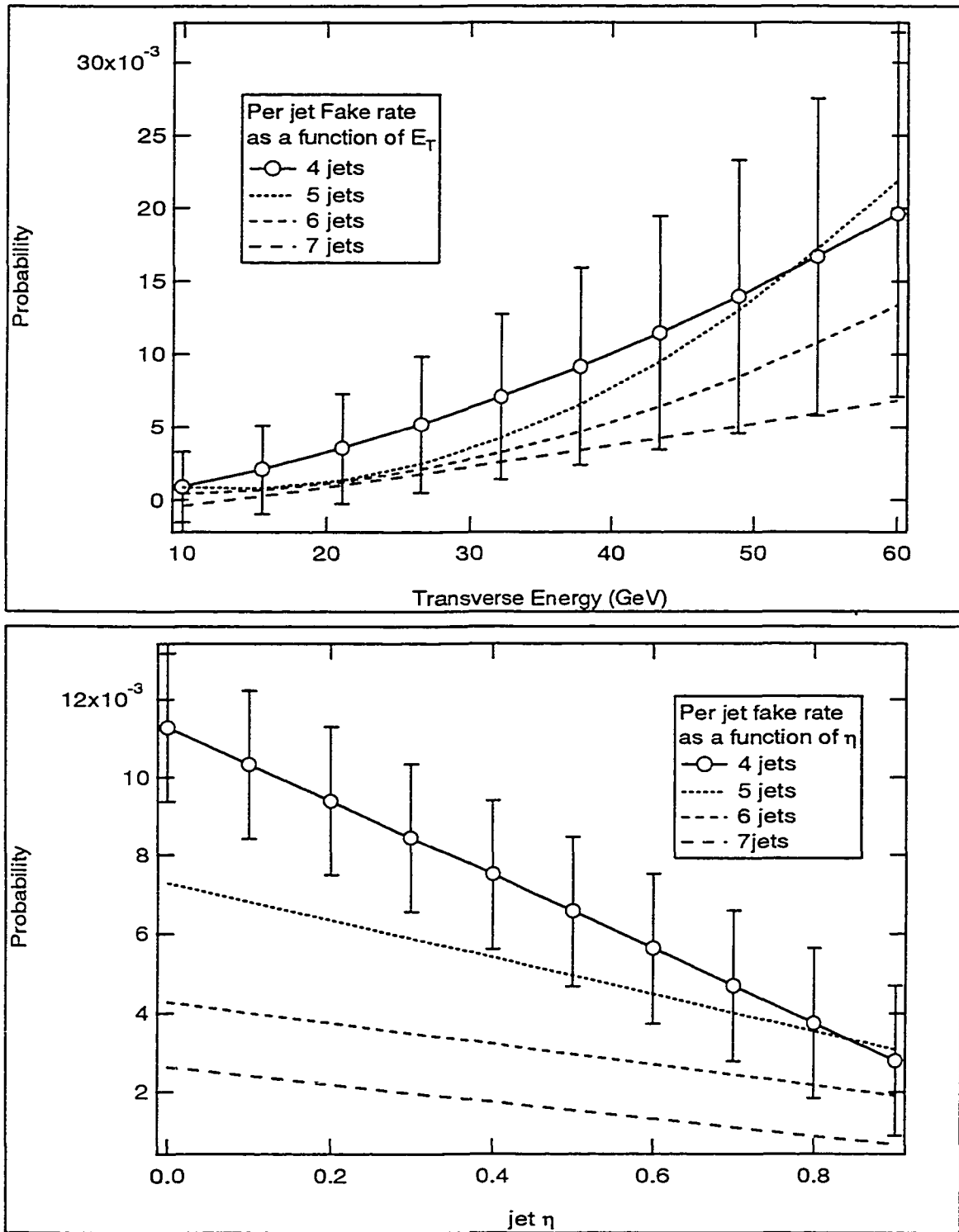


Figure 6.10: Fake rates for a combined sample of JET_MULTI, and JET_MS_MULTI.

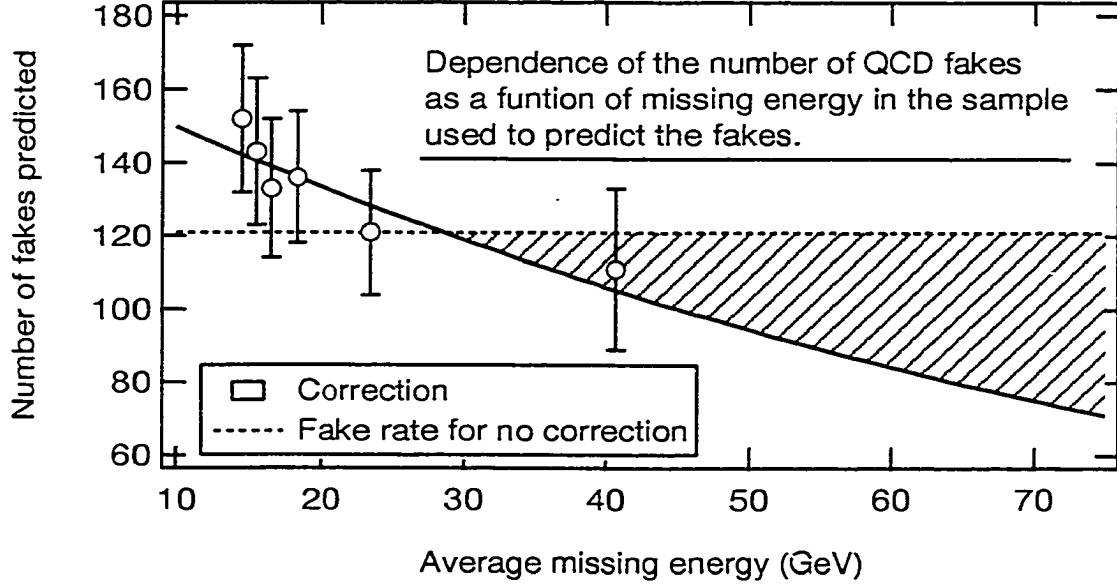


Figure 6.11: Predicted number of qcd fakes as a function of missing energy.

6.3.2 Effect of \cancel{E}_T on the QCD fake rate

The qcd fake rate is calculated with data which has a cut of $\cancel{E}_T > 20\text{GeV}$, which represents $\langle \cancel{E}_T \rangle = 28.17\text{GeV}$. If the \cancel{E}_T cut is changed, the number of predicted fakes also changes. The final event set selected by the neural network is comprised of events with $\langle \cancel{E}_T \rangle \approx 70\text{GeV}$, which is statistically inaccessible to the calculation of the fake rate. In order to estimate the correction, we use predictions of the fake rate for values of missing energy ranging from $14.5 \leq \langle \cancel{E}_T \rangle \leq 40.7\text{GeV}$, and extrapolate the correction to the data selected by the neural network.

To find the correction, we calculate the fake rate for various missing energy cuts, and then predict the number of fakes, n_f , which will be found in the JET_MS_MULTI loose cut sample, with a NN cut of 0.0. Figure 6.11 shows a fit to the measured n_f .

The sample used to calculate the fake rate becomes statistically limited, and we cannot go further in \cancel{E}_T . We fit the predicted fakes with an exponential of the

form:

$$n_f = e^{a+b\langle E_T \rangle} \quad (6.18)$$

and find values:

$$a = 5.12 \pm 0.177$$

$$b = -0.0115 \pm 0.0085$$

Let n_f calculated at $\langle E_T \rangle = 28.17$ be denoted n_{f_o} . The fraction by which we overestimate the fake rate, ξ is then

$$\xi = \frac{n_{f_o}}{n_f} \quad (6.19)$$

where n_f is predicted with the fit, equation 6.18. We now predict the number of fakes for any arbitrary NN cut, \bar{n}_{f_o} , and correct this number to arrive at the best estimate of the number of fakes expected, \bar{n}_f as:

$$\bar{n}_f = \bar{n}_{f_o} \xi \quad (6.20)$$

and

$$(\delta \bar{n}_f)^2 = ((\delta \bar{n}_f) \xi)^2 + (\bar{n}_{f_o} (\delta \xi))^2 \quad (6.21)$$

provides a measure of the error on the QCD fake rate. However, it is not clear that this correction will provide a reliable estimate in the region to which we extrapolate, or whether a correction should be used at all. We therefore use the average of the corrected and uncorrected predictions as our final estimate of the number of QCD fakes, N_f , and we use the difference in the two predictions as a measure of the systematic error:

$$N_f = \frac{1}{2}(\bar{n}_{f_o} + \bar{n}_f) \pm \sqrt{((\delta \bar{n}_f) \xi)^2 + (\bar{n}_{f_o} - \bar{n}_f)^2} \quad (6.22)$$

Chapter 7

Selected Data Sample

7.1 Efficiencies

The efficiency for the loose cuts applied to the data and each $t\bar{t}$ decay mode are listed in table 7.1. The sharp drop in efficiency for the high mass $t\bar{t} \rightarrow b\bar{b}HH$ channel is a result of the relatively soft b-jets. The effect is also apparent in the mixed decay mode, although the stiff b-jet recoiling off of the 80GeV W keeps the acceptance moderately high. The very low efficiency times branching ratio for SM production of $t\bar{t} \rightarrow \tau jet jet$ should be pointed out. The branching ratio of this mode is only 0.1, giving an acceptance*BR of 1.8%, for the 5jet sample, which contains $71.8 pb^{-1}$ of data. For $\sigma(t\bar{t}) = 5.5 pb$, we will only see 7 $t\bar{t}$ in the entire 3800 events of the JET_MULTI sample.

Table 7.2 details the efficiencies of each network for each decay mode, for a neural network cut of 0.88, where the cut means that only events for which the output of the neural network is 0.88 or higher will be kept. The decision to use the value of 0.88 is described in section 9. Only the networks trained on $t\bar{t} \rightarrow WH$, and $t\bar{t} \rightarrow HH$ are shown, because, as is expected, the efficiency for SM top quark

Event Type	Initial Events	5jet+ E_T	Eff (%)	4jet+ E_T	Eff (%)
JET_MULTI	810286	3800	0.47	6083	0.75
JET_MS_MULTI	572272	4213	0.74	9451	1.65
$W + \geq 4jet$	45899	510	1.1	972	2.1
$W + \geq 3jet$	67829	145	0.2	333	0.5
$t\bar{t} \rightarrow WW$	22345	4081	18.3	5922	26.5
$t\bar{t} \rightarrow WH, M_H = 50GeV$	16799	5115	30.4	7296	43.4
$t\bar{t} \rightarrow WH, M_H = 80GeV$	24275	4686	19.3	6788	30.0
$t\bar{t} \rightarrow WH, M_H = 110GeV$	25725	4882	19.0	7137	27.7
$t\bar{t} \rightarrow WH, M_H = 140GeV$	25000	4057	16.2	6337	25.3
$t\bar{t} \rightarrow WH, M_H = 160GeV$	25620	3306	12.9	5872	22.9
$t\bar{t} \rightarrow HH, M_H = 50GeV$	18414	2312	12.5	3857	20.9
$t\bar{t} \rightarrow HH, M_H = 80GeV$	14665	1945	13.3	3306	22.5
$t\bar{t} \rightarrow HH, M_H = 110GeV$	17008	2208	13.0	3768	22.1
$t\bar{t} \rightarrow HH, M_H = 140GeV$	24806	861	3.5	1558	6.3
$t\bar{t} \rightarrow HH, M_H = 160GeV$	18322	426	2.3	745	4.1

Table 7.1: Efficiencies of loose cuts applied to signal and data.

Net/Signal	$M_H = 50$	$M_H = 80$	$M_H = 110$	$M_H = 140$	$M_H = 160$
Neural Net output cut at 0.88					
$Eff_{WH}^{WW} (\%)$	1.8 ± 0.35	1.9 ± 0.35	1.8 ± 0.35	1.8 ± 0.30	-
Eff_{HH}^{WW}	2.7 ± 0.41	2.6 ± 0.45	2.5 ± 0.43	2.6 ± 0.45	-
Eff_{WH}^{WH}	3.3 ± 0.52	2.0 ± 0.33	2.1 ± 0.33	1.8 ± 0.27	-
Eff_{HH}^{WH}	4.8 ± 0.67	3.1 ± 0.51	3.3 ± 0.52	3.1 ± 0.51	-
Eff_{WH}^{HH}	2.3 ± 0.46	2.5 ± 0.42	2.2 ± 0.34	0.7 ± 0.14	-
Eff_{HH}^{HH}	4.3 ± 0.78	4.4 ± 0.75	3.8 ± 0.66	1.3 ± 0.22	-

Table 7.2: Efficiencies of networks for all decay modes.

pair decay is essentially the same in either a network trained on a WW mode, or one trained on a WH mode for $M_{H^+} = 80GeV$: both have the same couplings and final states. The efficiencies include the subsequent $\tau - id$ cuts, and the errors are statistical + systematic.

Chapter 8

Trigger Efficiency

This analysis uses the standard definition of jets used by the top group, part of which specifies a 0.5 cone jet. The triggers used, however, require only 0.3 cone jets. Because of this, using off-line cuts which are several GeV higher in E_T than the trigger thresholds does not guarantee 100% trigger efficiency. A 0.5 cone jet with a threshold of 15GeV, as used in this analysis, could easily fail an online cut of 10GeV if only the inner 0.3 cone portion were used to determine the energy.

The trigger efficiency was studied for the decay modes

- $t\bar{t} \rightarrow WWbb; W \rightarrow jj, W \rightarrow \tau\bar{\nu}$
- $t\bar{t} \rightarrow HWbb; W \rightarrow jj, H \rightarrow \tau\bar{\nu}$
- $t\bar{t} \rightarrow HHbb; H \rightarrow \tau\bar{\nu}, H \rightarrow \tau\bar{\nu}$

for $M_{H^+} = 50, 80, 110, 140, 160 \text{ GeV}$ and for each trigger definition for both JET_MULTI and JET_MS_MULTI. The study was carried out using the VMS_FILTER v7.18, a VMS based trigger simulator. VMS_FILTER allows one to determine the trigger efficiency for monte carlo events, when the selection cuts are close enough to the trigger requirements that inefficiency is suspected. A sample of 1000 events

for each decay mode, at each mass was used. The JET_MULTI trigger uses $E_{T_{jet}}$ as the only trigger requirement (it was found here and elsewhere [43], that the H_T cut introduced in later runs (see table 5.1) had little affect on $t\bar{t}$ events). Let $E_{T_5}^p$ denote the E_T of the fifth jet for events passing the JET_MULTI trigger, as determined with the VMS_FILTER, and E_{T_5} denotes the E_T of the fifth jet for all events in that sample. The trigger efficiency can then be expressed as:

$$\varepsilon_5 = \frac{E_{T_5}^p}{E_{T_5}} \quad (8.1)$$

Figure 8.1 shows a fit to the trigger efficiencies for $t\bar{t} \rightarrow WW$, and $t\bar{t} \rightarrow WH$ at two extreme M_H . The off-line cut of 15GeV is clearly not fully efficient. The errors

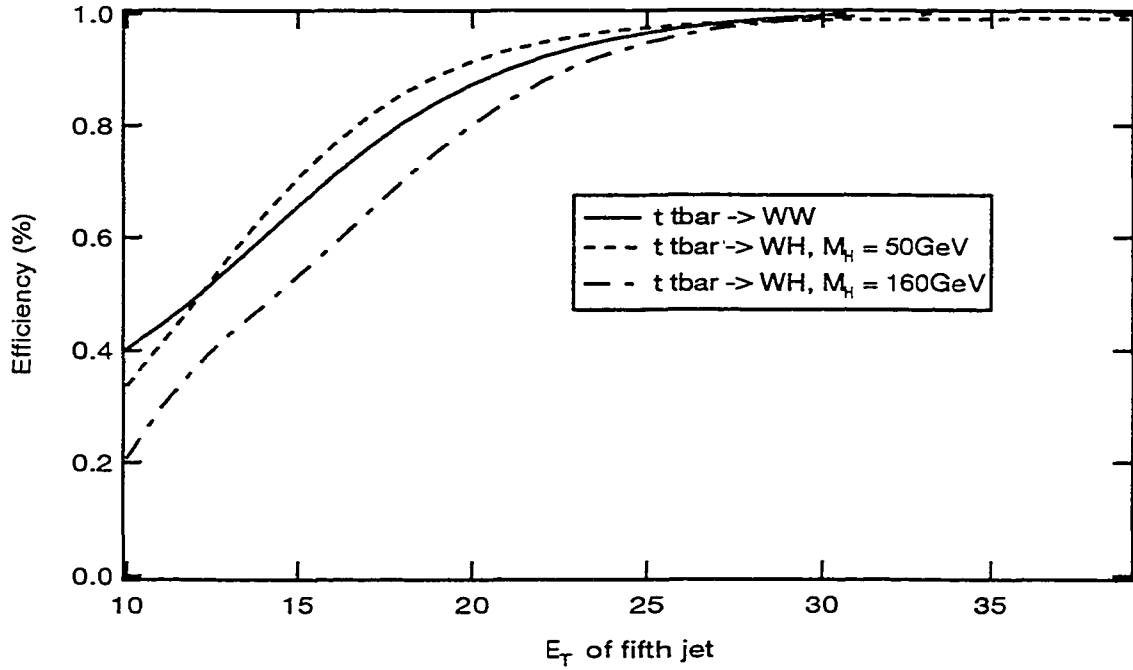


Figure 8.1: Trigger Efficiencies for standard model top decay, and top anti-top decay to W and Higgs, using the JET_MULTI trigger.

on the fits are of the order of the separation of the curves.

The JET_MS_MULTI trigger includes a E_T cut of 14GeV as well as the minimum transverse jet energy of 12GeV. However, a comparison of the efficiency as a

function of E_T for a sample with $E_T > 20\text{GeV}$ with a sample with $E_T > 30\text{GeV}$ showed no more than a 1% change, and the $E_T > 20\text{GeV}$ cut is therefore considered to be fully efficient. The JET_MS_MULTI trigger requires 4 jets, and the efficiency is determined by:

$$\varepsilon_4 = \frac{E_{T_4}^p}{E_{T_4}} \quad (8.2)$$

Figure 8.2 shows a fit to the trigger efficiencies for $t\bar{t} \rightarrow HH$ at two extreme M_H . The off-line cut of 20GeV is again not fully efficient. The trigger efficiency for the

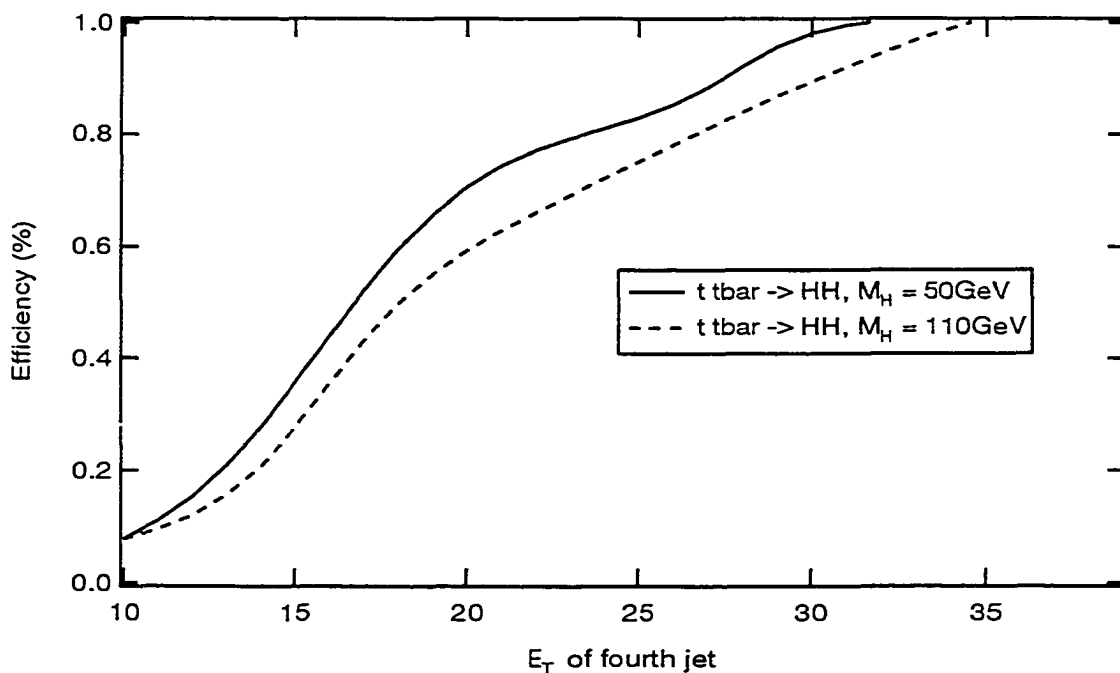


Figure 8.2: Trigger Efficiencies for top anti-top decay to Higgs Higgs, using the JET_MS_MULTI trigger.

final data sample selected, however, is the only number of real interest. Once the final set is selected, the average trigger efficiency can be calculated:

$$\langle \varepsilon_n \rangle = \frac{\int \varepsilon_n E_{T_n} dE_{T_n}}{\int E_{T_n} dE_{T_n}} \quad (8.3)$$

Table 8.1 lists $\langle \varepsilon_n \rangle$ for all decay modes, and extreme M_H . The reason for the high average efficiencies can be seen in figures 8.3 - 8.5. The E_T of the fourth and

Mode	Trigger	$\langle \varepsilon_n \rangle$
$t\bar{t} \rightarrow WW$	JET_MULTI	98%
$t\bar{t} \rightarrow WH, M_H = 50\text{GeV}$	JET_MULTI	99%
$t\bar{t} \rightarrow WH, M_H = 160\text{GeV}$	JET_MULTI	98%
$t\bar{t} \rightarrow HH, M_H = 50\text{GeV}$	JET_MS_MULTI	95%
$t\bar{t} \rightarrow WH, M_H = 110\text{GeV}$	JET_MS_MULTI	95%

Table 8.1: Average trigger efficiencies for the final data set.

fifth jets of the final sample are contained mainly in the region of high efficiency.

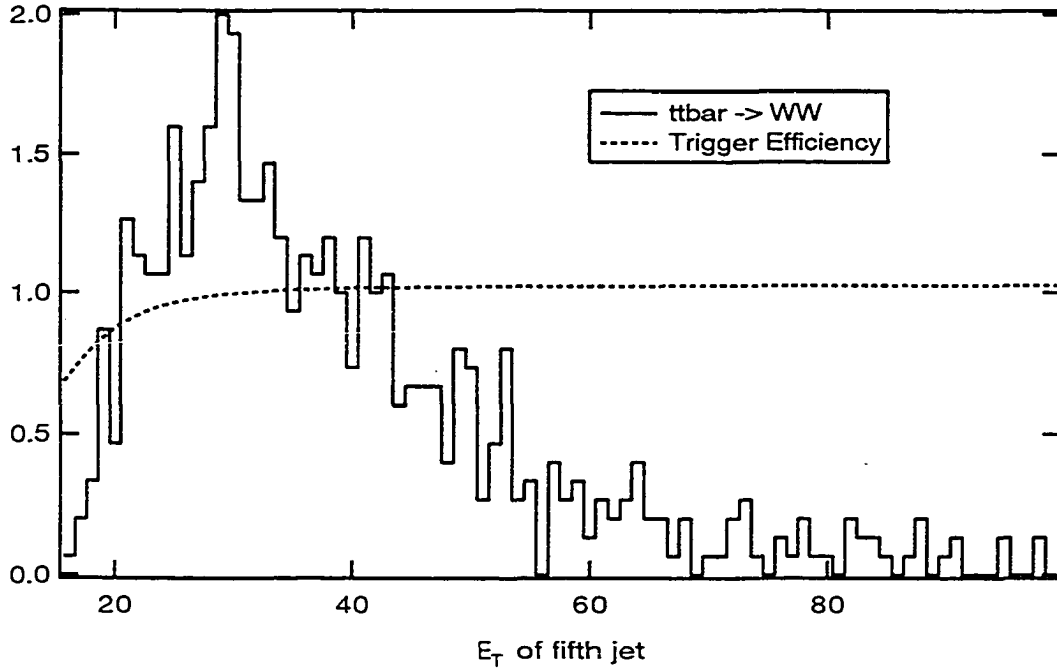


Figure 8.3: Trigger efficiency for standard model decay, and the distribution of E_{T_s} for the same mode.

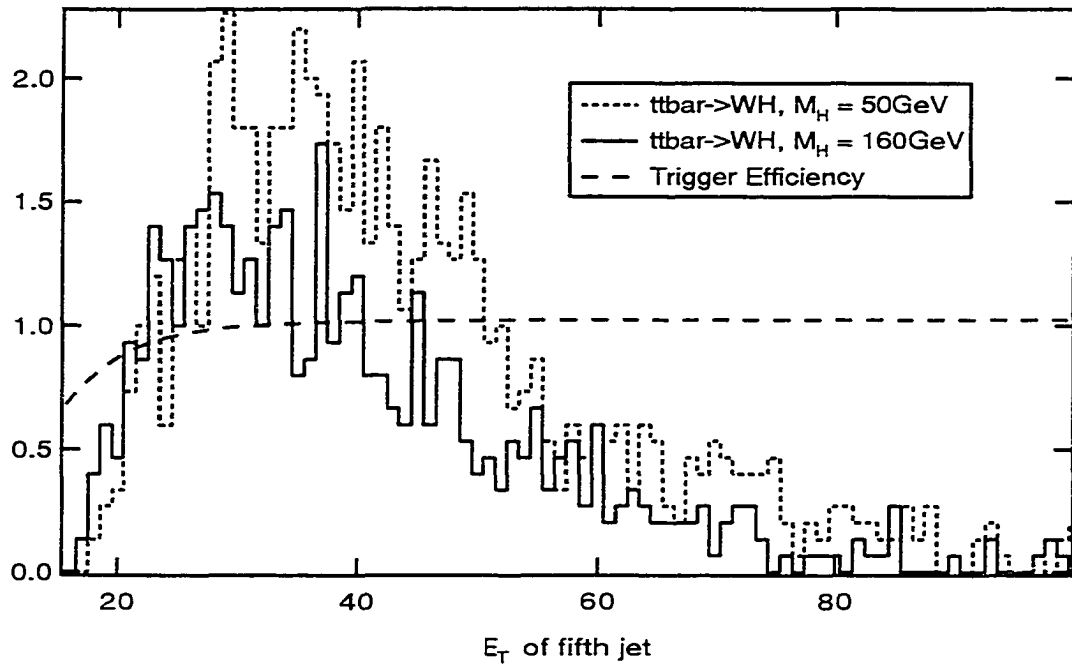


Figure 8.4: Distribution of E_{T_5} for $t\bar{t} \rightarrow WH$, overlaid on the trigger efficiency for standard model decay.

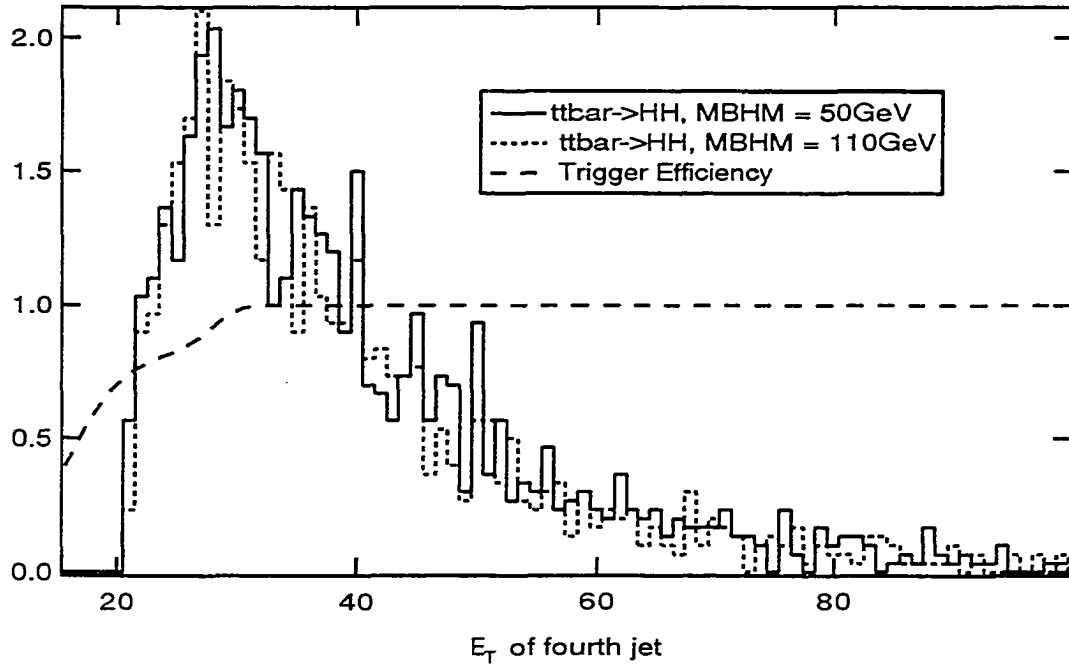


Figure 8.5: Distribution of E_{T_4} for $t\bar{t} \rightarrow HH$, overlaid on the trigger efficiency for the HH mode, with $M_H = 50\text{ GeV}$.

Chapter 9

Results

With signal acceptances, trigger efficiencies and background contributions known, the final number of events expected in each network, NN_{XX}^e can be calculated as:

$$NN_{XX}^e = \left(\mathcal{L}_f \sigma(t\bar{t}) \sum_{YY} BR(t\bar{t} \rightarrow YY) Eff_{XX}^{YY} \right) + N_{XX}^{QCD} + N_{XX}^{W+jet} \quad (9.1)$$

Where

- \mathcal{L}_f is the total luminosity used from the filter f .
 - JET_MULTI : $\mathcal{L} = 71.8 \text{ pb}^{-1}$
 - JET_MS_MULTI : $\mathcal{L} = 62.2 \text{ pb}^{-1}$
- $\sigma(t\bar{t})$ is the production cross section for top quark pair production. These results are quoted with $\sigma(t\bar{t}) = 5.5 \text{ pb}$.
- $BR(t\bar{t} \rightarrow YY)$ is the branching ratio of $t\bar{t}$ to the mode YY
- N_{XX}^{QCD} is the expected number of QCD background events.
- N_{XX}^{W+jet} is the expected number of W+jets events.

Network	QCD	W+jets	SM	Total	Measured
NN output > 0.88					
$NN_{WH}, M_H = 50$	0.9 ± 0.6	0.94 ± 0.28	0.73 ± 0.12	2.6 ± 0.67	1
$NN_{WH}, M_H = 80$	0.9 ± 0.6	1.0 ± 0.3	0.73 ± 0.14	2.6 ± 0.68	1
$NN_{WH}, M_H = 110$	0.98 ± 0.6	0.91 ± 0.3	0.71 ± 0.14	2.6 ± 0.69	1
$NN_{WH}, M_H = 140$	0.9 ± 0.27	0.91 ± 0.27	0.7 ± 0.12	2.5 ± 0.7	1
$NN_{HH}, M_H = 50$	3.2 ± 1.6	1.3 ± 0.44	0.9 ± 0.15	5.4 ± 1.7	3
$NN_{HH}, M_H = 80$	3.3 ± 1.6	1.3 ± 0.33	0.88 ± 0.15	5.5 ± 1.6	2
$NN_{HH}, M_H = 110$	3.0 ± 1.5	1.3 ± 0.5	0.86 ± 0.15	5.2 ± 1.6	2
$NN_{HH}, M_H = 140$	3.0 ± 1.7	1.3 ± 0.44	0.9 ± 0.15	5.2 ± 1.8	2

Table 9.1: Expected and measured events for each network. Notice the similarity in the expected events for a given network type (NN_{XX}), indicating large correlations.

Figures 9.1 - 9.8 show the expected number of events, and the events measured, for the networks trained on $t\bar{t} \rightarrow WHbb$ and $t\bar{t} \rightarrow HHbb$. The notation “Sig+Back given SM” means the number of events expected if only the SM decay of top is allowed.

Let the mean number of events expected for some NN output cut, including background, be b , with error σ_b , and let the number of measured events be n . The appearance of charged Higgs serves to increase the expected number of events in the $t\bar{t} \rightarrow \tau + X$ channel, and the probability, P , that our expected Higgs signal has fluctuated to our measured number of events is:

$$P(n, b, \sigma_b) = \int_0^\infty d\mu \frac{\mu^n e^{-\mu}}{n!} \frac{1}{\sqrt{2\pi}\sigma_b} e^{-(\mu-b)^2/2\sigma_b^2} \quad (9.2)$$

Recall that the total number of events in each network includes all possible sources. That is, when calculating the total number expected in the network trained on $t\bar{t} \rightarrow HWbb$, we include:

1. $t\bar{t} \rightarrow WWbb$
2. $t\bar{t} \rightarrow WHbb$
3. $t\bar{t} \rightarrow HHbb$

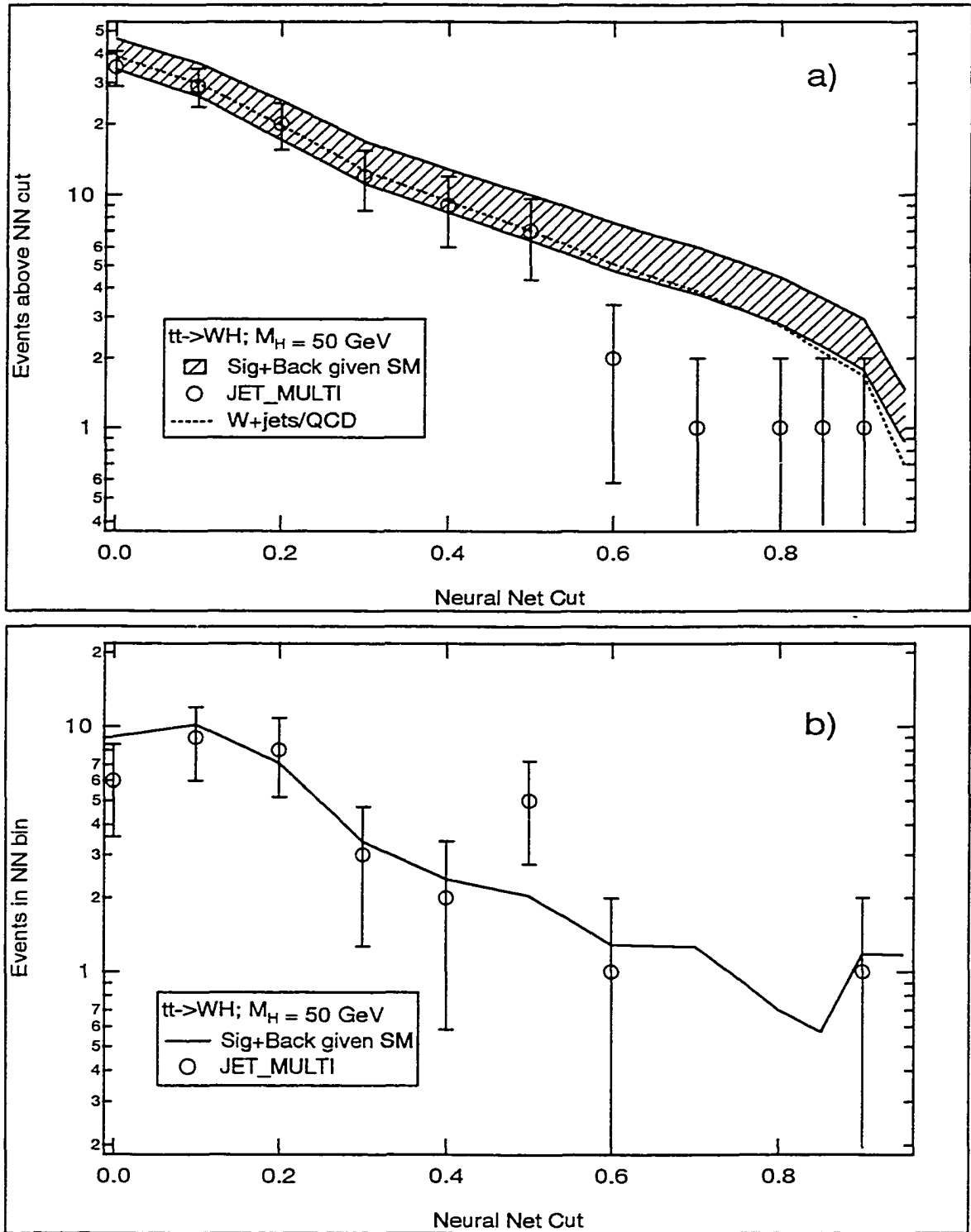


Figure 9.1: Expected and measured events as a function of neural network cut, for the network trained on $t\bar{t} \rightarrow WH$, for $M_H = 50 \text{ GeV}$.

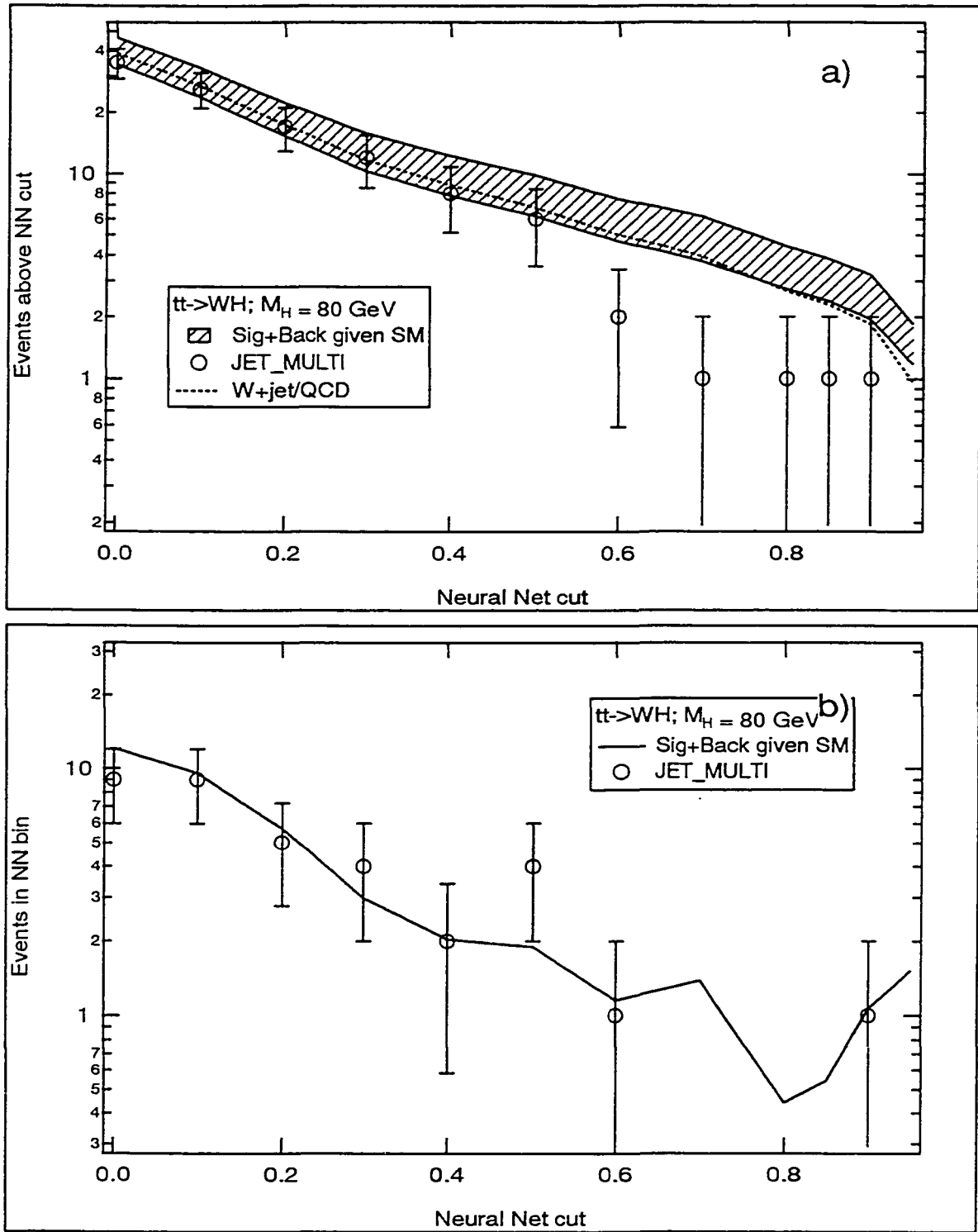


Figure 9.2: Expected and measured events as a function of neural network cut, for the network trained on $t\bar{t} \rightarrow WH$, for $M_H = 80\text{GeV}$.

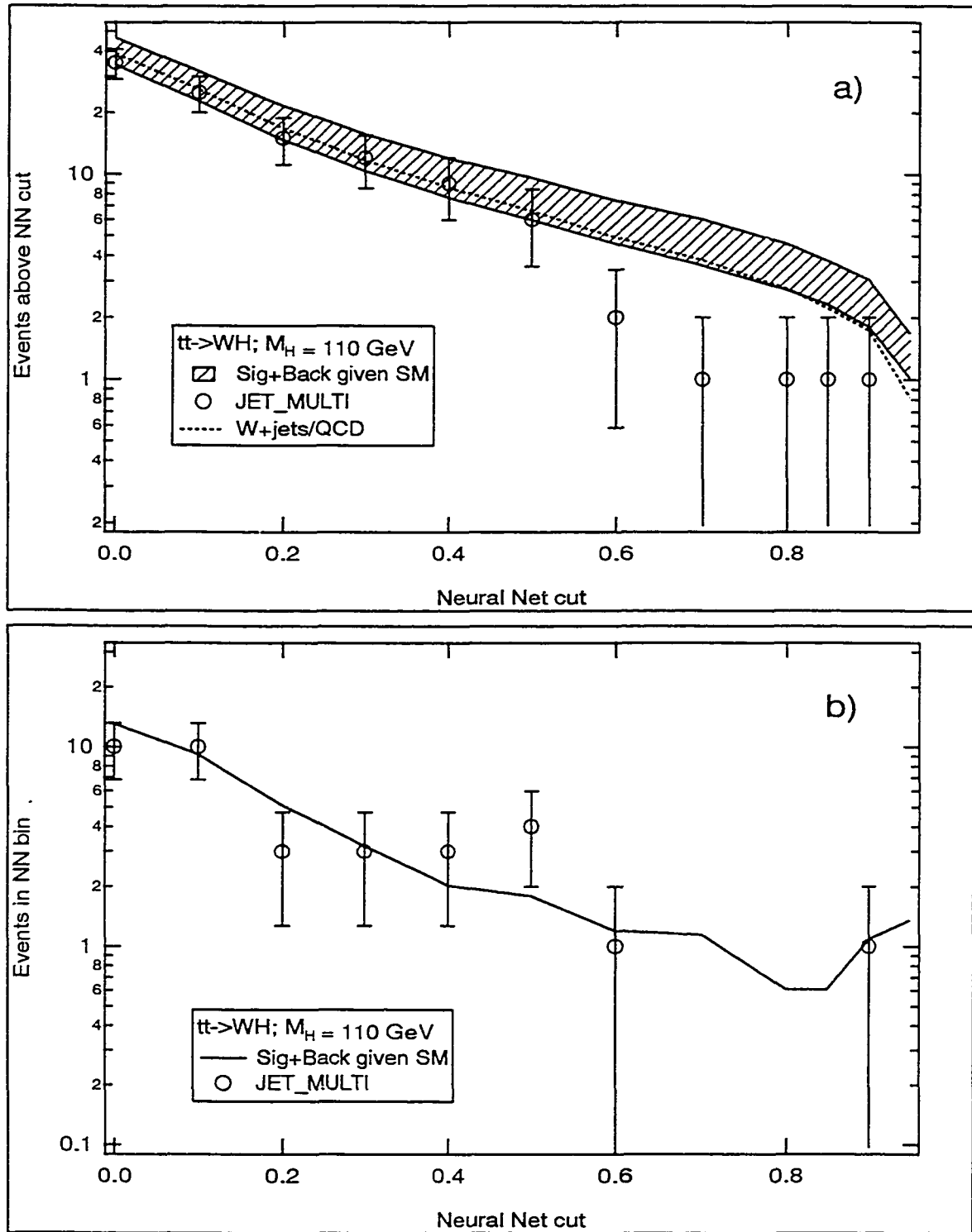


Figure 9.3: Expected and measured events as a function of neural network cut, for the network trained on $t\bar{t} \rightarrow WH$, for $M_H = 110 \text{ GeV}$.

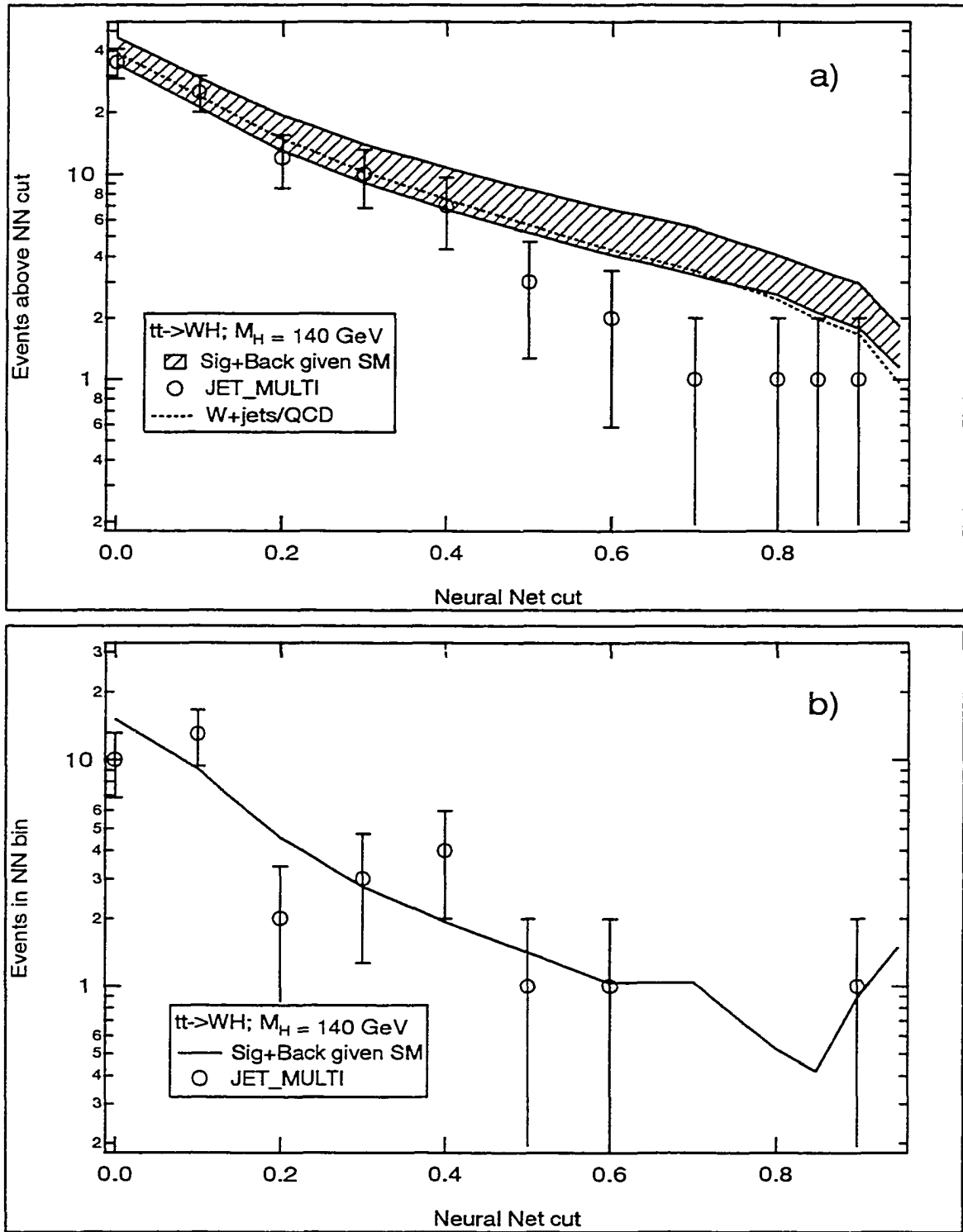


Figure 9.4: Expected and measured events as a function of neural network cut, for the network trained on $t\bar{t} \rightarrow WH$, for $M_H = 140 \text{ GeV}$.

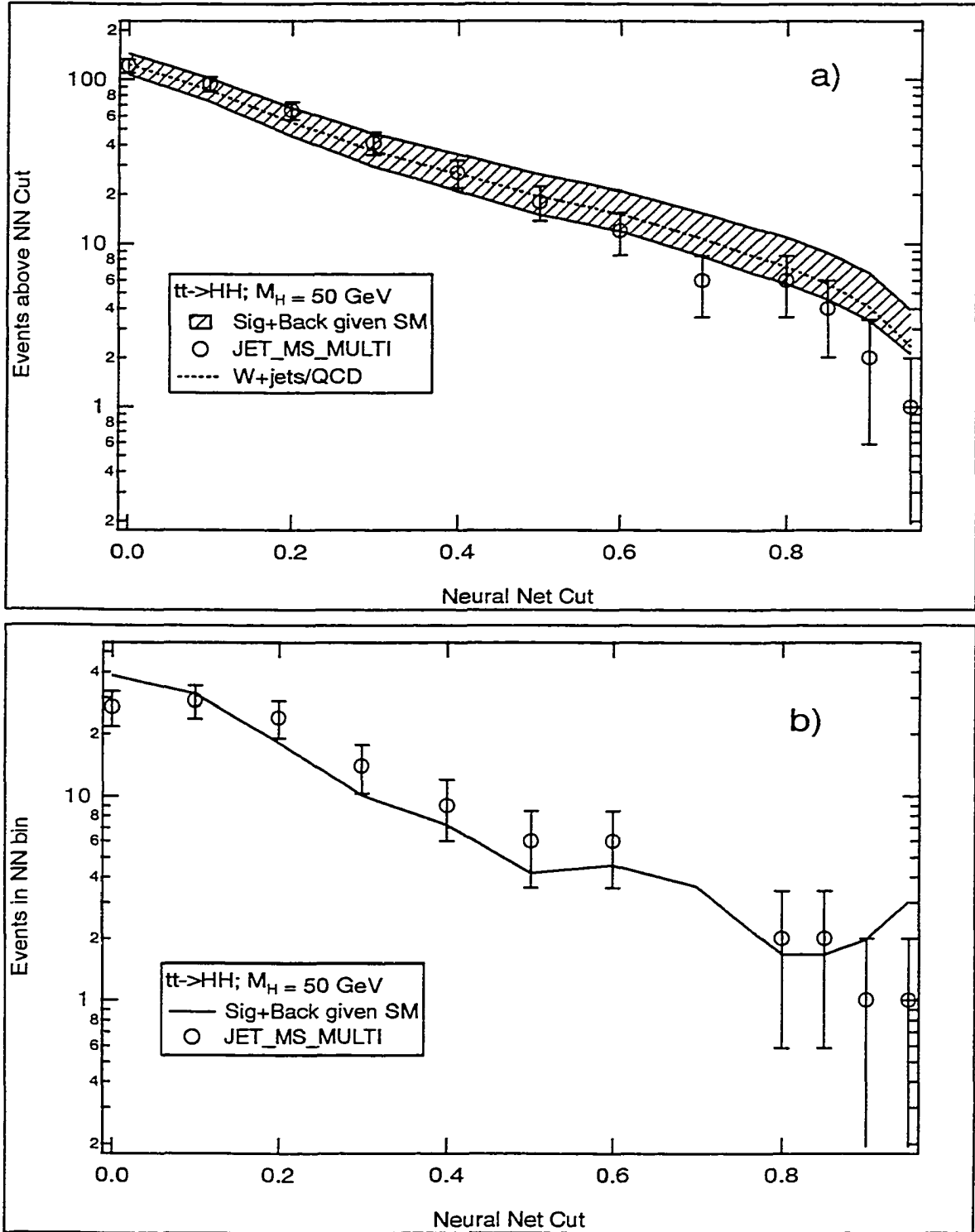


Figure 9.5: Expected and measured events as a function of neural network cut, for the network trained on $t\bar{t} \rightarrow HH$, for $M_H = 50 \text{ GeV}$.

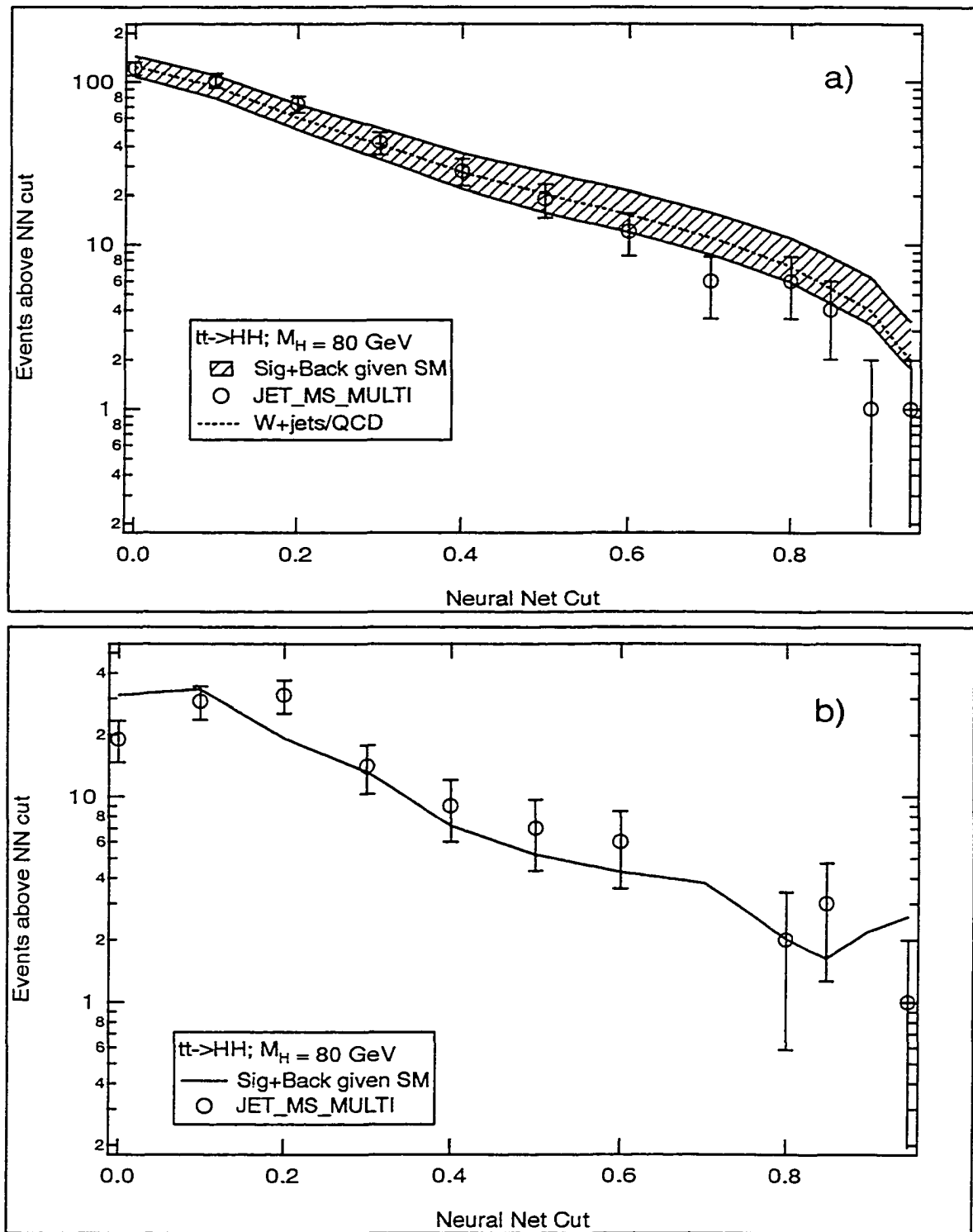


Figure 9.6: Expected and measured events as a function of neural network cut, for the network trained on $t\bar{t} \rightarrow HH$, for $M_H = 80\text{GeV}$.

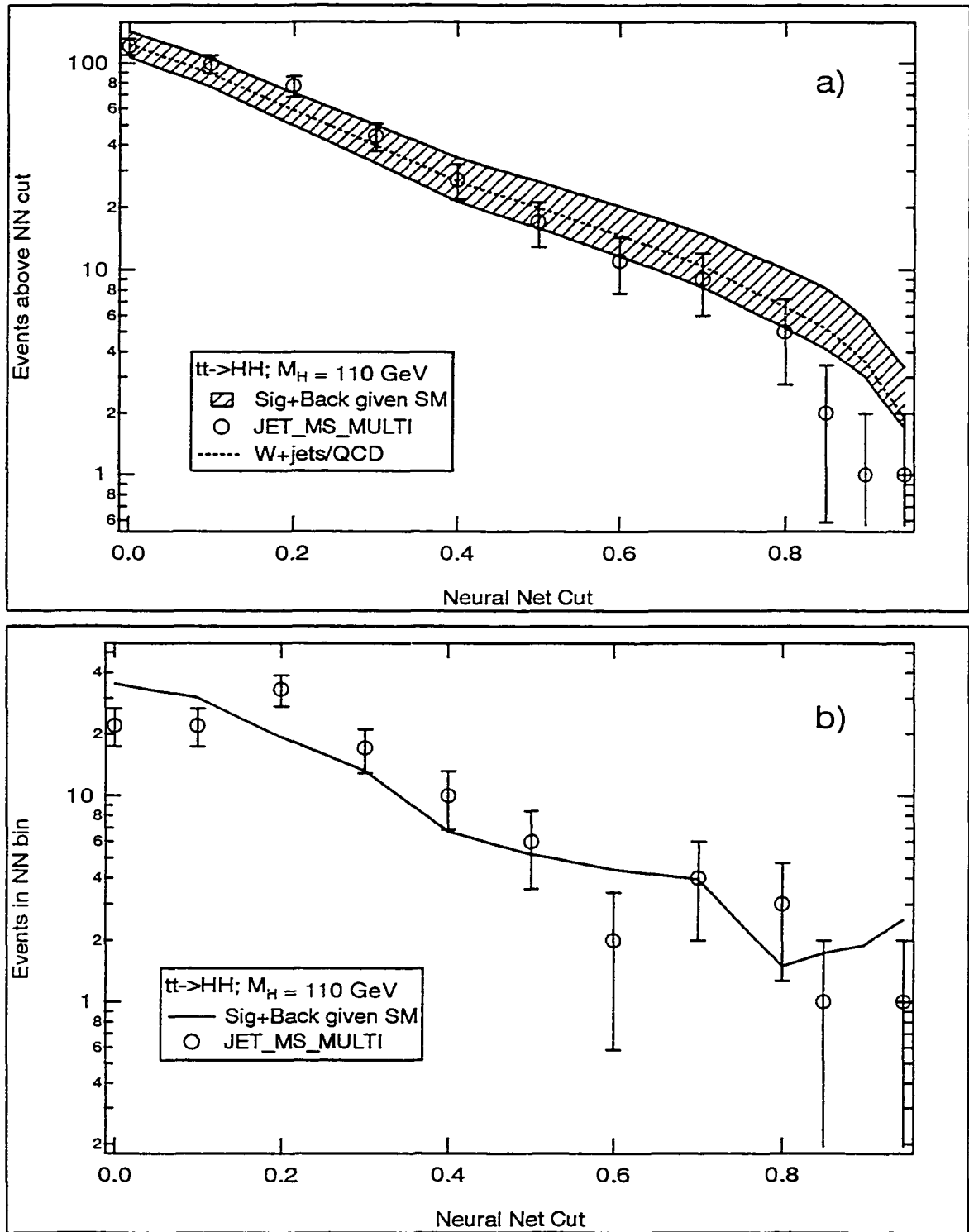


Figure 9.7: Expected and measured events as a function of neural network cut, for the network trained on $t\bar{t} \rightarrow HH$, for $M_H = 110 \text{ GeV}$.

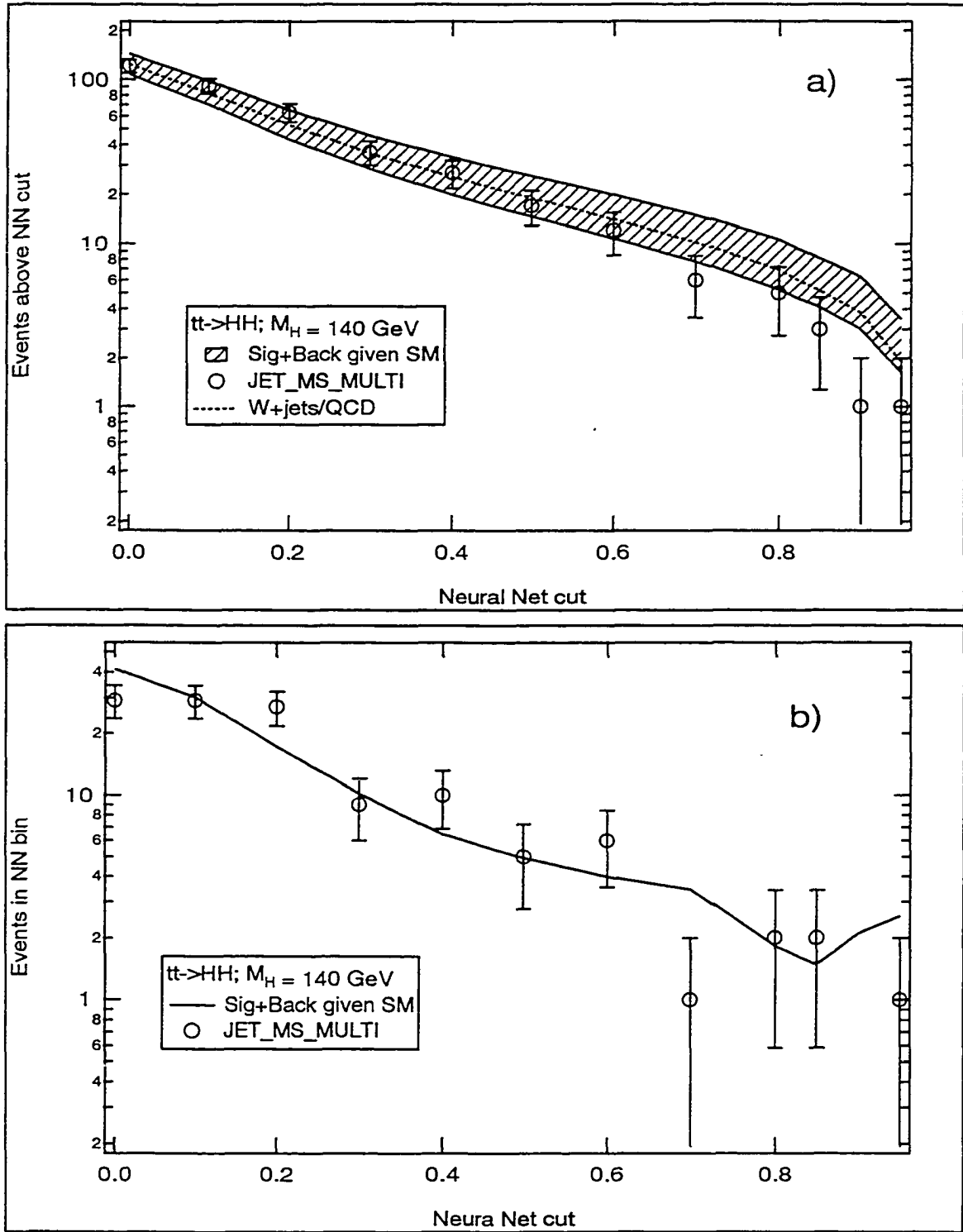


Figure 9.8: Expected and measured events as a function of neural network cut, for the network trained on $t\bar{t} \rightarrow HH$, for $M_H = 140 \text{ GeV}$.

Signal type	α for a network trained on Higgs mass:			
	50GeV	80GeV	110GeV	140GeV
$t\bar{t} \rightarrow WW$	0.531	0.516	0.471	0.467
$t\bar{t} \rightarrow WH$	0.641	0.524	0.433	0.403
$t\bar{t} \rightarrow HH$	0.425	0.390	0.365	0.315
$W + jets$	0.262	0.250	0.265	0.241

Table 9.2: Fractions of signals found in the NN_{HH} output which were also found in the output of NN_{WH} .

4. $W + jets$, QCD

Where all signals are subject to the $5jet + \cancel{E}_T$ cuts. In a separate measurement, we consider the events expected in a network trained on $t\bar{t} \rightarrow HHbb$, and include all sources subject to the $4jet + \cancel{E}_T$ cuts. If the two measurements were independent, the joint probability that we make each measurement, given the existence of H^+ , would simply be the product of the individual probabilities, improving our ability to rule out H^+ . This is not the case.

The original sets of events, in MC and data, are separated into three regions of parameter space by the process of selecting events passing the $5jet + \cancel{E}_T$ loose cuts, and the NN cuts applied by the NN_{WH} network, or the $4jet + \cancel{E}_T$ and NN_{HH} cuts. Let the set of events passing the former cuts be denoted B , and events passing the latter be denoted A , and the set of events in common between the two be denoted $A \cdot B$. A schematic diagram of this separation of events is shown in figure 9.9. Let α denote the fraction of A which is also included in B . It is clear that if α is non-zero, our measurement of the set A will affect our prediction of the set B , and that apriori information decreases the usefulness of B in improving our limit. Table 9.2 gives the value of α for all signals. The choice of using A , B or both in the calculation of the final limit depends on the method used, and the amount of overlap expected. In the case of a frequentist analysis (Section 9.2), the amount of additional information contained in, say, B given a measurement on A is a major concern. If all of the H^\pm in B were also in

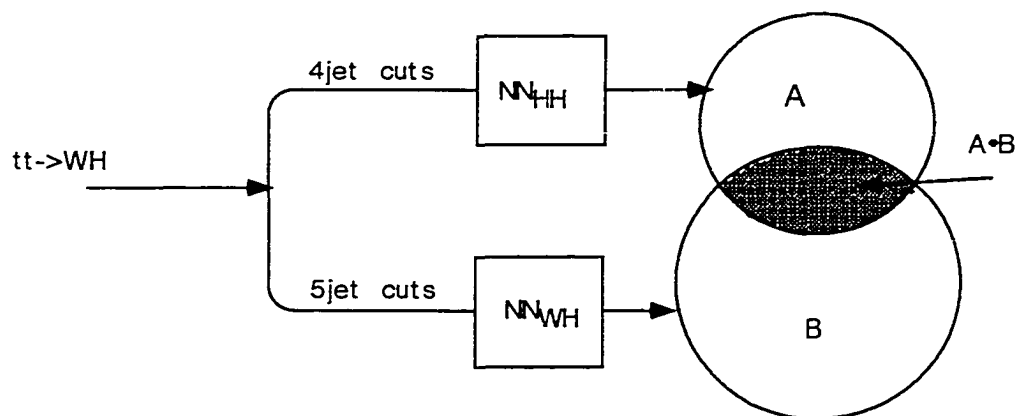


Figure 9.9: Schematic of how $t\bar{t} \rightarrow WHbb$ might be separated by the two sets of cuts and neural network selection.

A, no new information could be gleaned from a measurement on B, and we would weaken the limit because we include nothing more than background. Table 9.2 shows the fraction of the $4jet + \cancel{E}_T$ sample which is in the $5jet + \cancel{E}_T$ sample, but the $5jet + \cancel{E}_T$ sample is obviously smaller. In fact, 80 – 95% of the $5jet + \cancel{E}_T$ is found in the $4jet + \cancel{E}$ sample. Although a Bayesian approach is not sensitive to the addition of a flat background, the complication of removing the large measured overlap for an improvement which is expected to be minimal has motivated the choice to set limits based on A or B, but not both. According to the efficiencies listed in table 7.2, we expect stronger limits when using the NN_{HH} network, despite the fact that it uses JET_MS_MULTI, which has about a 9% reduction in \mathcal{L} as compared to JET_MULTI. For that reason, we choose to set limits based on our measurements with the NN_{HH} network.

9.0.1 Accessible region of parameter space

We rely on Monte Carlo for our estimates of the expected number of H^+ decays, and our search must be limited to the parameter space in which our MC remains valid. At leading order, the Yukawa couplings of the top and bottom quarks to charged Higgs are:

$$h_t = \frac{m_t}{v \sin \beta}, \quad h_b = \frac{m_b}{v \cos \beta} \quad (9.3)$$

$$\begin{aligned} v &= \frac{\sqrt{2}M_W}{e} \sin \theta_W \\ &= 174.1 \text{ GeV} \end{aligned} \quad (9.4)$$

In order to stay in the perturbative region, we require that the coupling strengths be less than one:

$$\alpha_h \equiv \frac{h_f^2}{4\pi} < 1 \quad (9.5)$$

which translates to approximately:

$$0.3 < \tan \beta < 150 \quad (9.6)$$

Leading order calculations cannot be trusted if $|m_t - m_{H^+}|$ is small and either $\Gamma(t)$ or $\Gamma(H^+)$ is large. The latter also brings into question the reliability of our MC. We therefore require:

$$\Gamma(t) < 10 \times \Gamma(t \rightarrow W^+ b) \quad (9.7)$$

$$\Gamma(H^+) < 7.5 \text{ GeV} \quad (9.8)$$

which limits our search to $BR(t \rightarrow H^+) < 0.9$, and $m_{H^+} < 160 \text{ GeV}$.

9.0.2 Estimation of low $\tan \beta$

When the large amount of MC needed for this analysis was generated, the purpose was the exclusion of H^+ in the region where the $BR(H^+ \rightarrow \tau)$ was large, that is, high $\tan \beta$. However, if one is to set a limit using the Bayesian prescription, the entire range of allowable $\tan \beta$ must be probed. The decays for which no MC exists are:

1. $t\bar{t} \rightarrow WH; W \rightarrow \tau\bar{\nu}, H \rightarrow c\bar{s}$
2. $t\bar{t} \rightarrow WH; W \rightarrow jj, H \rightarrow Wb, W \rightarrow \tau\bar{\nu}$
3. $t\bar{t} \rightarrow WH; W \rightarrow \tau\bar{\nu}, H \rightarrow Wb, W \rightarrow jj$
4. $t\bar{t} \rightarrow HH; H \rightarrow \tau\bar{\nu}, H \rightarrow c\bar{s}$
5. $t\bar{t} \rightarrow HH; H \rightarrow \tau\bar{\nu}, H \rightarrow Wb, W \rightarrow jj$
6. $t\bar{t} \rightarrow HH; H \rightarrow Wb, W \rightarrow \tau\bar{\nu}, H \rightarrow Wb, W \rightarrow jj$
7. $t\bar{t} \rightarrow HH; H \rightarrow Wb, W \rightarrow \tau\bar{\nu}, H \rightarrow c\bar{s}$

where all additional decays contain $5jets + \cancel{E}_T$ in the final state, and whose efficiencies are known in the indirect search. We estimate the efficiency for each of these channels by:

1. Cases 1-3

- Let the efficiency and error on efficiency of this mode be Eff_{WH}^{WW} with the error on Eff_{WH}^{WW} , for the case of $M_{H^+} = 80GeV$. That is, we assume that the $W \rightarrow \tau\bar{\nu}$ looks like the $H^+ \rightarrow \tau\bar{\nu}$, and that the $H \rightarrow c\bar{s}$ looks like the $W \rightarrow jj$.
- Scale the efficiency and error on efficiency as a function of M_{H^+} according to the mass dependence found in the case $t\bar{t} \rightarrow H^+bW^-\bar{b}$; $H^+ \rightarrow c\bar{s}$ in the indirect search [9].

2. Case 4-7

- Let the efficiency and error on efficiency of this mode be Eff_{HH}^{WW} , for the case of $M_{H^+} = 80GeV$. This has the same implication as in cases 1-3.
- Scale the efficiency and error on efficiency as a function of M_{H^+} according to the mass dependence found in the case $t\bar{t} \rightarrow H^+bH^-\bar{b}$; $H^+ \rightarrow c\bar{s}$, $H^- \rightarrow \tau\bar{\nu}$ in the indirect search.

These estimates are quite crude, and we do not expect them to reflect the real efficiencies of the low $\tan\beta$ decay modes; however, our lack of knowledge does not hurt us too much, because the branching ratios of these additional modes are quite small. Figure 9.10 shows the branching ratios for modes where at least one top quark decays to a W , and all BR s include the 65% $BR(\tau \rightarrow jet)$. Note that the only mode with a large BR is the mode for which we have MC. Figure 9.11 shows BR s for modes where both top quarks decay to a H^+ . The error on the efficiency for these additional modes are taken to be the same fractional error as that for $t\bar{t} \rightarrow WW$, or about 20%. Because we have little faith in our estimate, we should investigate the effect of changing this efficiency. We consider the effect of raising the efficiency by a factor of two, or a 5σ change. Figure 9.12 shows the

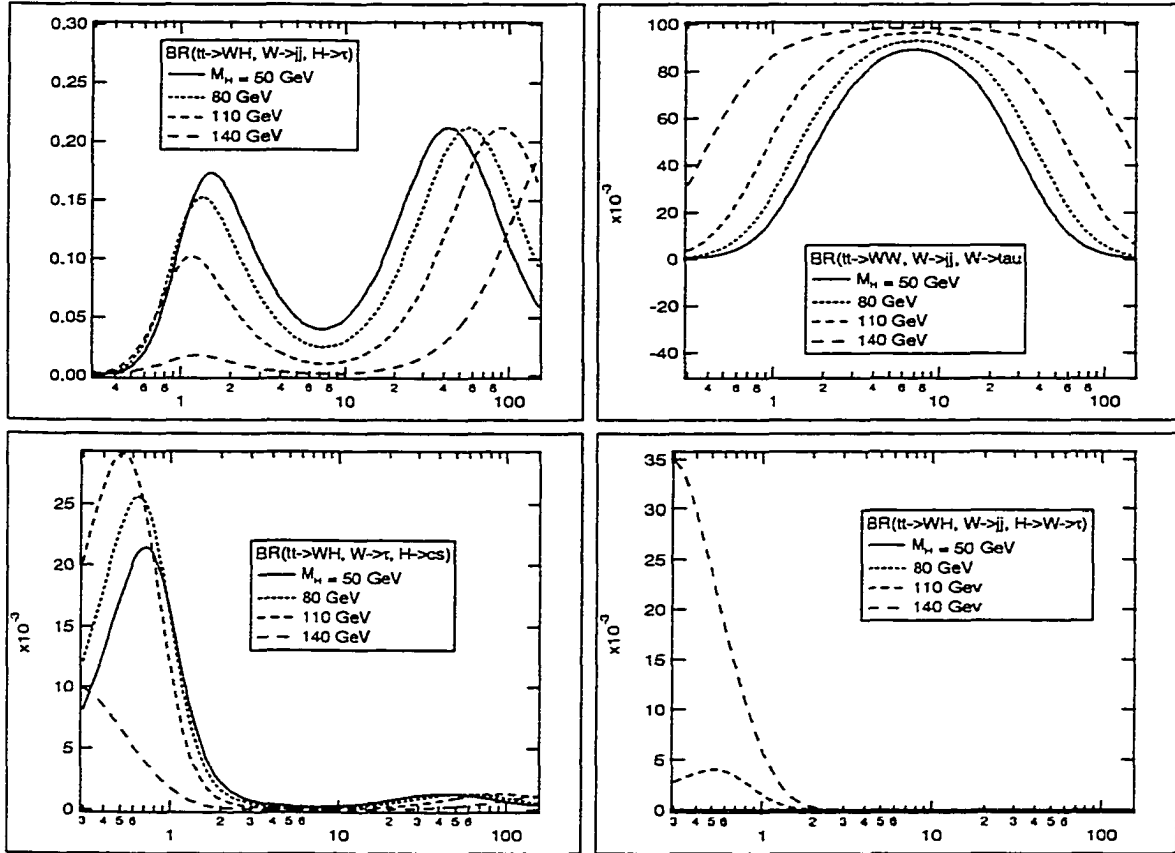


Figure 9.10: Branching ratios of various $t\bar{t} \rightarrow WX$ final states.

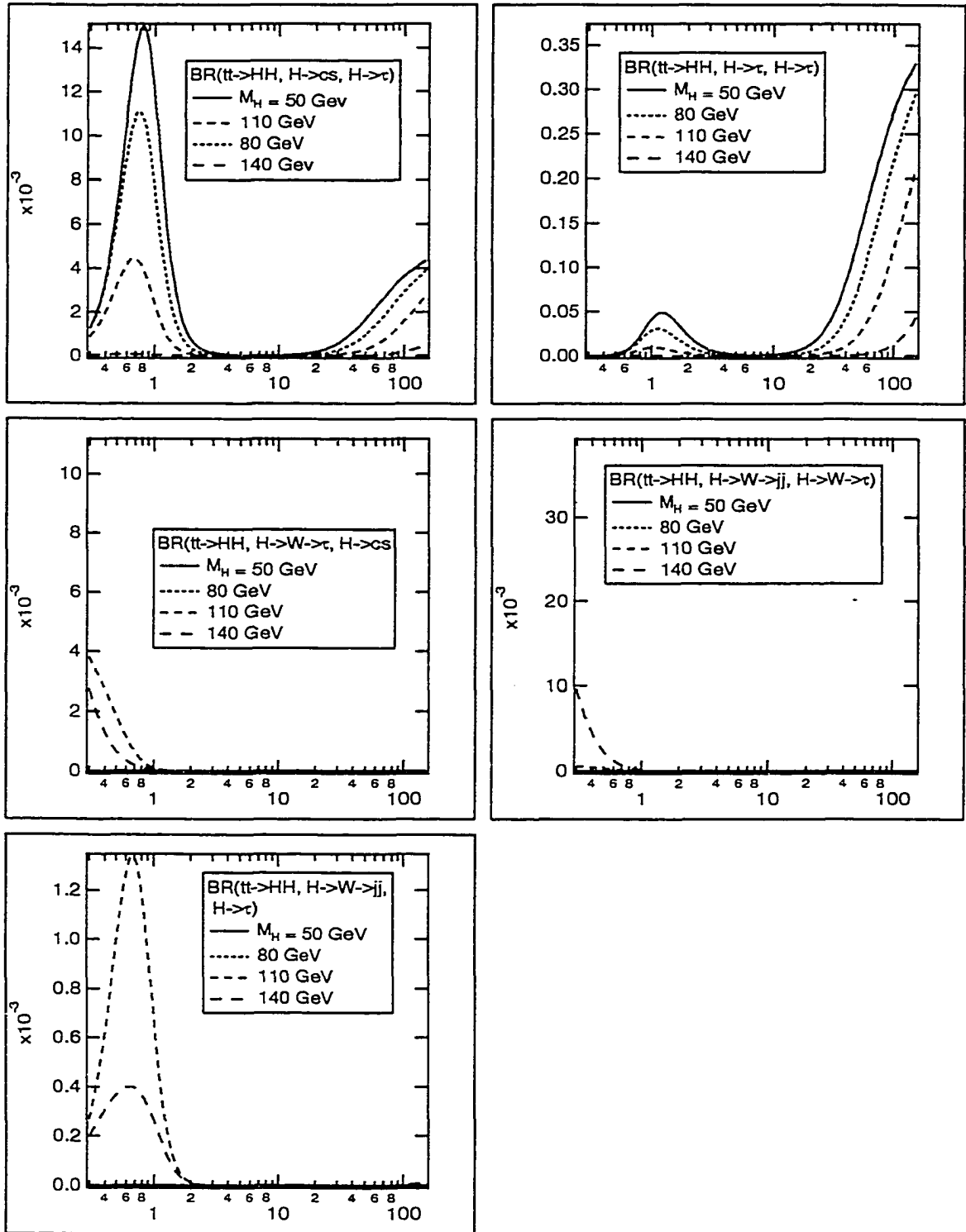


Figure 9.11: Branching ratios of various $t\bar{t} \rightarrow HH$ final states.

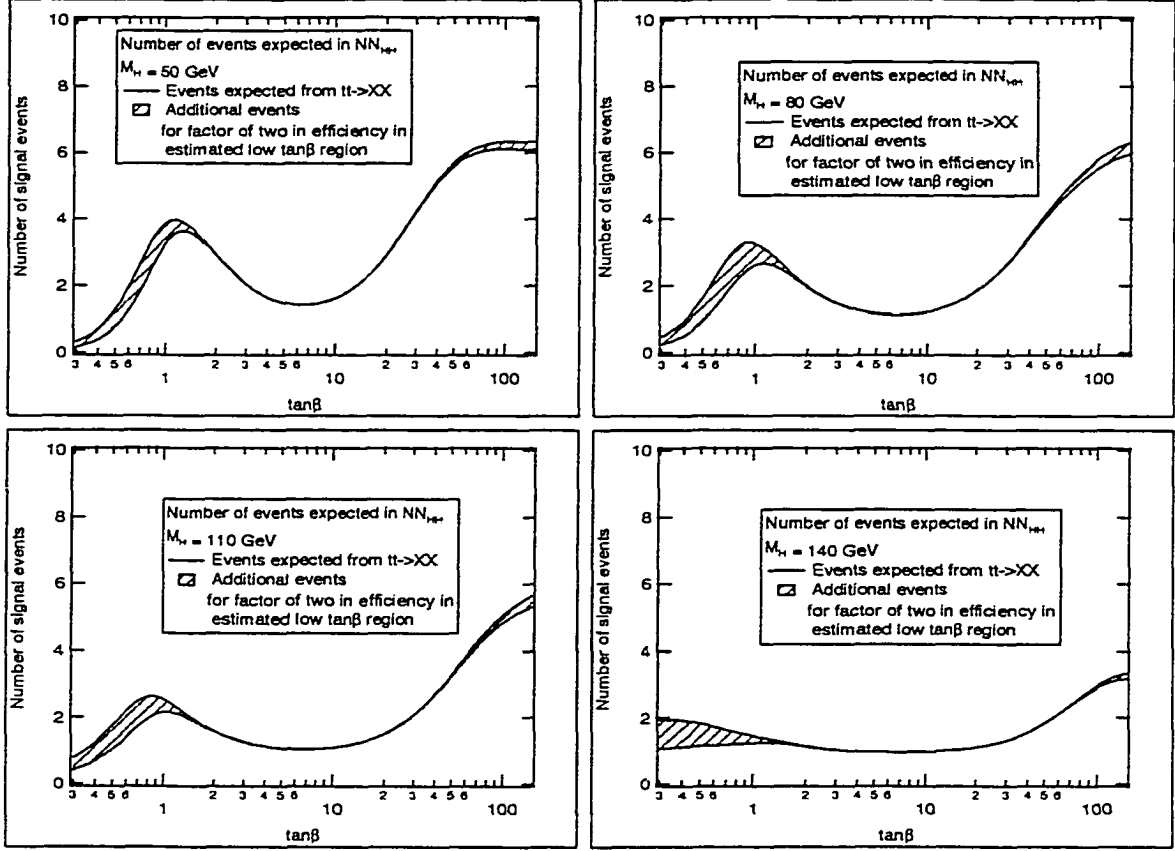


Figure 9.12: Number of events from $t\bar{t}$ decay expected in the NN_{HH} network, including the estimated modes for low $\tan\beta$.

number of events due to $t\bar{t}$ decay only, which are expected in the NN_{HH} network for a NN cut of 0.88, as a function of $\tan\beta$. The effect of raising the efficiencies of all estimated decays by a factor of 2 is also shown.

The number of expected events maps onto some probability curve, as indicated by equation 9.2. Figure 9.13 shows the probability curves, where, in reference to equation 9.2, n is the number of events measured in JET_MS_MULTI, b is the number of events expected from $W + jet$, QCD , and $t\bar{t} \rightarrow XX$ for a NN cut of 0.88. Also shown is the change in $P(n, b, \sigma_b)$ resulting in an increase of the estimated efficiencies by a factor of two. In the Bayesian approach to setting limits, we integrate the probabilities to a point, $\tan\beta_0$, which is the point where 95% of the area under the probability curve has been integrated, corresponding to

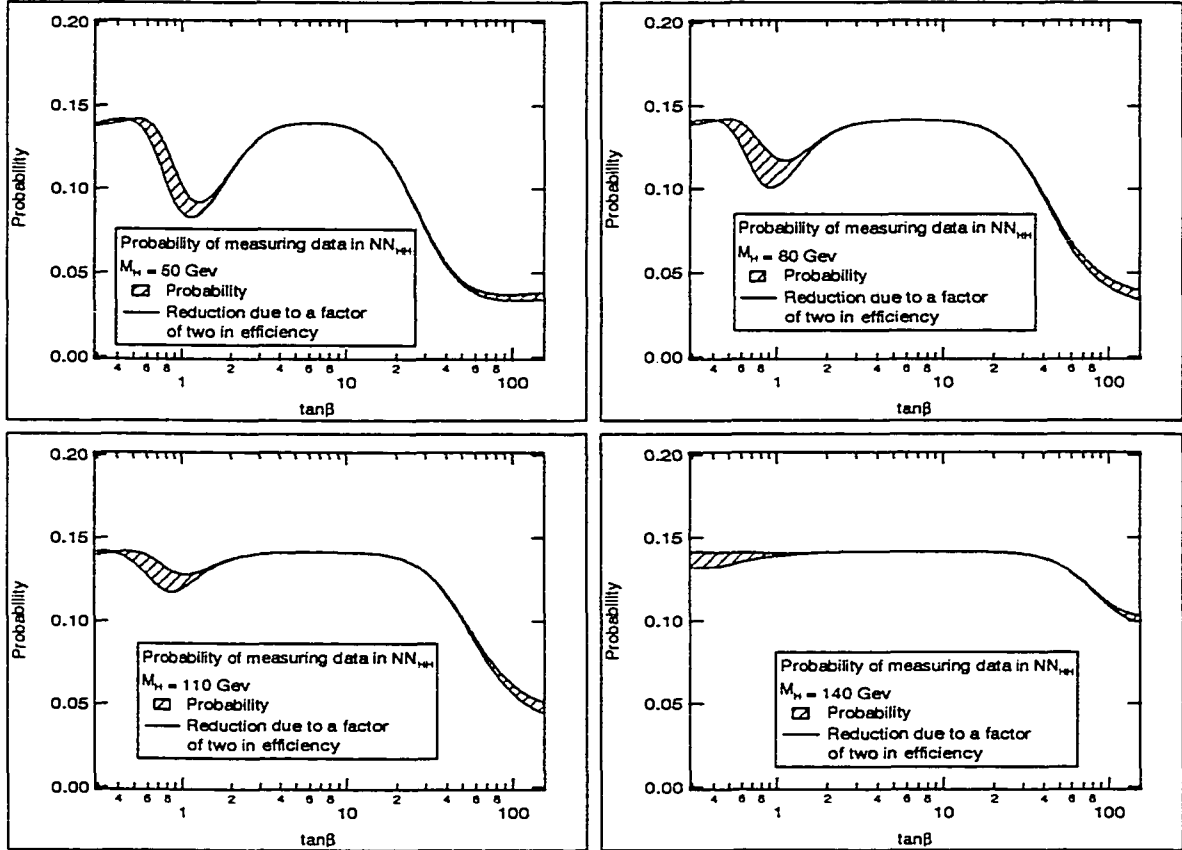


Figure 9.13: Probability that we measure the data, given all $t\bar{t}$ decays, including the effect of increasing the low $\tan\beta$ estimates by a factor of two.

the 95% confidence limit on $\tan \beta$. Figure 9.13 shows that the change in area due to the change in efficiency is of order 5%, and because the change occurs at low $\tan \beta$, we expect the effect on the limit to be negligible.

9.1 Bayesian Results

In the Bayesian method [44][45], we are not concerned with the absolute probability of measuring n given a parent distribution with mean b , but with the relative probability. That is, given a measurement n , what values of $\tan \beta$ and M_{H+} are most probable.

$$P(\tan \beta, M_{H+}|n) = \frac{P(n|\tan \beta, M_{H+})P(\tan \beta, M_{H+})}{\int \int P(n|\tan \beta, M_{H+})dM_{H+}d(\tan \beta)} \quad (9.9)$$

We rule out values of $(\tan \beta, M_{H+})$ which are less than 5% likely, given our measurement. We assume all $(\tan \beta, M_{H+})$ are equally likely, so that

$$P(\tan \beta, M_{H+}|n) \sim \frac{P(n|\tan \beta, M_{H+})}{\int \int P(n|\tan \beta, M_{H+})dM_{H+}d(\tan \beta)} \quad (9.10)$$

At this point, we have generated, using equation 9.2, the probability of measuring exactly n events, as a function of $\tan \beta$ for some particular Higgs mass, M_{H+}^i , $P(n^i|\tan \beta, M_{H+}^i)$. Because the networks were optimized on different M_{H+} and each network made a different but correlated measurement, we cannot directly write equation 9.9, which is a continuous function of $\tan \beta$, M_{H+} for *fixed* n . In the case of many measurements, equation 9.9 must be written:

$$P(\tan \beta, M_{H+}|\vec{n}) \sim P(\vec{n}|\tan \beta, M_{H+}) \quad (9.11)$$

where \vec{n} is a vector of the number of measured events for each network. The problem is in writing $P(\vec{n}|\tan \beta, M_{H+})$ in terms of what we know, $P(n^i|\tan \beta, M_{H+}^i)$. The problem would be greatly simplified if one measurement could be made, and from that $P(n|\tan \beta, M_{H+})$ calculated for any M_{H+} . The only possible drawback is the loss of efficiency caused by using a network trained on one Higgs mass to look for decays from some other Higgs mass. Figure 9.14 shows the effect of using a network trained on one Higgs mass to search for decays from some other Higgs mass. The errors shown in Figure 9.14 are statistical only, and when considering that the total error is around 20% of the efficiency, each curve is consistent with flat. We can therefore use only one network to look for all decays.

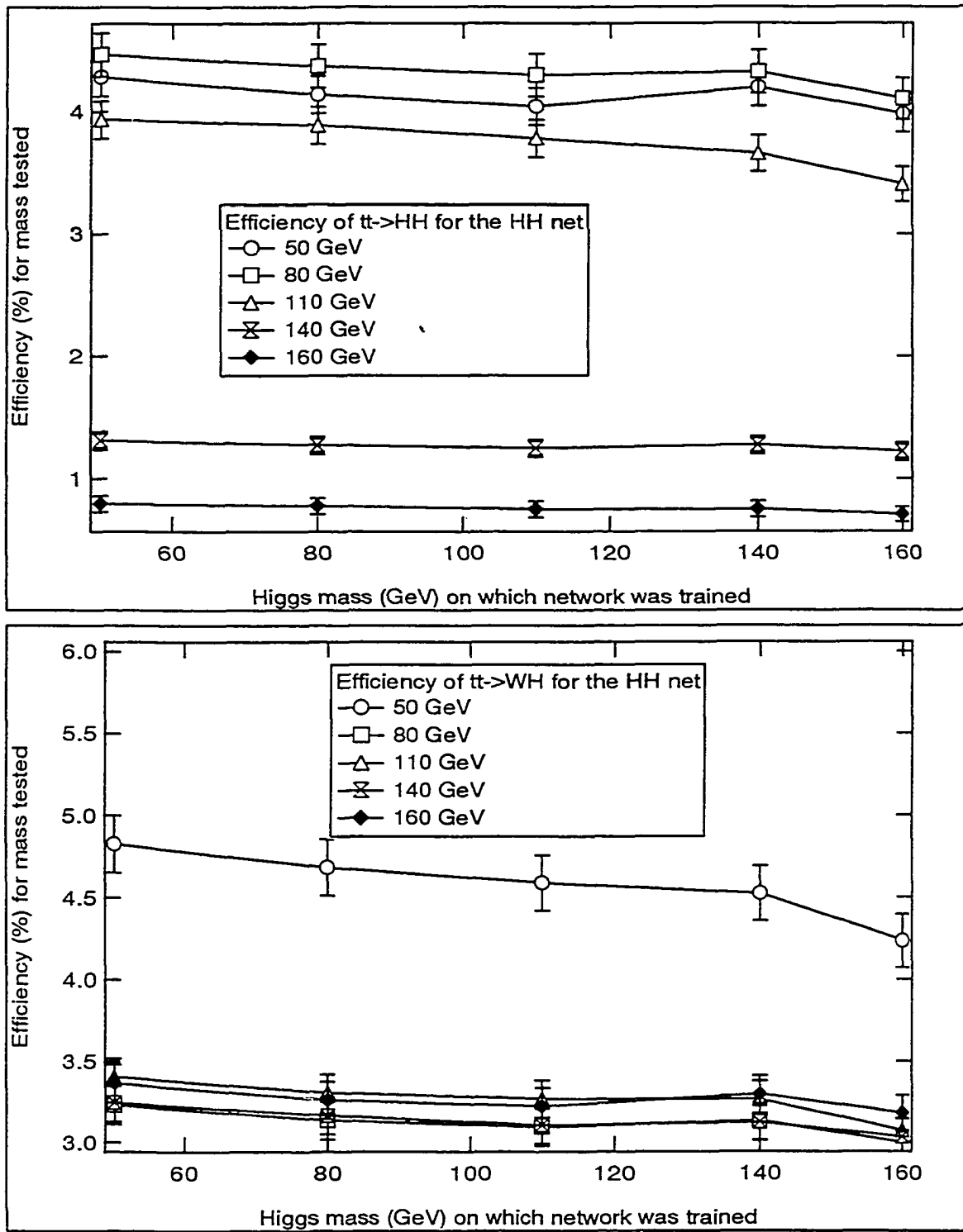


Figure 9.14: Efficiency of detecting $t\bar{t} \rightarrow WH$ and $t\bar{t} \rightarrow HH$. Each curve is the efficiency for detecting single mass, and the abscissa is the mass on which the network was trained.

Returning to equation 9.9, we see that we need probabilities for a continuum of Higgs masses, but only have Monte Carlo for a few points. In order to generate $P(n|\tan\beta, M_{H+})$ for all M_{H+} , we fit the $P(n|\tan\beta, M_{H+})$ for the generated masses of 50, 80, 110, 140, 160 GeV with 12th order polynomials, and fit each of the thirteen parameters of those polynomials as a function of M_{H+} with third order polynomials. The fits to the parameters can then be used to generate $P(\tan\beta, M_{H+}|n)$ for any intermediate Higgs mass. The collection of probability curves for different M_{H+} form the likelihood surface of equation 9.9, and we set a limit along a contour of constant likelihood which encloses 95% of the volume under the surface. Figures 9.15 - 9.16 show the fits to the thirteen parameters of fits to $P(n|M_{H+}, \tan\beta)$ for a network trained on $t\bar{t} \rightarrow HH$. The region of physical interest is $0.3 < \tan\beta < 150$. The original fit extends from $0.1 < \tan\beta < 300$ to ensure that the estimate is well behaved in the physical region. Figures 9.17 - 9.21 show $P(n|\tan\beta, M_{H+})$ from an analytic calculation (using efficiencies from MC), and the estimate of the fit using fits to the eleven parameters. Figure 9.22 shows the probability surface constructed from the measured and predicted probabilities at each higgs mass.

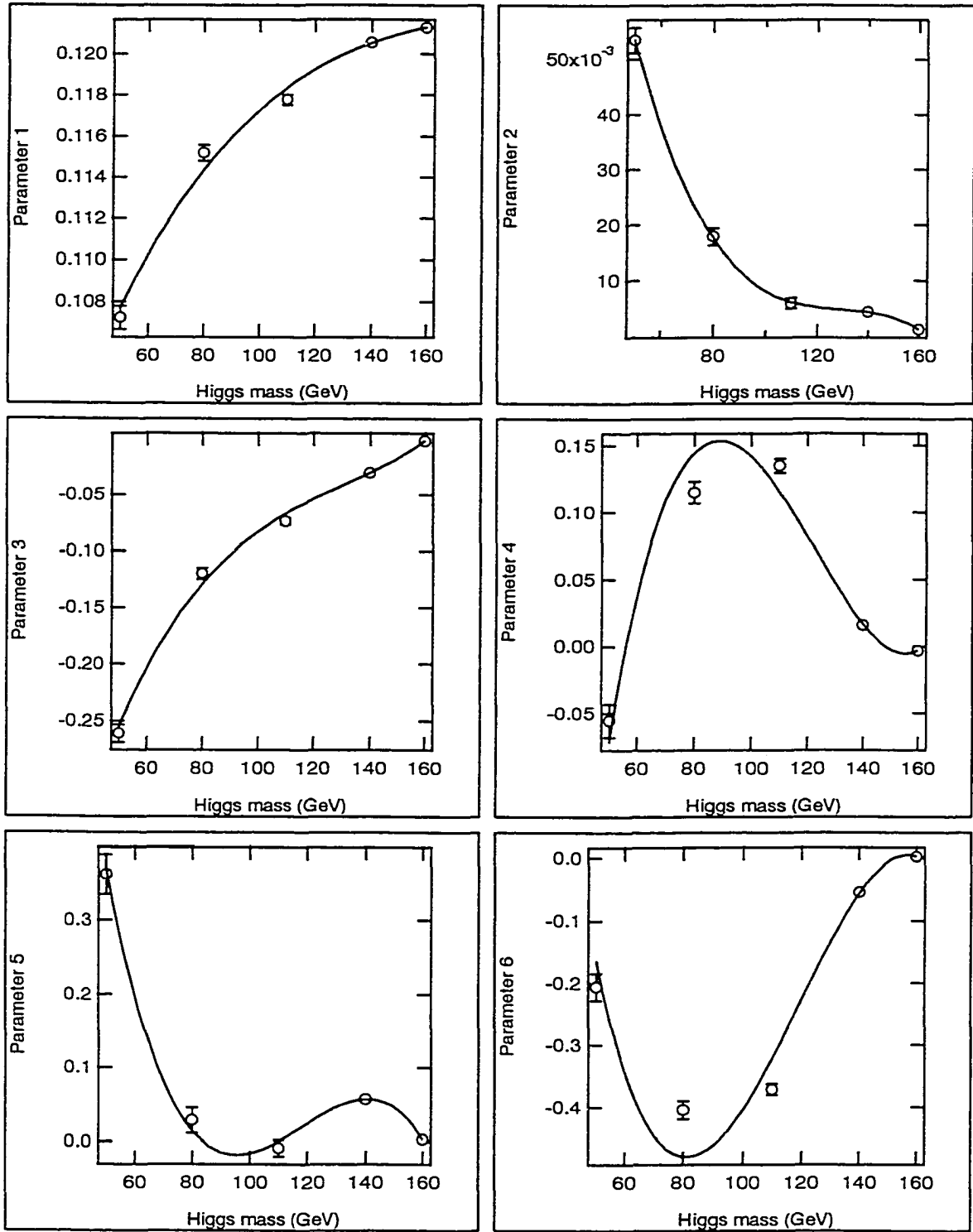


Figure 9.15: Fits to the first six parameters used to fit probabilities from the NN_{HH} network, where the cut on the output was placed at 0.88.

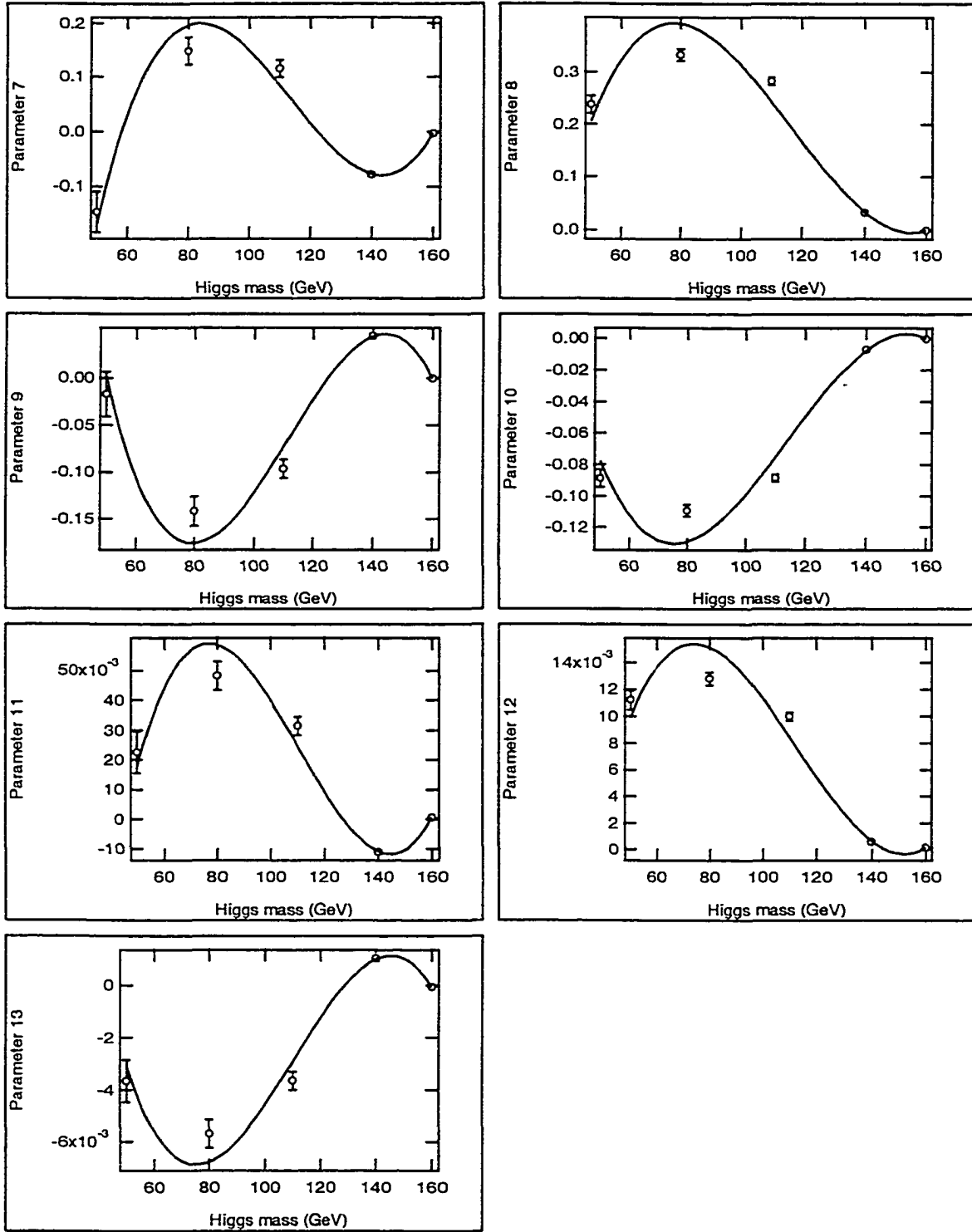


Figure 9.16: Fits to the last seven parameters used to fit probabilities from the NN_{HH} network, where the cut on the output was placed at 0.88.

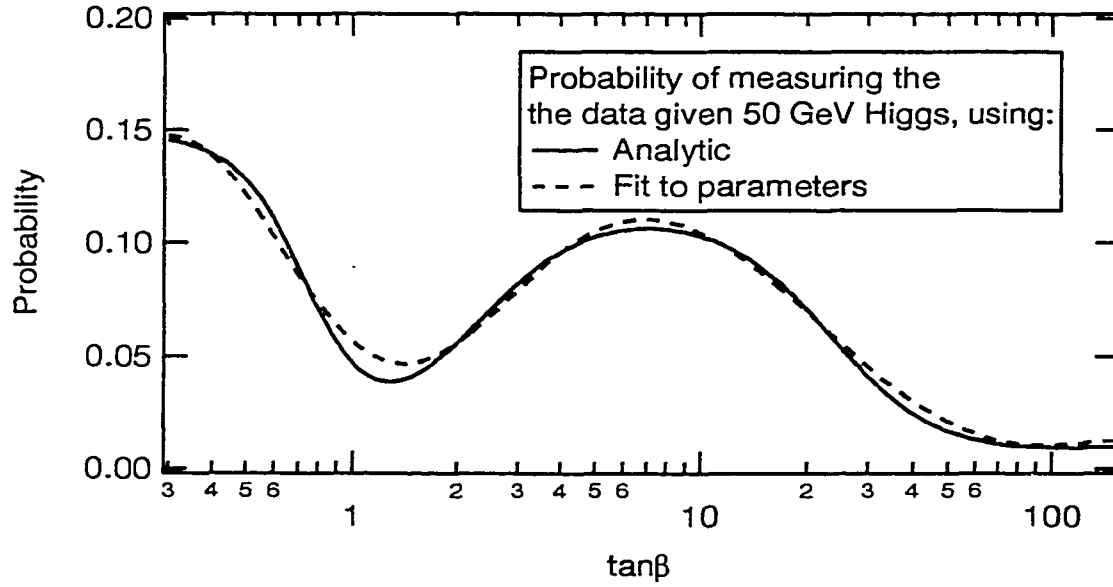


Figure 9.17: Probability of measuring the data in the NN_{HH} network.

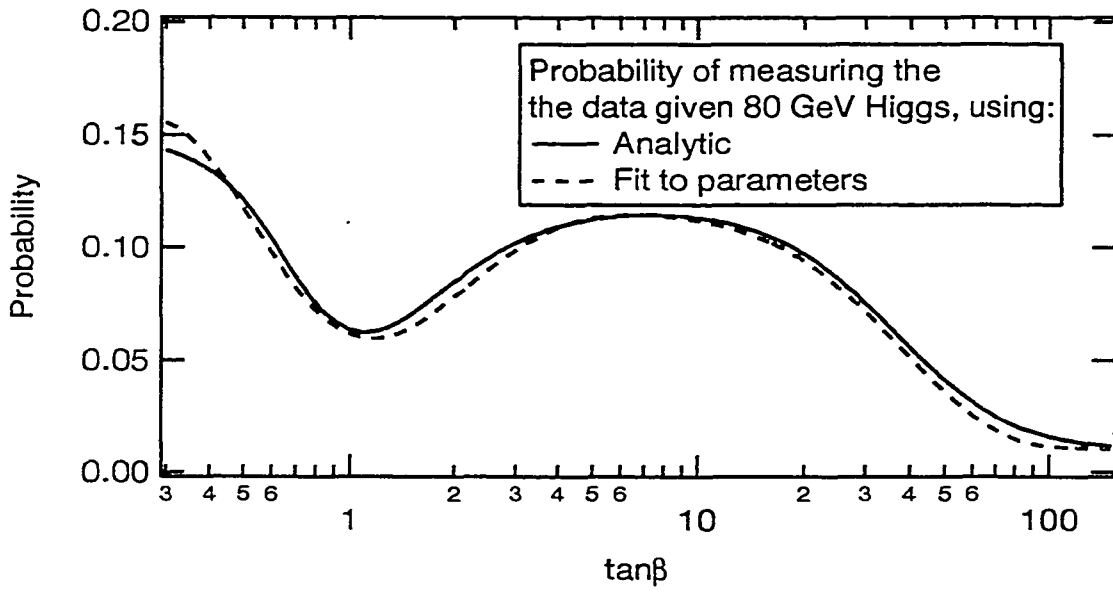


Figure 9.18: Probability of measuring the data in the NN_{HH} network.

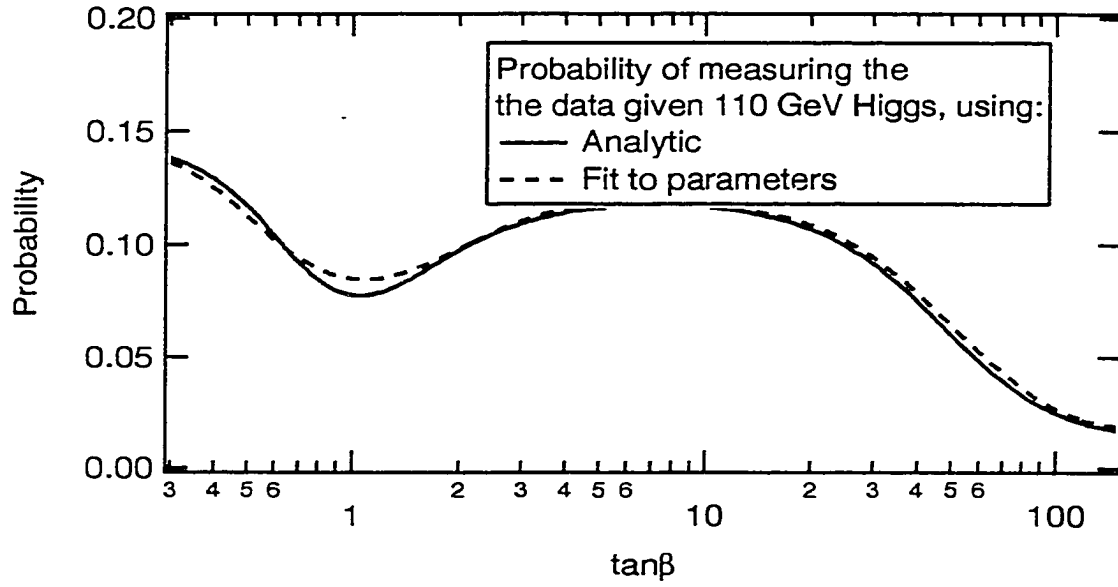


Figure 9.19: Probability of measuring the data in the NN_{HH} network.

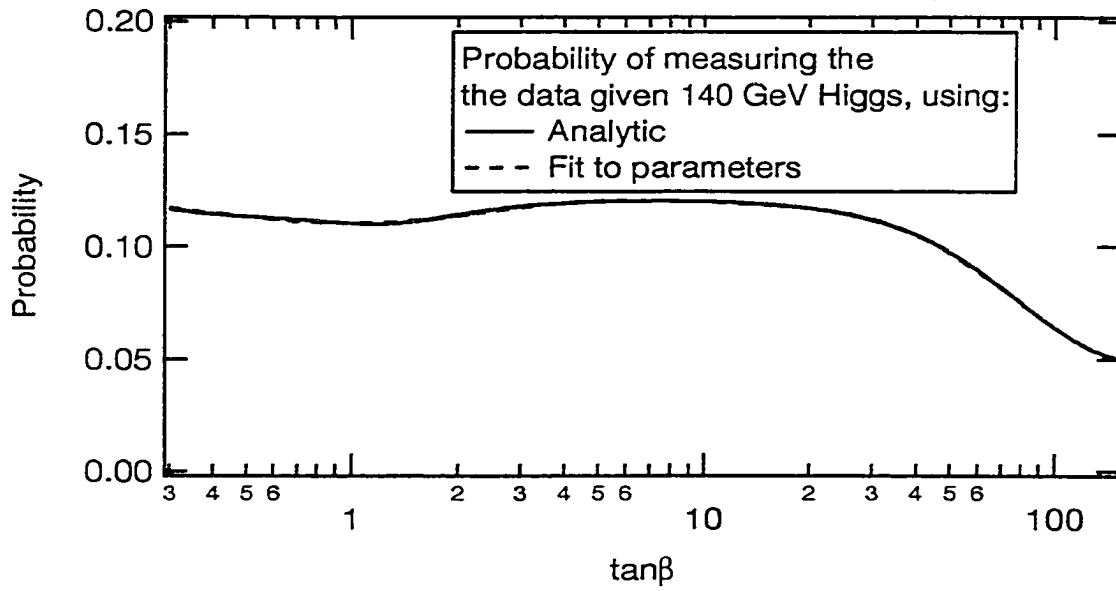


Figure 9.20: Probability of measuring the data in the NN_{HH} network.

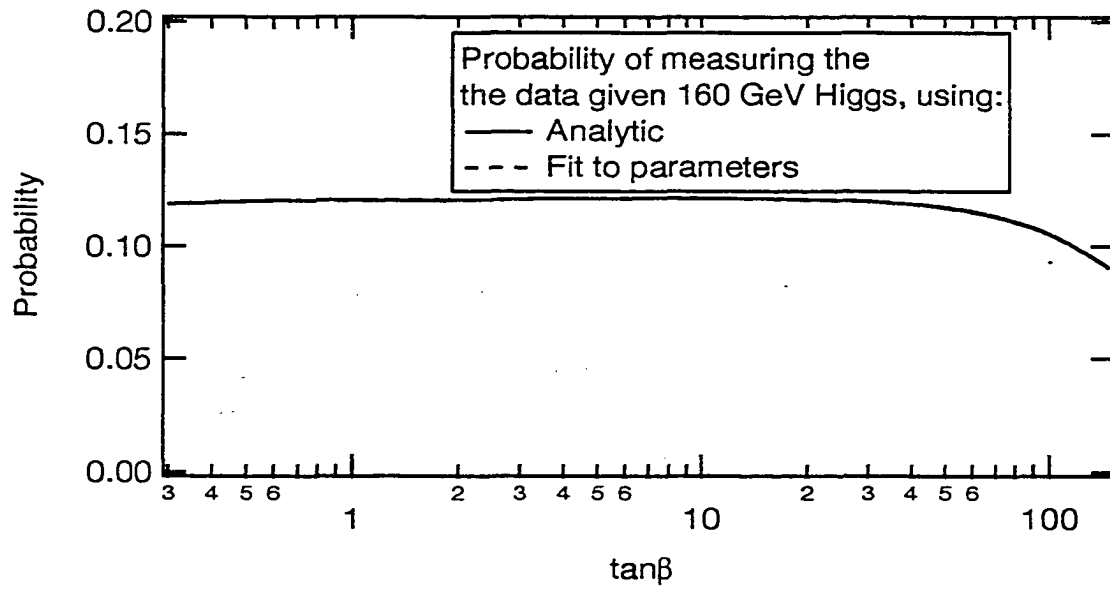


Figure 9.21: Probability of measuring the data in the NN_{HH} network.

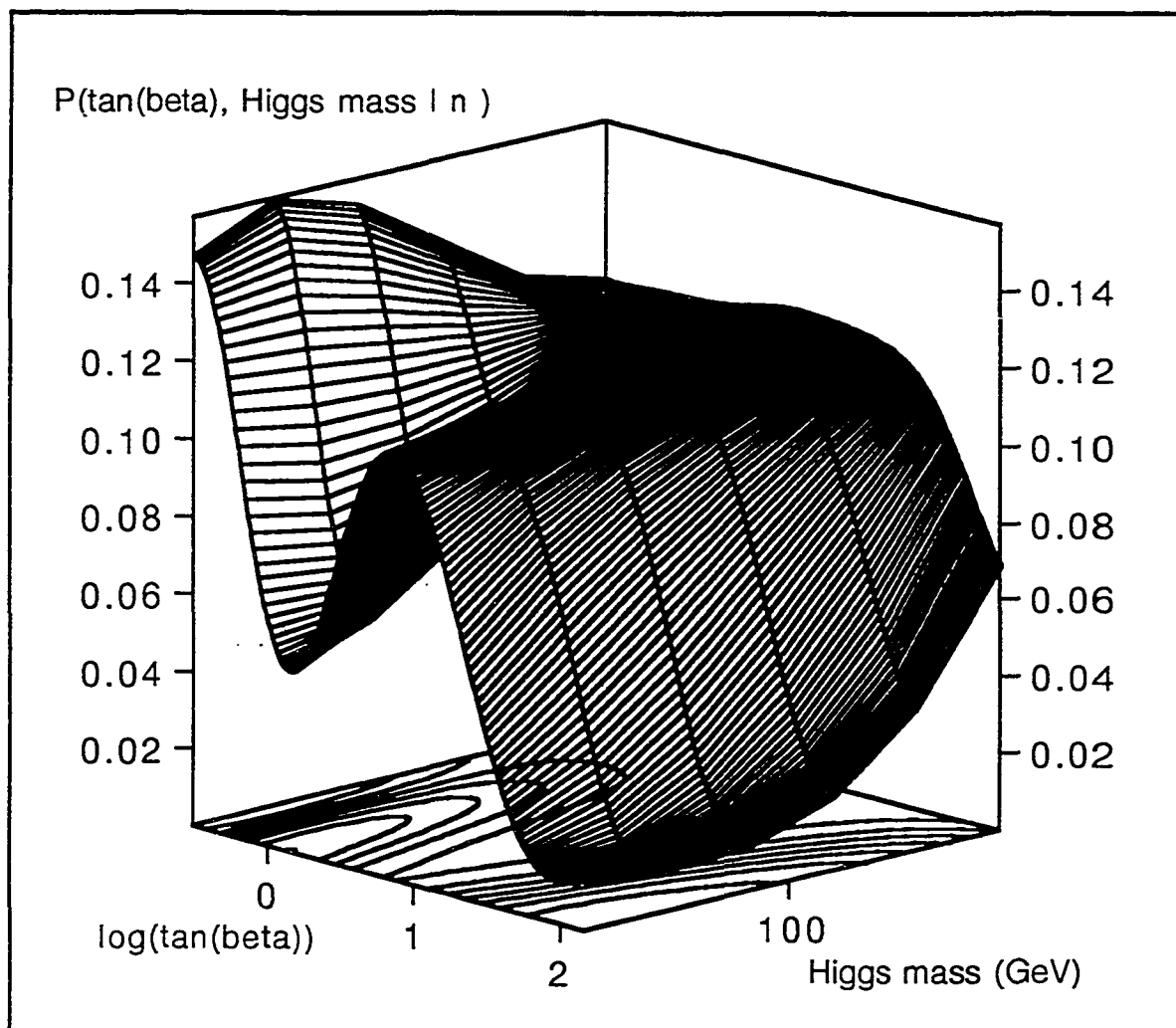


Figure 9.22: Likelihood surface of $P(\tan \beta, M_{H^+} | n)$.

9.1.1 Choosing the NN cut

We now have all of the information in hand to exclude regions of space unlikely to contain H^+ , and we must choose a cut on the neural net output. An estimate of the area in the $(\tan\beta, M_{H^+})$ plane which will be excluded can be made using MC, where our n is not the number of observed events, but the number predicted, given contributions from $t\bar{t} \rightarrow WW$, $W + jets$, and QCD only, and our b contains contributions from all sources. Figure 9.23 shows the area we expect to exclude for various NN cuts, as well as samples of MC exclusion curves. We choose a NN cut of 0.88, which maximizes the excluded area.

9.2 Frequentist Results

One method of setting limits examines only the probability that a measurement belongs to some predicted parent distribution. A 95% confidence limit is set on a process when five or fewer of 100 experiments would produce the measurement. The prediction of the number of experiments which would produce n or fewer events in 100 experiments, given a parent distribution with a mean of b is

$$\begin{aligned} N_e &= 100 \sum_{m=0}^n \int_0^\infty d\mu \frac{\mu^m e^{-\mu}}{m!} \frac{1}{\sqrt{2\pi}\sigma_b} e^{-(\mu-b)^2/2\sigma_b^2} \\ &= 100P(n, b, \sigma(b)) \end{aligned} \quad (9.12)$$

The frequentist approach examines the absolute probability that some outcome is obtained, and is not affected by probabilities in other regions of parameter space, as is the case in the Bayesian approach. For that reason, the additional low $\tan\beta$ decays which had to be estimated in the Bayesian analysis are no concern here. Figure 9.24 shows the probabilities of measuring n or fewer events in the NN_{HH} network, where n is the number of events found in JET_MS_MULTI. Also shown is the number of events expected in the NN_{HH} network, given H^+ . A 95% confidence limit is set where the probability is $< 5\%$.

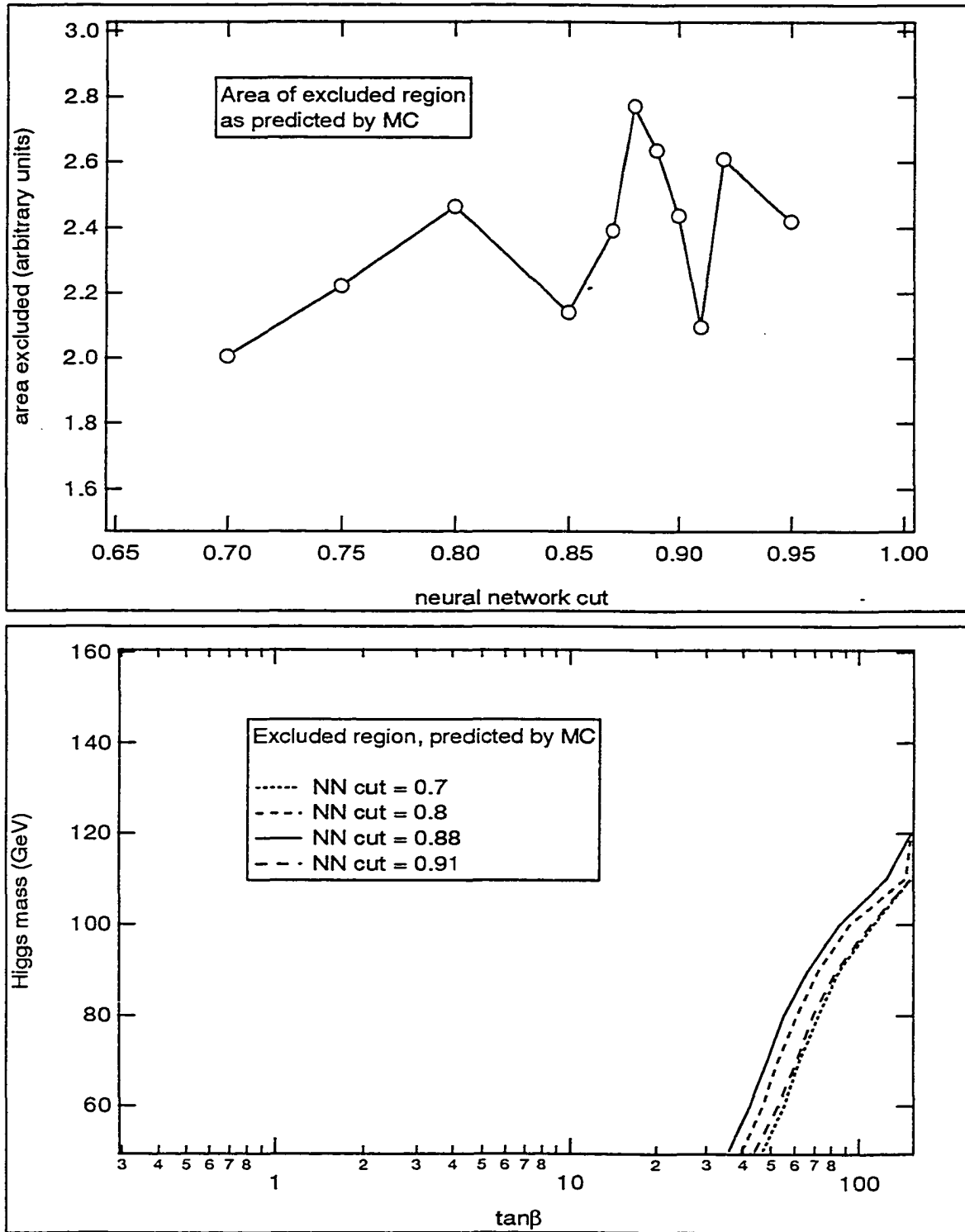


Figure 9.23: Predictions of the excluded area, using efficiencies from MC.

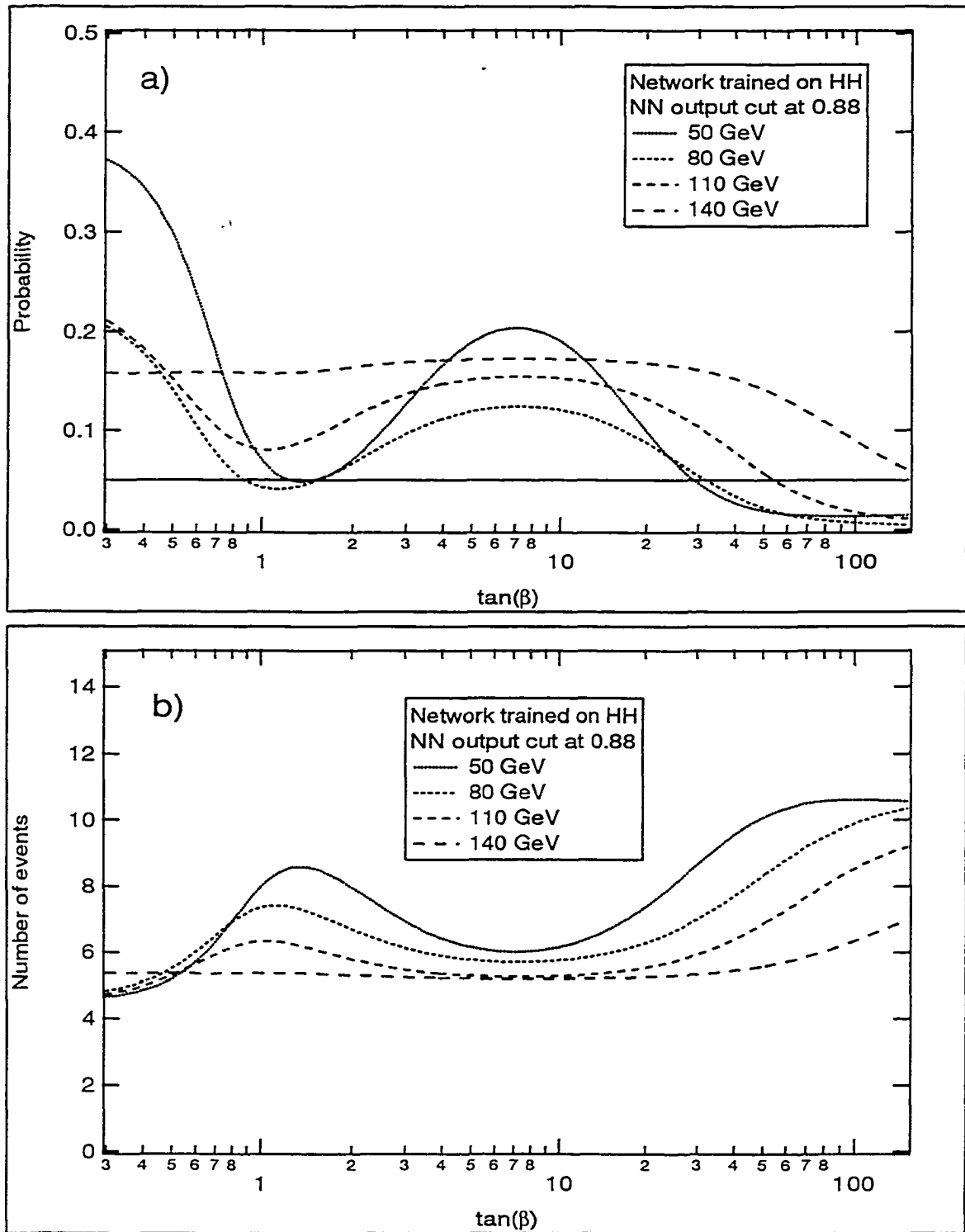


Figure 9.24: a) Probability that JET_MS_MULTI containing H^+ would give at most the values measured in data. b) Number of events expected in JET_MS_MULTI given H^+

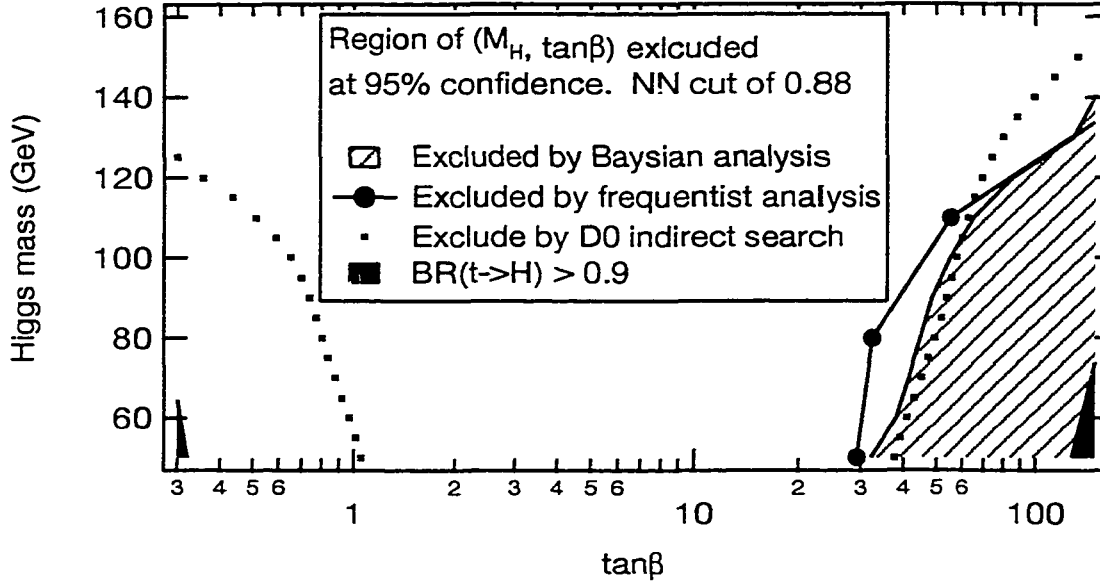


Figure 9.25: Region excluded by our search, for a NN cut of 0.88.

9.3 Conclusions

We have performed a direct search for a charged Higgs lighter than the top quark, in the region of $0.3 < \tan \beta < 150$, and any couplings of H^+ to non-SM particles was ignored. Figure 9.25 shows the excluded region which results from a frequentist approach, as well as a Bayesian approach. We show the comparison of the limits set by the indirect and direct searches.

We also show the effects of some alternative choices in the analysis. The first concern is the effect of using a NN cut other than 0.88. Figure 9.26 shows the effect of using three different cuts on neural network output. The small effect on the limit is an indication of the robustness of the result.

Our next concern is the poor fit at 80 GeV to some of our 13 parameters used to estimate intermediate Higgs masses (Figures 9.15 - 9.16). It is clear from Figure 9.18 that the area under the probability curve is incorrect. Our problem, of course, is a lack of Monte Carlo. We can make an estimate of the error in the Bayesian limit by using a different fit to these 13 parameters. Using the five masses available, we

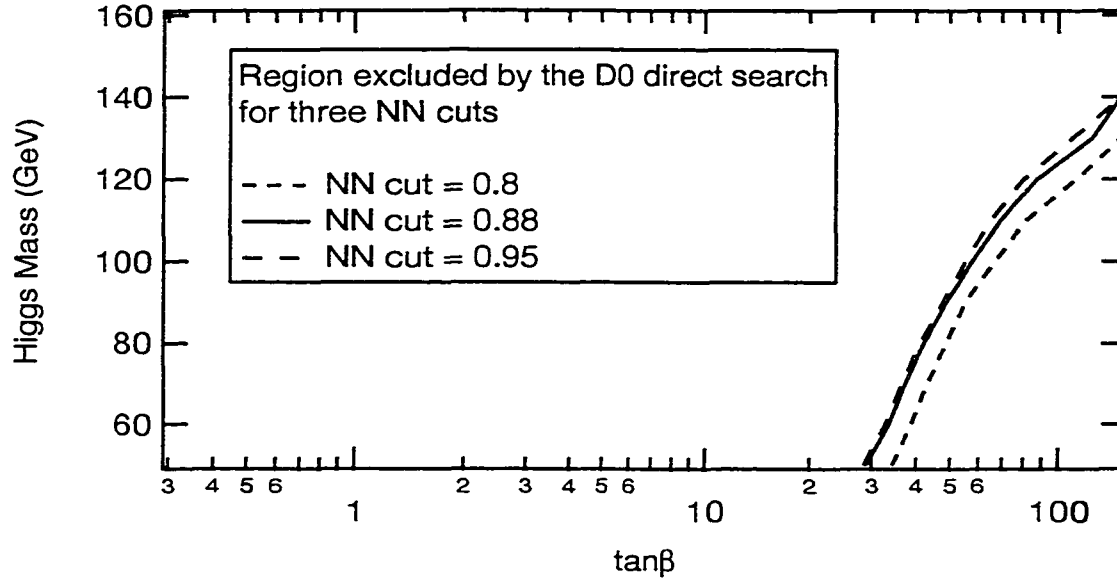


Figure 9.26: Effect on the Bayesian limit of using different cuts on neural net outputs.

can over-fit using a fourth order polynomial, which will force the curve through all mass points, but we can have little faith that the intermediate values estimated more accurately than the estimate using only a cubic fit. Figure 9.27 shows the effect of using a fourth order fit to generate the surface $P(\tan \beta, M_{H^+}|n)$. Additional Monte Carlo will be used to fill in the masses 65 GeV, and 95 GeV. It is expected that the resulting limit will lie somewhere in the small space between the curves obtained from the fourth and third order fits.

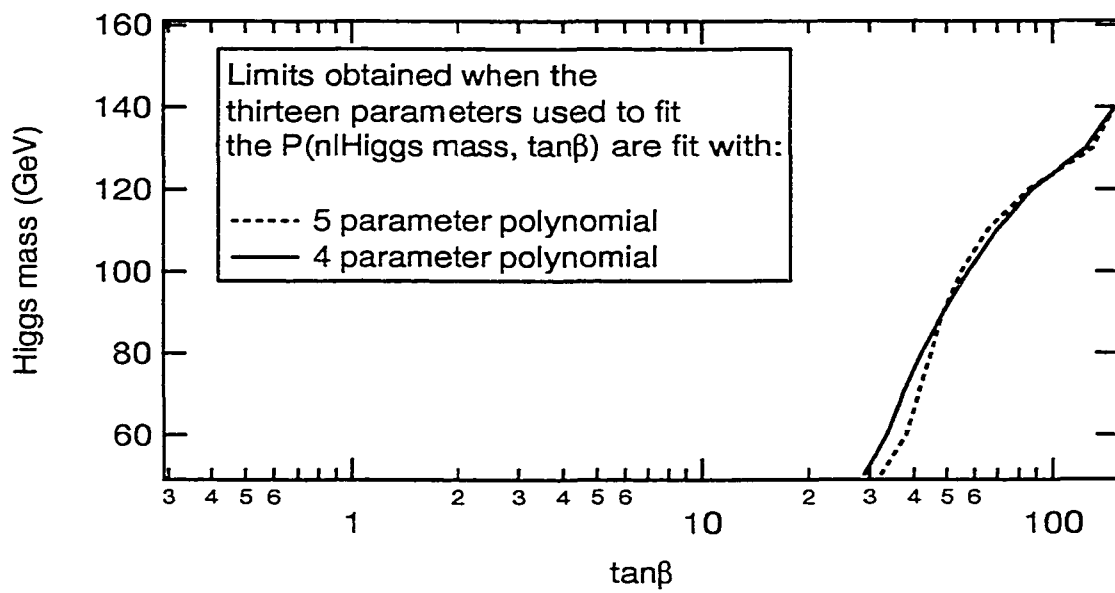


Figure 9.27: Effect on the Bayesian limit of using a fourth order polynomial fit the 13 parameters used to generate $P(n|\tan\beta, M_{H^+})$.

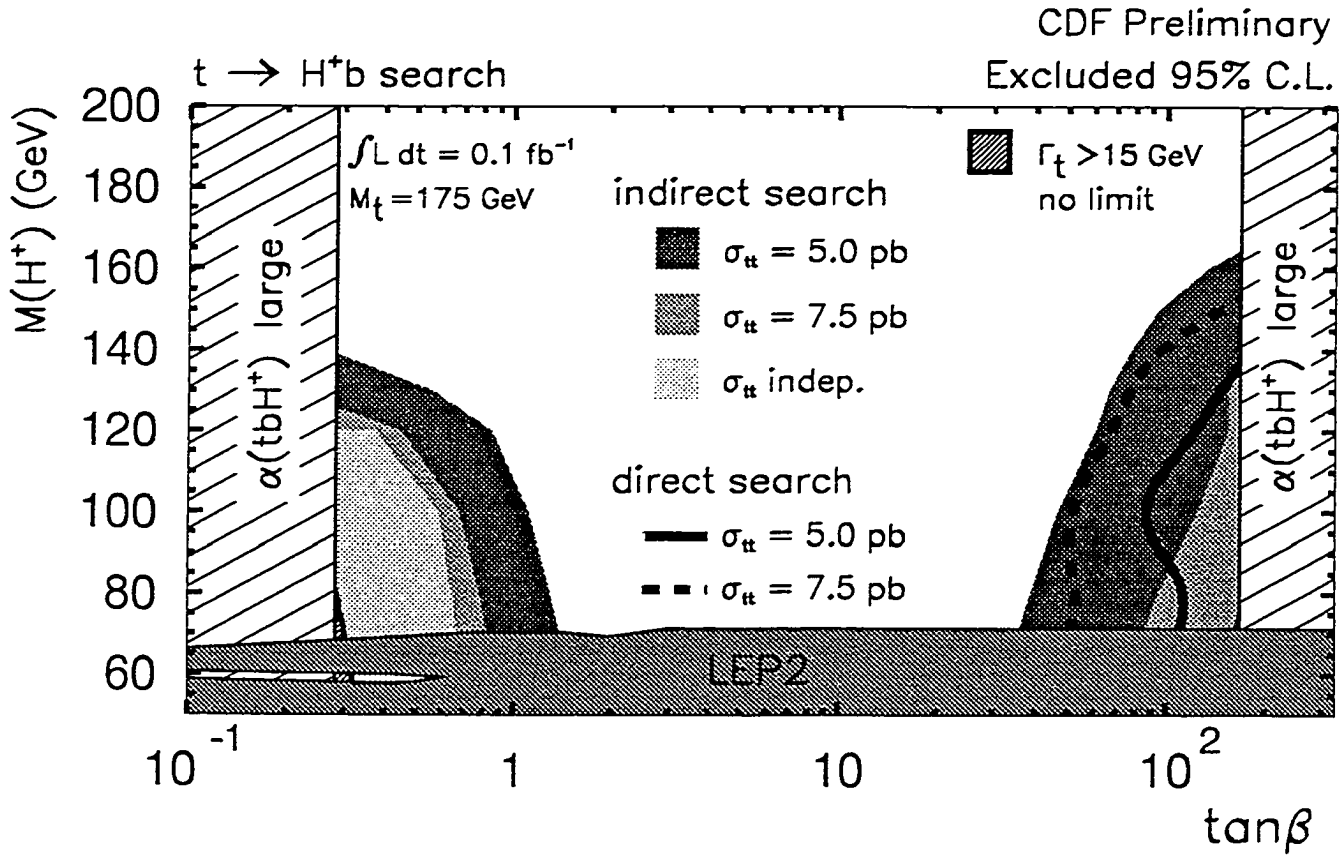


Figure 9.28: Limits on $(\tan\beta, M_{H^+})$ from CDF and LEP2. The hatched region labelled “ $\alpha(tbH^+)$ large” indicates $\alpha \geq 1$.

9.3.1 Limits from other experiments

CDF, and LEP2 both have limits on a direct searches for H^+ . Like the $D\bar{O}$ search, CDF looks for decays of the type $t\bar{t} \rightarrow H^+ X$; $H^+ \rightarrow \tau^+ \nu_\tau$. LEP2 looks for H^+ in the process $Z \rightarrow H^+ H^-$, where the H^+ decays to τ or $c\bar{s}$. Figure 9.28 shows the current limits from these two experiments. The Feynman rule for the ZH^+H^- vertex is:

$$\frac{-ig \cos 2\theta_W}{2 \cos \theta_W} (p + p')^\mu \quad (9.13)$$

So that the $BR(Z \rightarrow H^+ H^-)$ is independent of $\tan\beta$; however, the decay of H^+ does depend on $\tan\beta$, and we therefore do expect to see some structure in the limit placed by LEP2. As one expects, the limit is independent of $\tan\beta$ in the region

where H^+ is independent of $\tan \beta$, namely $3 \leq \tan \beta$.

CLEO has performed an indirect search for H^+ in the FCNC decay $b \rightarrow s\gamma$ [46]. The SM decay proceeds through a triangle diagram containing W^+ , c . The presence of H^+ allows for the competing triangle diagram containing H^+ , c . The lower limit on M_{H^+} set by CLEO is $M_{H^+} > 244 + 63/(\tan \beta)^{1.3}$, although this limit is not valid in cases where the H^+ is allowed to couple to non-SM particles [47].

Appendix A

Principles of Feed-forward Neural Networks

As the cornerstone of this analysis, the topic of neural networks demands special attention. Although useful neural networks have been in use since the mid-1980s, they have met with some resistance in data analysis because of their “black box” nature. I rely heavily on information from an excellent source [48] which is freely available on the web.

A.1 Fundamentals

The basic component of every neural network is the *neuron*. Common to every neuron are:

- The notion of an input, of which there may be many with distinct values, and the notion of an output, of which there may be many, but all have the same value.

- Weighted connections, w_{ik} between the k th neuron's inputs, and the outputs of any number of other neurons (with a one-to-one correspondence between an input of one neuron and the output of another).
- An external bias, θ_k providing a signal to a neuron, independently of its inputs. The bias term is added to mirror the functionality of a biological neuron, by acting as an inhibiting or activating external signal.
- An effective output s_k of a neuron, calculated from its weighted inputs and bias, according to some propagation rule.
- Neuron output, y_k , determined by a neuron's activation function, $\mathcal{F}(s_k)$.
- Method for updating the connection weights, $w_{ik}(t) \rightarrow w_{ik}(t+1)$.

The most common type of neuron, and the one used here, uses a propagation rule:

$$s_k(t) = \sum_i w_{ik}(t)y_i(t) + \theta_k(t) \quad (\text{A.1})$$

And the activation function chosen is a sigmoid:

$$\mathcal{F}(s_k) = \frac{1}{1 + e^{-2s_k}} \quad (\text{A.2})$$

Figure A.1 shows a schematic diagram of the basic neuron and its connections.

The network is built from a collection of connected neurons. The topology chosen for this analysis is called a *feed-forward* network, where data flows from the network input to the output, and no feedback loops are present. The neurons are arranged in layers, in which no connections between neurons in the same layer are allowed. A network consisting of three layers is sufficient to model any problem, and that is the type of network used here. Figure A.2 shows a schematic diagram of a network with two input nodes, three hidden nodes and two output nodes.

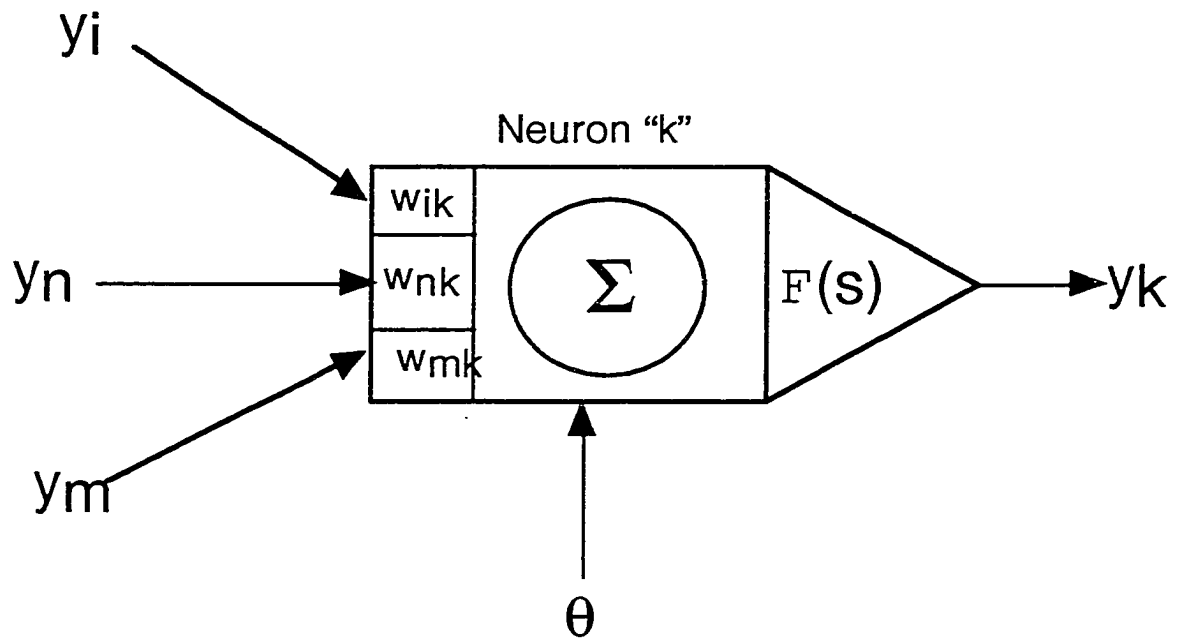


Figure A.1: Schematic of the basic neuron.

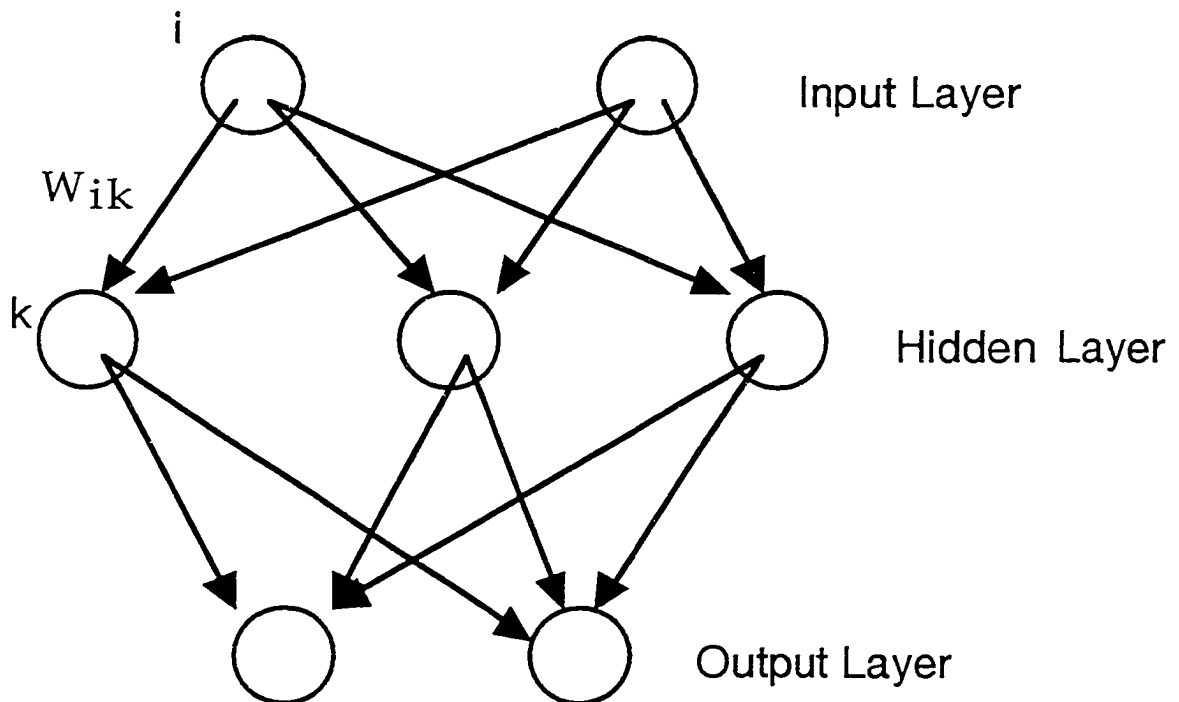


Figure A.2: Schematic of a full network.

A.2 Back-Propagation

The goal of the feed-forward network is the association of a set of inputs, called patterns (x^p), with a desired set of outputs, d_o^p , where the subscript o denotes the o th neuron in the output layer. There is a one-to-one correspondence between each element in the vector x^p and each input neuron.

The measure of error for the p th pattern is

$$E^p = \frac{1}{2} \sum_o (d_o^p - y_o^p)^2 \quad (\text{A.3})$$

Using the minimization of E^p , the connection weights and neuron biases must be updated:

$$w_{ik}(t+1) = w_{ik}(t) + \Delta w_{ik}(t) \quad (\text{A.4})$$

$$\theta_k(t+1) = \theta_k(t) + \Delta \theta_k(t) \quad (\text{A.5})$$

$$\Delta_p w_{ik} = -\gamma \frac{\partial E^p}{\partial w_{ik}} \quad (\text{A.6})$$

$$\Delta_p \theta_k = -\gamma \frac{\partial E^p}{\partial \theta_k} \quad (\text{A.7})$$

Where γ is a positive constant of the network, called the *learning rate*.

Using the chain rule, and equation A.1, we can write:

$$\frac{\partial E^p}{\partial w_{ik}} = \frac{\partial E^p}{\partial s_k^p} \frac{\partial s_k^p}{\partial w_{ij}} \quad (\text{A.8})$$

$$\begin{aligned} &= \frac{\partial E^p}{\partial s_k^p} y_i^p \\ &\equiv -\delta_k^p y_i^p \end{aligned} \quad (\text{A.9})$$

The trick is in determining the value of δ_k^p , which is accomplished through the process of *back-propagation* of errors. Using the chain-rule, and equation A.2 we can write:

$$\delta_k^p = -\frac{\partial E^p}{\partial y_k^p} \frac{\partial y_k^p}{\partial s_k^p} \quad (\text{A.10})$$

$$= -\frac{\partial E^p}{\partial y_k^p} \mathcal{F}'(s_k^p) \quad (\text{A.11})$$

In the case that we are to update the weights of an output node, the first term can be calculated from the definition of E^p :

$$\frac{\partial E^p}{\partial y_o^p} = -(d_o^p - y_o^p) \quad (\text{A.12})$$

and the adjustment to the weights of the output node is:

$$\Delta_p w_{jo} = \gamma \delta_o^p y_j^p \quad (\text{A.13})$$

The adjustment to the weights of the hidden nodes is determined by:

$$\frac{\partial E^p}{\partial y_h^p} = \sum_o \frac{\partial E^p}{\partial s_o^p} \frac{\partial s_o^p}{\partial y_h^p} \quad (\text{A.14})$$

where h indicates a hidden node (neuron), and o indicates an output node. Using equation A.1, this is:

$$\sum_o \frac{\partial E^p}{\partial s_o^p} \frac{\partial s_o^p}{\partial y_h^p} = \sum_o \frac{\partial E^p}{\partial s_o^p} \frac{\partial}{\partial y_h^p} \sum_j y_j^p w_{jo} = \sum_o \frac{\partial E^p}{\partial s_o^p} w_{ho} = - \sum_o \delta_o^p w_{ho} \quad (\text{A.15})$$

whence, by equation A.11

$$\delta_h^p = \mathcal{F}'(s_h^p) \sum_o \delta_o^p w_{ho} \quad (\text{A.16})$$

The bias terms, θ_k , can be calculated in precisely the same manner, and we find:

$$\Delta_p \theta_k = \gamma \delta_k^p \quad (\text{A.17})$$

The goal of network training is to find the best set of weights, but it is very desirable to do it in the shortest possible time. If the learning rate is small enough, convergence will be reached, eventually. If one becomes impatient and chooses a large learning rate, the network may oscillate around the best solution without ever reaching it. In order to speed learning while preventing oscillation, a *momentum* term α is added to the update of the weights:

$$\Delta w_{ik}(t+1) = \gamma \delta_k^p y_i^p + \alpha \Delta w_{ik}(t) \quad (\text{A.18})$$

So, the neural network is just a “least-squares machine”, which combines a series of activation functions in a way which best maps a set of input patterns to a set of desired outputs. The standard choice of desired outputs when trying to differentiate between signal and background is 1, when a signal pattern is presented to the network inputs, and 0 when a background pattern is presented. The process of error-minimization automatically accounts for any correlations between input variables, which always results in cuts which are as good as, or better than, cuts chosen as constants with respect to the input variables.

Bibliography

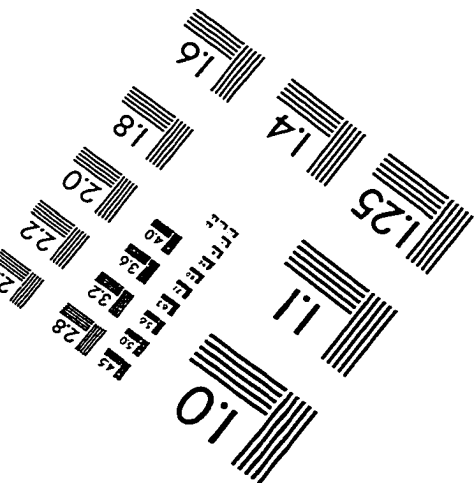
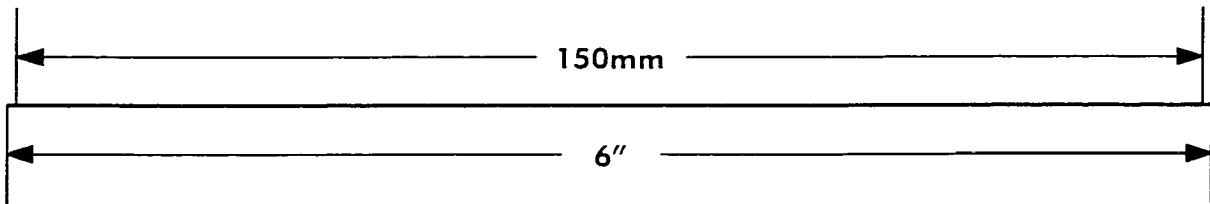
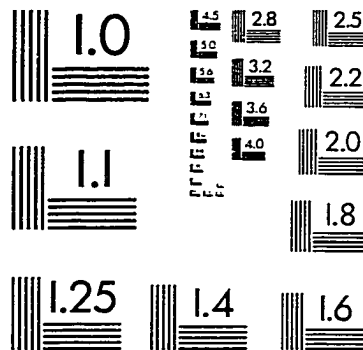
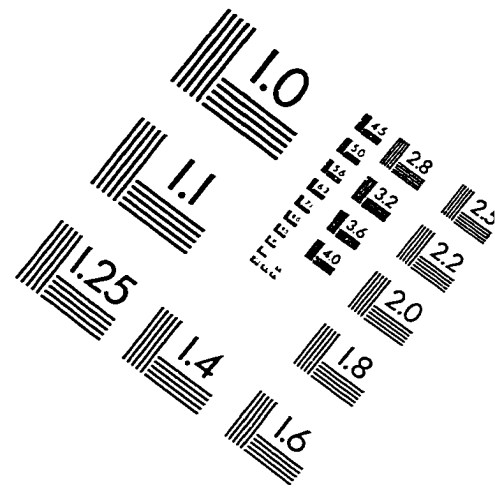
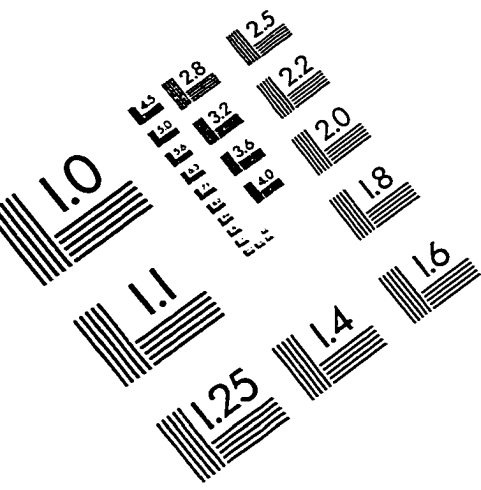
- [1] Chris Quigg. *Gauge Theories of the Strong, Weak, and Electromagnetic Interactions*. pg 42. Addison-Wesley, Reading, MA, 1983
- [2] Chris Quigg. *ibid.* pg 72.
- [3] J. Goldstone, A. Salam, and S. Weinberg, *Phys. Rev.* **127**, 965 (1962).
- [4] Chris Quigg. *ibid.* pg 74.
- [5] S. Weinberg. *The Quantum Theory of Fields*. pg. 217. Cambridge Press, NY, NY, 1995
- [6] I. Aitchison, and A. Hey. *Gauge Theories in Particle Physics 2nd Edition*. pg 428. IOP Publishing, Bristol, UK, 1993.
- [7] F. Halzen, and A. Martin. *Quarks & Leptons* pg. 334, Wiley, NY, NY, 1984,
- [8] J. Gunion. *The Higgs Hunter's Guide*. pg. 195, Addison-Wesley, Reading, MA, 1990.
- [9] M. Baarmand, D. Chakraborty, R. Raja, E. Smith. "An indirect search for a light charged Higgs boson in the decay of top quark pairs in lepton+jets final states in $p\bar{p}$ collisions", DØ note 3298.
- [10] F Abe et al., "Search For Charged Higgs Decays of the Top Quark Using Hadronic Decays of the Tau Lepton", FERMILAB-PUB-97/058-E.

- [11] S. Abachi et al., "The DØ detector", Nuclear Instrumentation and Methods in Physics Research A, 338:185-253, 1994.
- [12] S Snyder, "The DØ Detector", DØ note 2500.
- [13] J. Thompson, "Introduction to Colliding Beams at Fermilab", Fermilab Tech. Memo. TM-1909, October 1994.
- [14] J Butler, "Main Ring Deadtime", DØ note 1682.
- [15] N Amos, "Main Ring Veto Counters for RunIB", DØ note 2072
- [16] AR Clark, "The Central Tracking Detectors for DØ", Nuclear Instruments and Methods in Physics Research A279:243, 1989.
- [17] RC Fernow, *Introduction to Experimental Particle Physics*, Cambridge: Cambridge University Press, 1986.
- [18] T Ferbel, *Experimental Techniques in High Energy Physics*, Addison-Wesley, 1987.
- [19] M Abolins et al., "Hadron and Electron Response of Uranium/Liquid Argon Calorimeter Modules for the DØ Detector", Nuclear Instruments and Methods in Physics Research, A280:36, 1989.
- [20] C Brown et al., "DØ Muon System with Proportional Drift Tube Chambers", Nuclear Instruments and Methods in Physics Research A279:331, 1989.
- [21] M. Abolins et al., "The level one framework" DØ note 328 revised, DØ note 705, 1988.
- [22] M. Abolins et al, *IEEE Trans. Nucl. Sci.*, 36(1):384-389, 1989.
- [23] M. Abolins, D. Edmunds, P. Laurens, and B. Pi. *Nucl. Instr. and Methods*, A289:543-560, 1990.

- [24] S. Snyder “Measurement of the Top Quark Mass at DØ”, PhD thesis, SUNY, Stony Brook NY, 1995.
- [25] N Amos, “Measurement of the Top Quark in Multi-jet Final States in ppbar Collisions”, DØ note 3333.
- [26] V.D. Barger, R.J.N., *Collider Physics* Addison-Wesley, Mass, 1987.
- [27] B Abbott et al., “Fixed Cone Jet Definitions in DØ and R_{sep} ”, Fermilab-PUB97/242-E.
- [28] G Di Loreto, “Methodology for the derivation of the Offset correction”, DØ note 3542.
- [29] B. Abbot et al., “Determination of the Absolute Jet Energy Scale in the DØ Calorimeters”, Fermilab-Pub-97-330-E
- [30] J. Krane “A Multiple Interaction Tool for $\sqrt{s} = 630$ GeV”, DØ note 3265, 1997.
- [31] J. Krane “The Ratio of Inclusive Jet Cross Sections at $\sqrt{s} = 630\text{GeV}$ and $\sqrt{s} = 1800\text{GeV}$ ”, PhD thesis, University of Nebraska, Lincoln NE, 1998.
- [32] B Abbott, “Jet Transverse Energy Shape in $p\bar{p}$ Collisions at $\sqrt{s} = 1.8$ TeV”, PhD thesis, Purdue University, 1994.
- [33] E. Won “Top Quark Production in Multi-Jets Final States”, PhD thesis, University of Rochester, Rochester NY, 1996.
- [34] H. Greenlee, “B Tagging Fraction From Multijet Data”, DØ note 2180 (1994).
- [35] M. Narain and F. Stichelbaut, “B Tagging in ttbar Events for Run II”, DØ note 3243 (1997).

- [36] Gupta, Mondal, Narain, “b Tagging Using Electrons Near a Jet”, DØ note 2901 (1996).
- [37] S. Youssef, C. Hebert, Current work underway to identify b jets using electrons inside the jet.
- [38] R. Raja, D. Wirjawan, Qizhong Li, “H MATRIX for TAU identification in $D\bar{D}$ ”, unpublished.
- [39] S Protopopescu, “Rules for ZEBRA Banks”, DØ note 354 (1986)
- [40] R Raja, “Use of Zebra in DØ (Offline Tutorial)”, DØ note 1002 (1990)
- [41] Q Li, “A Measurement of the $\sigma(p\bar{p} \rightarrow W) \cdot Br(W \rightarrow \tau\nu)$ as a Test of Lepton Universality at $\sqrt{s}=1.8$ TeV”, DØ note 3214
- [42] G Griffith et al., “ $W \rightarrow e\nu$ Data-Based $W \rightarrow \tau\nu$ Monte Carlo”, DØ Note 2938, 1996.
- [43] C Cretsinger, “Search for the Top in the All-Jets Channel”, PhD thesis, University of Rochester, Rochester, New York, December 1995.
- [44] E. Jaynes *Probability Theory: The Logic of Science*, <ftp://bayes.wustl.edu/pub/Jaynes/book.probability.theory/book.tar.gz>
- [45] D. Sivia *Data Analysis: A Bayesian Tutorial* Oxford Science Publications, 1996.
- [46] CLEO collaboration, M. S. Alam et al., Phys Rev. Letters 74, 2885 (1995).
- [47] T. Goto and Y. Okada, Prog. Theor. Phys. 94, 407 (1995); F. M. Borzumati and N. Polonsky, [ph/9602433](http://arxiv.org/abs/hep-ph/9602433).
- [48] B. Kröse, P. van der Smagt *An Introduction to Neural Networks*, <http://www.robotic.dlr.de/Smagt/books/neuro-intro.ps.gz>, (1996).

IMAGE EVALUATION TEST TARGET (QA-3)



APPLIED IMAGE, Inc
1653 East Main Street
Rochester, NY 14609 USA
Phone: 716/482-0300
Fax: 716/288-5989

© 1993, Applied Image, Inc., All Rights Reserved

